Study of a Large Volume $CaF_2(Eu)$ Scintillating Bolometer with Metallic Magnetic Calorimeter

Li Xiaolong

A thesis presented for the degree of

Doctor of Physics in the Graduate School of Science

Osaka University

2020.02.06

Abstract

Neutrinoless double beta ($0\nu\beta\beta$) decay is a way to prove fundamental properties of neutrinos, such as Majorana nature, mass hierarchy and absolute mass scale. Many experiment groups around the world are developing various detection techniques and competing to observe the $0\nu\beta\beta$ decay for the first time.

Scintillating bolometer is a powerful tool to search for the $0\nu\beta\beta$ decay, because it can achieve a high energy resolution and a good discrimination power to reduce background. Our experiment group plans to develop a scintillating bolometer to search for the $0\nu\beta\beta$ decay of ^{48}Ca.

We established a large scintillating bolometer using a 312 g CaF_2(Eu) crystal with a readout technology of metallic magnetic calorimeters. Phonons and scintillation photons of the CaF_2(Eu) are detected by a metal film phonon collector and a germanium light detector, respectively. Since CaF_2(Eu)'s scintillation is easy to be absorbed by metals, we developed a special multi-layer metal film phonon collector having both a high thermal conductivity and a high optical reflectivity. We also studied a physical mechanism to understand the detector system through some basic calculations and Monte Carlo simulation.

A set of successful measurements were carried out for simultaneous detection for heat and light signals at a few 10 mK in an above-ground laboratory. We found large light signals with clear difference in scintillation yields between electron- and alpha-induced events. The comparison of relative amplitudes of heat and light signals obtained about 10 σ discrimination power. The resolution of scintillation signals was 3.1% for 4.9 MeV alpha events, so we can estimate that the same energy beta/gamma events should have 1.3% energy resolution because of a 17% quenching factor. The obtained resolution exceeded the one of the current running CANDLES experiment as 2.5%.

The intrinsic resolution of heat signals was 0.3% (FWHM) at 5.6 MeV, which was evaluated by silicon heater's signals and $^{222}\mathrm{Rn} \rightarrow {}^{218}\mathrm{Po} \rightarrow {}^{214}\mathrm{Pb}$

sequential alpha decay events. This intrinsic resolution has already satisfied our goal of resolution, 0.5% (FWHM). Through the study of the sequential alpha decay, however, we also found the heat signals experiencing strong position dependence from the event locations. This position dependence could be induced by the spin-lattice interaction of paramagnetic Eu ions in the CaF_2 crystal.

Contents

1 Neutrinos **6**

1.1 Existence of neutrino 6

1.2 Neutrino flavors 7

1.3 Neutrino oscillation 9

2 Neutrinoless Double beta decay **12**

2.1 Double beta decay 12

2.2 Neutrinoless double beta decay 14

2.3 Detection of neutrinoless double beta decay 18

2.4 Sensitivity of $0\nu\beta\beta$ experiment 21

3 Detection technologies for neutrinoless double beta decay search **24**

3.1 Large liquid scintillator detector 24

3.2 Germanium experiments 26

3.3 Tracker-Calorimeter: NEMO experiments 27

3.4 Bolometer experiments 29

4 Conceptualization of scintillating bolometer with a large CaF_2(Eu) scintillation crystal **34**

4.1 Absorber selection for $0\nu\beta\beta$ decay of ^{48}Ca 34

4.2 Preliminary low temperature experiments using CaF_2(Eu) scintillator for rare event physics 36

4.2.1 First bolometer of CaF_2(Eu) in 1992 36

4.2.2 Scintillation study at low temperature in 1995 37

4.2.3 First simultaneous detection of phonon and scintillation in 1997 38

4.3 Purpose of my study 40

5 Development of scintillating bolometer with a large CaF_2(Eu) crys-

tal **42**

5.1 Detector configuration 42

5.2 Basic properties of CaF_2(Eu) crystal used in this experiment 43

5.3 Phonon collector 48

5.4 Phonon collector design 51

5.5 Multi-layer metal film production 54

5.5.1 Surface cleaning method 54

5.5.2 Evaporation process 55

5.5.3 Evaporation results and adhesion test 57

5.6 Temperature increase measurement 60

5.7 Three types of photon propagations 62

5.7.1 Self-absorption 63

5.7.2 Photon absorption by metal film 67

5.7.3 Scintillation detection by light detector 72

5.8 Cherenkov radiation of beta rays 77

5.9 Total understood mechanism of detector 79

5.10 Detector set-up 81

5.10.1 Scintillating bolometer assembling. 81

5.10.2 Reflector selection 82

5.10.3 Dilution Refrigerator 83

5.10.4 Data acquisition system 84

6 Data analysis **87**

6.1 Result of simultaneous detection of phonon and scintillation 87

6.2 Discrimination of alpha and beta/gamma events 90

6.3 Light signal analysis 92

6.3.1 Resolution of light signal 92

6.3.2 Energy calibration in the light channel 95

6.4 Heat signal analysis 99
6.4.1 Resolution of heater's signal 99
6.4.2 Resolution of alpha events 103
6.5 Position dependence 105
6.6 Intrinsic resolution of CaF_2(Eu) scintillating bolometer 108
6.7 Comparison of waveforms of different signal heights 111
6.8 Possibility of an unknown mechanism in detector system 114
6.9 Interpretation of position dependence 116
6.9.1 Spin system in CaF_2(Eu) 116
6.9.2 Spin-lattice interaction to position dependence 116
6.10 The complete mechanism of CaF_2(Eu) scintillating bolometer 121

7 Conclusion **123**

8 Future prospect **125**

9 Acknowledgments **126**

1 Neutrinos

1.1 Existence of neutrino

Neutrino is a fundamental particle in the current Standard Model. Its history can be reviewed from 1890s. In 1896, Henri Becquerel discovered evidence of radioactivity in uranium and subsequently Marie Curie and Pierre Curie successfully observed it in thorium. The observed radioactivity was identified as alpha and beta rays, based on penetration ability of objects. In 1900, a new type of radiation with higher penetration was found by Paul Villard and named as gamma rays. In nuclear decays, alpha and gamma rays have a narrow energy distribution, but beta decays have a continuous energy spectrum which means some energy is lost in the beta decay process. However, energy conservation law must be true in any physical process. To explain beta decay's spectrum, Wolfgang Pauli suggested a three-body process, in which neutrino was emitted together with beta ray and proton:

$$n \to p + e + \bar{\nu_e}. \tag{1}$$

Neutrino was thought to take away a part of energy, momentum and angular momentum from beta decay process, and it interacted with matter so weak that it hadn't been observed in the experiments.

Detection of this ghost particle annoyed physicists for nearly 20 years until Cowan-Reines neutrino experiment was carried out. In nuclear reactor, nuclear fission occurs emitting neutrons and quickly undergoes beta decays. This process produces a lot of beta rays, anti-neutrinos and gamma rays. The anti-neutrinos have a certain probability of interacting with protons to produce neutrons and positrons:

$$\bar{\nu_e} + p \to n + e^+. \tag{2}$$

Kinetic energy of positron is absorbed by surrounding material and finally annihi-

lates with an electron emitting two gamma rays. This two gammas have the same 511 keV energy but opposite directions. The neutron loses energy in water to become thermal neutron. The thermal neutron is captured by hydrogen while emitting a 2.2 MeV gamma ray:

$$n + H \rightarrow D + \gamma. \tag{3}$$

The coincidence of both events gives a unique signature of an anti-neutrino existence.

1.2 Neutrino flavors

In 1936, another charged Lepton "muon" was discovered by Carl D. Anderson and Seth Neddermeyer, while studying cosmic radiation. Muon has the same negative charge as electron, but its mass is 200 times heavier than the one of electron. Because muon could be created by accelerator in the pion decay process:

$$\pi^{\pm} \rightarrow \mu^{\pm} + (\nu/\bar{\nu}), \tag{4}$$

phycisists faced a problem of "Is the neutrino produced in this process same as the one in the beta decay?" At the same time, theoretical physicists needed an evidence of different types of neutrinos to introduce W boson to Fermi's theory. Fermi's theory of weak interaction worked well at low energy region, but broke down above 100 GeV. The break down of Fermi's theory can be avoided if a mediating boson was introduced, W boson. The introduction of W boson provides the correct calculation of the branch ratio $(\mu \rightarrow e + \gamma)/(\mu \rightarrow e + \nu + \bar{\nu})$. If there is only one type of neutrino, the theoretical value of the branch ratio is at the order of 10^{-4}. However, the measured value by the experiment was less than 10^{-8}. Two different types of neutrinos were necessary to support the theory.

To verify if the neutrinos are different, Leon M. Lederman, Melvin Schwartz and Jack Steinberger carried out the AGS neutrino experiment at Brookhaven [1] . They used accelerator to generate a 15 GeV proton beam. The proton beam struck

beryllium target and produced pions, where it decays into muons and neutrinos. The neutrinos, muons and surviving pions crashed into a 13 m thick steel shield, where it stopped all particles down to 10^{-24} except neutrinos. These neutrinos went into a 10 tons aluminum spark chamber behind steel shield and interacted with matter to produce muons or electrons. If there is only one type of neutrino, electrons will be generated and produce distinct showers in the spark chamber. If there are two different types of neutrinos, muons can be created and produce tracks in the chamber.

$$\nu + n \rightarrow p + e^{-}; \tag{5}$$

$$\nu + n \rightarrow p + \mu^{-}. \tag{6}$$

After 3.48×10^{17} protons were fired at the target, 113 events were found to match the experimental conditions. In the 113 events, 34 events were single muon events, in which 5 events were considered as cosmic muons. Only 6 showers events were observed. This result proved neutrinos can have two different types, thus proving the existence of muon neutrinos.

The third generation tau was discovered by Martin Lewis Perl between 1974 and 1977 [2]. They used $e^{+} - e^{-}$ colliders to find 64 events of the form

$$e^{+} + e^{-} \rightarrow e^{\pm} + \mu^{\pm} + \geq 2\,\text{undetected particles}. \tag{7}$$

The undetected particles were not electrons, muons, photons or hadrons and were verified as a pair of new leptons. As the same as muons, taus also have their corresponding neutrinos. In 2001, the DONUT experiment successfully found evidence of four tau neutrino interactions with an estimated background of 0.34 events [3]. That number is consistent with the Standard Model expectation.

In this way, neutrinos have three types: electron neutrino, muon neutrino and tau neutrino, which are also known as three flavors, in the Standard Model. All of

the neutrinos are neutral with half-integer spin. The neutrinos are considered to be massless in the Standard Model until the discovery of neutrino oscillation.

1.3 Neutrino oscillation

In the late 1960s, astrophysicists Raymond Davis, Jr. carried out an experiment to collect and counted electron neutrinos emitted by nuclear fusion taking place in the Sun [4]. They chose perchloroethylene as target of neutrino capture reaction:

$$\nu_e + {}^{37}\mathrm{Cl} \rightarrow {}^{37}\mathrm{Ar} + \mathrm{e}^{-}. \tag{8}$$

Through collection of ^{37}Ar atoms, they could determine how many neutrinos had been captured. However, in his experiment he only observed $1/3 - 1/2$ number of events predicted by John N. Bahcall using the Standard Solar Model. The experiment and the Standard Solar Model were investigated again, but no anomaly could be found, which means the deficit of electron neutrinos arises from neutrino's inherent characteristics. Now this characteristics is known as neutrino oscillation, in which the probability of measuring a particular flavor of neutrinos varies between 3 mass eigenstates as it propagates through space. Neutrino oscillation was verified by some independent experiments, such as solar neutrino experiments [5] , atmospheric neutrino experiments [6] , reactor neutrino experiments [7, 8, 9] and long-baseline accelerator neutrino experiments [10] .

In neutrino oscillation, neutrinos must have none-zero mass and the flavors of neutrino are represented as a mixing of neutrino mass eigenstates:

$$|\nu_\alpha >= \sum_{i=1}^{3} U_{\alpha i} |\nu_i >, \tag{9}$$

where ν_i indicates three mass eigenstates, and the U is known as Pontecorvo-Maki-

Nakagawa-Sakata (PMNS) matrix, written as

$$U = \begin{bmatrix} 1 & 0 & 0 \\ 0 & c_{23} & s_{23} \\ 0 & -s_{23} & c_{23} \end{bmatrix} \begin{bmatrix} c_{13} & 0 & s_{13}e^{-i\delta} \\ 0 & 1 & 0 \\ -s_{13}e^{i\delta} & 0 & c_{13} \end{bmatrix} \begin{bmatrix} c_{12} & s_{12} & 0 \\ -s_{12} & c_{12} & 0 \\ 0 & 0 & 1 \end{bmatrix} \begin{bmatrix} e^{i\alpha_1/2} & 0 & 0 \\ 0 & e^{i\alpha_2/2} & 0 \\ 0 & 0 & 1 \end{bmatrix}, \tag{10}$$

where $c_{ij} = cos\theta_{ij}$, $s_{ij} = sin\theta_{ij}$, and δ is a CP violation phase factor. The α_1 and α_2 are Majorana phase factors which are meaningful only if neutrinos are Majorana particles. To image neutrino oscillation easily, we can just consider neutrinos have only two generations, electron neutrino ν_e and muon neutrino ν_μ. In this case, matrix element has just one mixing angle θ and states of electron and muon neutrinos can be written as:

$$\begin{aligned} |\nu_e> &= \cos\theta\,|\nu_1> + \sin\theta\,|\nu_2> \\ |\nu_\mu> &= -\sin\theta\,|\nu_1> + \cos\theta\,|\nu_2> . \end{aligned} \tag{11}$$

When electron neutrino propagates in vacuum, we consider it as a plate wave and its state can be written as:

$$|\nu_e(t)> = \cos\theta\,|\nu_1>\,\mathrm{e}^{-\mathrm{iE_1t}} + \sin\theta\,|\nu_2>\,\mathrm{e}^{-\mathrm{iE_2t}}, \tag{12}$$

where $E_j = \sqrt{p^2 + m_j^2} =\simeq p + \frac{m_j^2}{2E}$. Therefore, the probability of electron neutrino ν_e changing to muon neutrino ν_μ at time t is

$$\begin{aligned} P(\nu_e \to \nu_\mu : t) &= |<\nu_\mu|\nu_e(t)>| = |\sin\theta\cos\theta(1 - \mathrm{e}^{-\mathrm{i(E_1-E_2)t}})|^2 \\ &= \sin^2 2\theta \sin^2 \frac{\Delta \mathrm{m}^2}{4\mathrm{E}} \mathrm{L} = \sin^2 2\theta \sin^2 1.27 \frac{\Delta \mathrm{m}^2(\mathrm{eV})^2}{\mathrm{E(GeV)}} \mathrm{L(km)}, \end{aligned} \tag{13}$$

where $\Delta m^2 = |m_1^2 - m_2^2|$ is the squared difference of neutrino mass eigenstates, and $L = ct$ is the distance from neutrino source to detector. Because neutrinos

have mass, we observed less neutrinos from the Sun and oscillation phenomena from reactor neutrino oscillation experiments. Conversely, we can change distance of detector from source and measure the mixing angles and the squared differences of neutrino mass eigenstates. The neutrino mixing parameters (for normal mass hierarchy) are list as below [11].

1. $\sin(\theta_{12}) = 0.307 \pm 0.013$.
2. $\Delta m^2_{12} = (7.53 \pm 0.18) \times 10^{-5}\,\mathrm{eV}^2$.
3. $\sin(\theta_{23}) = 0.536^{+0.023}_{-0.028}$.
4. $\Delta m^2_{32} = (-2.55 \pm 0.04) \times 10^{-3}\,\mathrm{eV}^2$.
5. $\sin(\theta_{13}) = 0.0218 \pm 0.0007$.
6. $\delta = 1.37^{+0.18}_{-0.16}\,\pi\,\mathrm{rad}$.

Neutrino oscillation proved that neutrinos have none-zero mass, but cannot give the information of absolute neutrino mass scale. One of approaches for the neutrino mass is neutrinoless double beta decay search. This decay process is possible if the neutrinos are Majorana particles, which means neutrino and anti-neutrino in each flavor are the same particle. The Majorana mass determines the probability of neutrinoless double beta decay, so we can measure its half-life to estimate the neutrino mass scale. The best limit of effective Majorana mass is given by KamLAND-Zen experiment [12] as:

$$< m_{\beta\beta} >= |\sum_{i=1}^{3} U_{ei}^2 m_i| < 61 - 165\,\mathrm{meV}. \tag{14}$$

Recently, neutrinoless double beta decay search has been already one of the featured physics experiments in the world.

2 Neutrinoless Double beta decay

2.1 Double beta decay

Double beta decay ($2\nu\beta\beta$) was first discussed by M. Goeppert-Mayer in 1935 [13]. $2\nu\beta\beta$ is nuclear transition in which an initial nucleus (Z-2, A) with proton number Z-2 and total nucleon number A decays to (Z, A). In this process, the initial nucleus emits two electrons and two antineutrinos at the same time,

$$(Z-2, A) \rightarrow (Z, A) + 2e^- + 2\bar{\nu}_e. \tag{15}$$

This decay process occurs if the isotope has a lower binding energy of the initial nucleus (Z-2,A) than the one of the final nucleus (Z,A), while transition from nucleus (Z-2,A) to nucleus (Z-1,A) is forbidden by energy conversion law (Fig.1).

This decay process is allowed by the Standard Model with lepton number conversion, no matter if neutrinos are Dirac or Majorana. $2\nu\beta\beta$ has been already observed for some nucleus in Table.1. The half-lives of $2\nu\beta\beta$ isotopes are $10^{18} \sim 10^{21}$ years indicating $2\nu\beta\beta$ is a very rare nuclear decay process.

In addition to $2\nu\beta\beta$, there are some other decay process that can occur from nucleus (Z+2,A) to nucleus (Z,A), such double beta-plus decay, single beta-plus electron capture and double electron capture:

$$\begin{aligned} \beta^+\beta^+\text{mode} &: (\mathrm{Z}+2, \mathrm{A}) \rightarrow (\mathrm{Z}, \mathrm{A}) + 2\mathrm{e}^+ + 2\nu_\mathrm{e}, \\ \beta^+/EC\text{mode} &: (\mathrm{Z}+2, \mathrm{A}) + \mathrm{e}^- \rightarrow (\mathrm{Z}, \mathrm{A}) + \mathrm{e}^+ + 2\nu_\mathrm{e} + \mathrm{X\,ray}, \\ EC/EC\text{mode} &: (\mathrm{Z}+2, \mathrm{A}) + 2\mathrm{e}^- \rightarrow (\mathrm{Z}, \mathrm{A}) + 2\nu_\mathrm{e} + 2\,\mathrm{X\,rays}. \end{aligned} \tag{16}$$

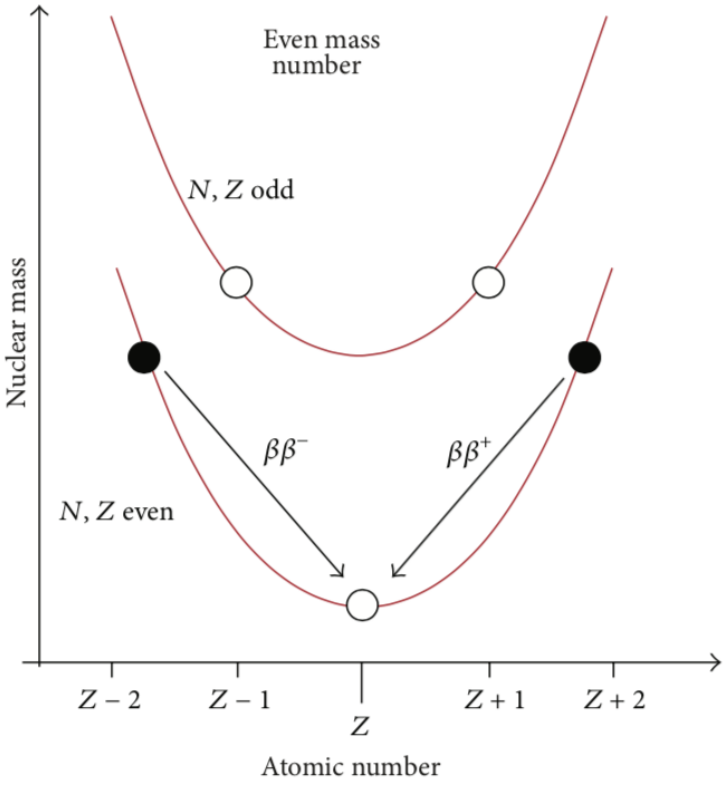

Figure 1: Nuclear mass as a function of the atomic number Z in the case of an isobar candidate with even mass number A [14].

Table 1: Observed $2\nu\beta\beta$ nuclei.

Nuclide	Half-life, 10^{21} years	Experiment	Reference
^{48}Ca	$0.064\,^{+0.007}_{0.006}\pm^{+0.012}_{-0.009}$	NEMO-3	[15]
^{76}Ge	$1.84^{+0.14}_{-0.10}$	GERDA	[16]
^{82}Se	$9.39 \pm 0.17 \pm 0.58 \times 10^{-2}$	NEMO-3	[17]
^{96}Zr	$2.35 \pm 0.14 \pm 0.16 \times 10^{-2}$	NEMO-3	[18]
^{100}Mo	$6.81 \pm 0.01\,^{+0.38}_{-0.40} \times 10^{-3}$	NEMO-3	[19]
^{116}Cd	$2.6\,^{+0.9}_{-0.5} \times 10^{-2}$	ELEGANT V	[20]
^{130}Te	$8.2 \pm 0.2 \pm 0.6 \times 10^{-1}$	CUORE-0	[21]
^{136}Xe	$2.165 \pm 0.016 \pm 0.059$	EXO-200	[22]
^{150}Nd	$9.11\,^{+0.25}_{-0.22} \pm 0.63 \times 10^{-3}$	NEMO-3	[23]

2.2 Neutrinoless double beta decay

If neutrinos are Majorana particle that means neutrino and anti-neutrino are the same particle, there is a possibility that nucleus (Z-2,A) emits two electrons, but without any anti-neutrinos:

$$(Z-2, A) \rightarrow (Z, A) + 2e^{-}. \tag{17}$$

This decay process can be imaged as a light neutrino exchange, a nucleon absorbs the anti-neutrino emitted by another nucleon (Fig.2). The exchanged neutrino are virtual particles caused by none-zero mass of neutrinos.

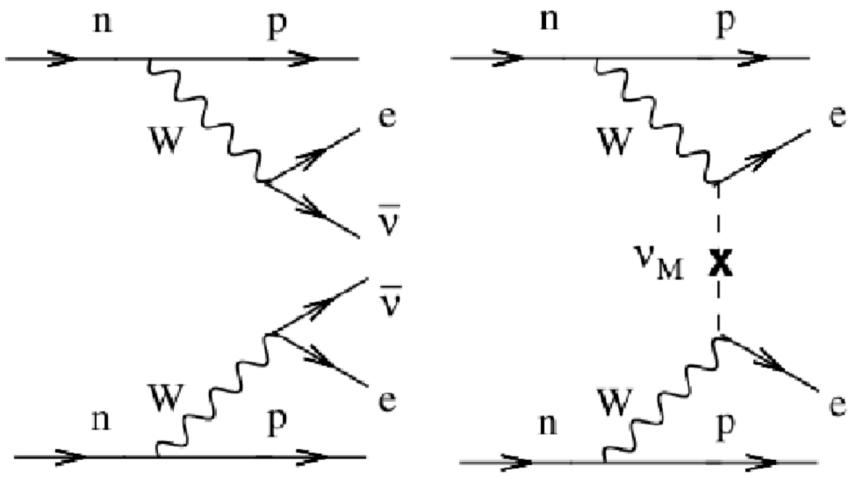

Figure 2: Feynman diagram for $2\nu\beta\beta$ (left) and $0\nu\beta\beta$ (right) [24].

The $0\nu\beta\beta$ process violates lepton number conservation and is forbidden in the Standard Model. However, it is an executable way to prove the Majorana nature of neutrinos. And if neutrinos are Majorana particle, the alternative neutrinoless decay modes are also possible:

$$\begin{aligned} \beta^{+}\beta^{+}\text{mode} &: (\mathrm{Z}+2, \mathrm{A}) \rightarrow (\mathrm{Z}, \mathrm{A}) + 2\mathrm{e}^{+}, \\ \beta^{+}/EC\text{mode} &: (\mathrm{Z}+2, \mathrm{A}) + \mathrm{e}^{-} \rightarrow (\mathrm{Z}, \mathrm{A}) + \mathrm{e}^{+} + \mathrm{X\,ray}, \\ EC/EC\text{mode} &: (\mathrm{Z}+2, \mathrm{A}) + 2\mathrm{e}^{-} \rightarrow (\mathrm{Z}, \mathrm{A}) + 2\,\mathrm{X\,rays}. \end{aligned} \tag{18}$$

The probability of neutrino exchange is suppressed by (m/E) in theory. The three mass eigenstates of neutrinos will contribute to this process, so the effective Majorana mass can be written as:

$$< m_{\beta\beta} >= |\sum_{i=1}^{3} m_i U_{ei}^2|, \tag{19}$$

where the U_{ei} is the PMNS matrix, m_i is the eigenvalue of each mass eigenstate of neutrinos.

The half-life of $0\nu\beta\beta$ decay with light Majorana neutrinos exchange is expressed as follows:

$$\frac{1}{T_{1/2}^{0\nu}} = g_A^4 G^{0\nu} |M^{0\nu}|^2 (\frac{m_{\beta\beta}}{m_e})^2 \tag{20}$$

where $g_A = 1.27$ is the axial-vector weak coupling for free nucleon, $G^{0\nu}$ is the known phase-space factor, $M^{0\nu}$ is the nuclear matrix element (NME) and m_e is the mass of electron. The phase-space factor of each $0\nu\beta\beta$ isotope candidate is given in Fig.3.

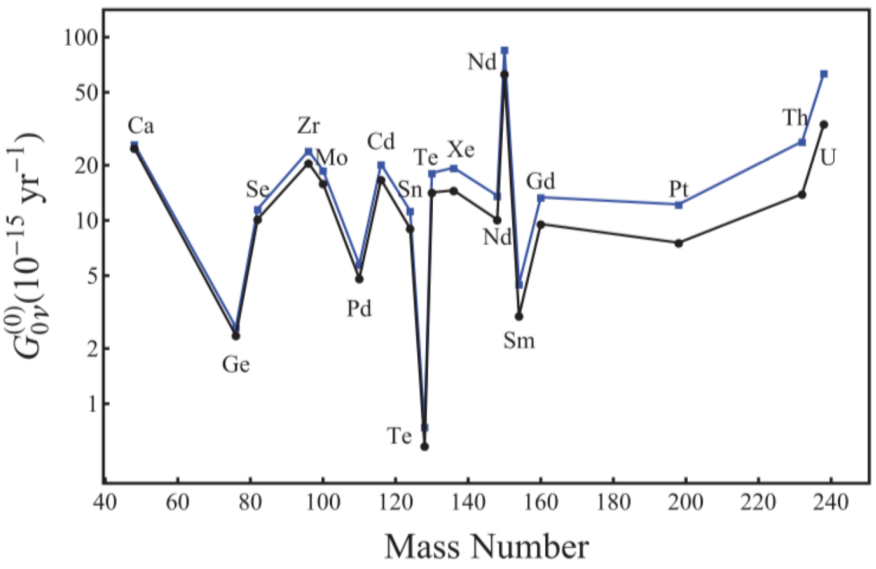

Figure 3: Phase space factors $G_{0\nu}$ in units of 10^{-15} year^{-1}. The blue points are from [25] , and the black points are from [26] .

The NME values have large uncertainties in the calculation by different methods

as shown in Fig.4. The methods include quasiparticle random phase approximation (QRPA) [27] , interacting shell model [28] , angular momentum projected Hartree-Fock-Bogoliubov method (PHFB) [29] , interacting boson model (IBM) [30] and energy density functional method (EDF) [31] . In the $0\nu\beta\beta$ decay search, the mean value of different models should be used to reduce the NME uncertainties. Since the NME value fluctuates within one order of magnitude, we can understand the $T^{0\nu}_{1/2} \times m^2_{\beta\beta}$ is roughly equal to 10^{30} year·meV^2. If $< m_{\beta\beta} >$ is 20 meV, the half-life of $0\nu\beta\beta$ decay is as long as 10^{28} years; If $< m_{\beta\beta} >$ is 2 meV, the half-life of $0\nu\beta\beta$ decay will be in the order of 10^{30} years.

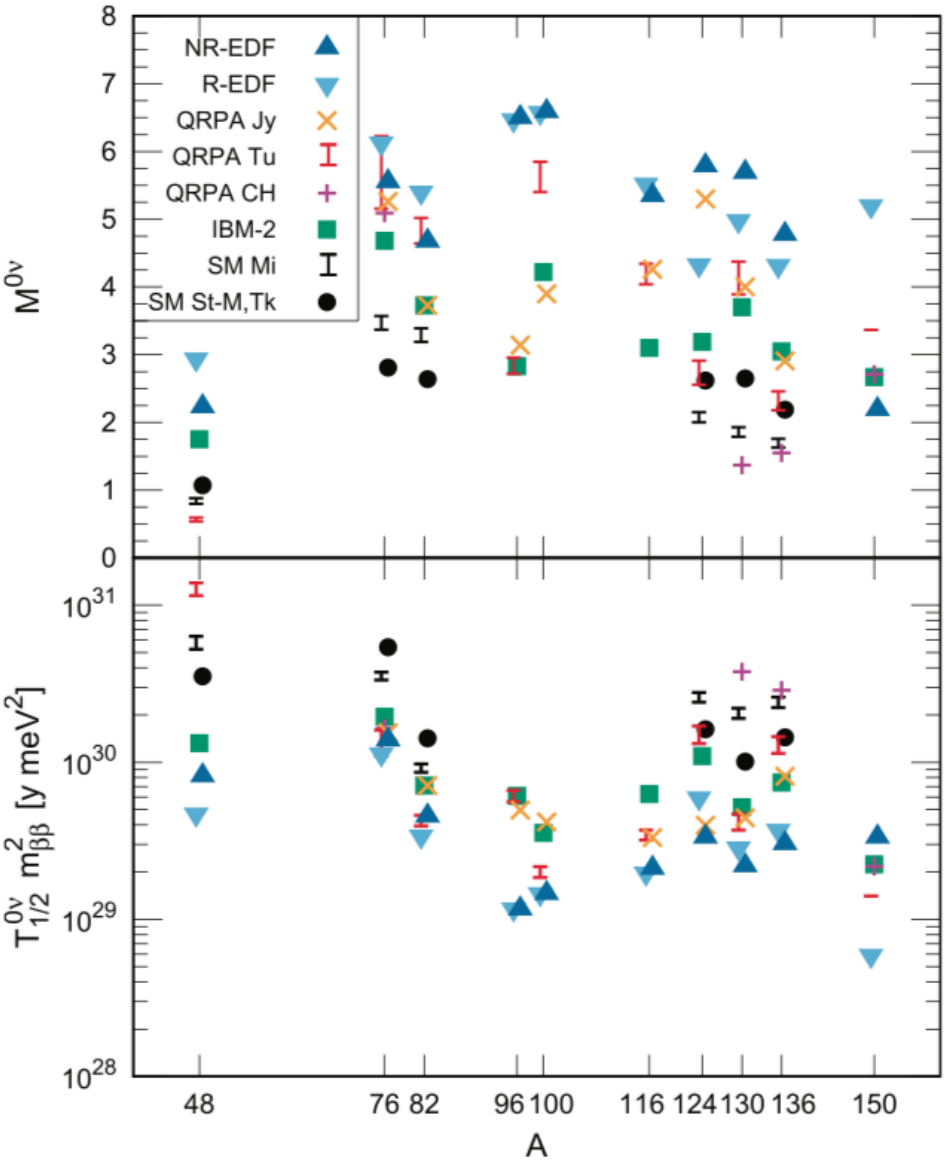

Figure 4: Top panel: nuclear matrix elements ($M_{0\nu}$) for $0\nu\beta\beta$ decay candidates as a function of mass number A. Bottom panel: associated $0\nu\beta\beta$ decay half-lives, scaled by the square of the unknown parameter $m_{\beta\beta}$. The plotted results are introduced in [32].

2.3 Detection of neutrinoless double beta decay

Detection of $0\nu\beta\beta$ decay is to find a peak at the end point of the $2\nu\beta\beta$ decay spectrum. In $2\nu\beta\beta$ decay, two anti-neutrinos take away a part of decay energy from emitted electrons, so $2\nu\beta\beta$ decay has a continuous spectrum with an end point at $Q_{\beta\beta}$ value. However, $0\nu\beta\beta$ decay doesn't emit neutrinos, so $0\nu\beta\beta$ decay is mono-energetic nuclear transition that would make a single peak at the $Q_{\beta\beta}$ region (Fig.5).

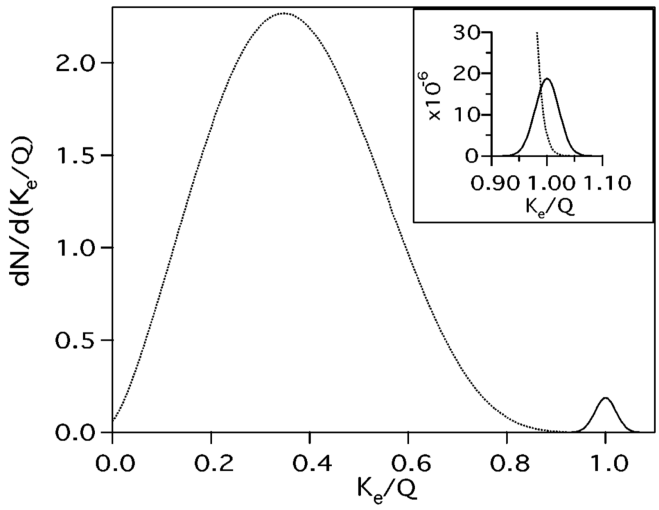

Figure 5: Illustration of the spectra of the sum of the electron kinetic energies K_e (Q is the endpoint) for the $\beta\beta(2\nu)$ normalized to 1 (dotted curve) and $\beta\beta(0\nu)$ decays (solid curve) [33]. The $\beta\beta(0\nu)$ spectrum is normalized to 10^{-2} (10^{-6} in the inset). Both spectra use an energy resolution of 5%.

From Fig.5, we can understand several parameters are very important for $0\nu\beta\beta$ decay search. The first parameter is the number of $0\nu\beta\beta$ isotopes. Since the half-life of $0\nu\beta\beta$ decay is predicted to be longer than 10^{26} years, we have to prepare at least 100 kg target to observe one event in a year.

The second parameter is the energy resolution of detector. In actual measurement, some backgrounds could happen in the $0\nu\beta\beta$ decay region. Good energy resolution can shrink the region of interest (ROI) to reduce the effect of background, especially the high-energy tail of the $2\nu\beta\beta$ decay events. The fraction F of the $2\nu\beta\beta$

counts in the $0\nu\beta\beta$ region can be approximated by

$$F = \frac{7Q\delta^6}{m_e}, \tag{21}$$

where $\delta\,(= \Delta E/Q)$ is the FWHM energy resolution expressed as a fraction and m_e is the electron mass [33] . The coefficient 7 is for a resolution of 5%. This coefficient depends moderately on resolution and is 9 at 0.5%. An expression for the $0\nu\beta\beta$ signal S to $2\nu\beta\beta$ background B ratio then can be written as

$$\frac{S}{B} = \frac{m_e}{7Q\delta^6}\frac{T^{2\nu}_{1/2}}{T^{0\nu}_{1/2}}. \tag{22}$$

This calculation indicates that good resolution is critical to neutrinoless double beta decay search. In the assumption that the half life of $0\nu\beta\beta$ decay is 10^6 times longer than that of $2\nu\beta\beta$ decay, for the ^{48}Ca isotope candidate with $Q_{\beta\beta} = 4.27\,\mathrm{MeV}$ with a 5% energy resolution, the ratio of signal to background S/B is equal to 1.09. In the case of 0.5% energy resolution, the S/B is 10^5 which means $2\nu\beta\beta$ background is negligible for $0\nu\beta\beta$ experiment.

The third parameter is $Q_{\beta\beta}$ value. From equation (22), we can know there are less $2\nu\beta\beta$ background when we use the $0\nu\beta\beta$ isotope candidate with a higher $Q_{\beta\beta}$ value. Also, the hardest γ rays emitted from the natural radioactive nuclei are those belonging to ^{208}Tl, of 2.61 MeV energy, while β emission from the same sources don't exceed the energy of 3.27 MeV (^{214}Bi). Therefore, the isotope candidates with $Q_{\beta\beta}$ higher than 3.27 MeV are preferred for $0\nu\beta\beta$ decay experiments. The $Q_{\beta\beta}$ values and the natural abundances of some $0\nu\beta\beta$ isotopes are list in the table.2.

Table 2: $Q_{\beta\beta}$ value and natural abundance of each $0\nu\beta\beta$ isotope.

Decay candidate	$Q_{\beta\beta}$ value (MeV)	natural abundance %
^{48}Ca	4.271	0.187
^{76}Ge	2.040	7.8
^{82}Se	2.995	9.2
^{96}Zr	3.350	2.8
^{100}Mo	3.034	9.6
^{116}Cd	2.802	7.5
^{130}Te	2.533	34.5
^{136}Xe	2.479	8.9
^{150}Nd	3.367	5.6

2.4 Sensitivity of $0\nu\beta\beta$ experiment

Let's consider an experiment with a total exposure Mt, where M is the mass of the $0\nu\beta\beta$ isotope, t is the data-taking time. In the approximation $T^{0\nu}_{1/2} \gg t$, the radioactive law for the rare process can be written as

$$N(t) \sim N_0(1 - \ln 2 \cdot \frac{\mathrm{t}}{\mathrm{T}^{0\nu}_{1/2}}), \tag{23}$$

where N_0 is the number of $0\nu\beta\beta$ isotopes at $t = 0$. This equation is allowed by the current limits on $0\nu\beta\beta$ half-lives of order 10^{24} or greater. As a consequence, the number of $0\nu\beta\beta$ decay during the data-taking time t is

$$N = \log 2 \, \frac{\epsilon \cdot \mathrm{M} \cdot \mathrm{N_A}}{\mathrm{W}} \frac{\mathrm{t}}{\mathrm{T}^{0\nu}_{1/2}}, \tag{24}$$

where W is its molar mass, N_A is the Avogadro constant and ϵ is the detection efficiency.

In the case of zero-background case, the sensitivity for $0\nu\beta\beta$ decay can be expressed as

$$T^{0\nu}_{1/2} = \log 2 \, \frac{\epsilon \cdot \mathrm{M} \cdot \mathrm{N_A}}{\mathrm{W}} \mathrm{t}. \tag{25}$$

If no event is observed in the experiment, the upper limit with a certain confidence level can be written as

$$T^{0\nu}_{1/2} \geq \frac{\log 2}{n_{CL}} \, \frac{\epsilon \cdot M \cdot N_A}{W} t, \tag{26}$$

where n_{CL} is the upper number in the Poisson distribution for certain expected number of background events, number of measured events in the $Q_{\beta\beta}$ region, and confidence level. For example, $n_{CL} = 2.44$ for 90% confidence level in case that expected background number and number of measured event are zero [34] .

In most of experiments, a number of background events are remaining in the region of interest (ROI). In the large background case, the standard deviation of the

number of background events is proportional to $B^{1/2}$, where B is the background number in the ROI. In the case of a flat background distribution, the sensitivity of the experiment can be expressed as

$$T^{0\nu}_{1/2} \geq \frac{\log 2}{n_\sigma \cdot B^{1/2}} \frac{\epsilon \cdot M \cdot N_A}{W} t, \tag{27}$$

where n_σ is a certain confidence level in unit of σ. In the case that a detector having an energy resolution ΔE, target mass M and background level b during data-taking time t, the background B is expressed as

$$B = b \cdot \Delta E \cdot M \cdot t, \tag{28}$$

where b is in the unit of counts/(keV·kg·year). The equation (27) can be written as

$$T^{0\nu}_{1/2} \geq \frac{\log 2 \cdot \epsilon \cdot \mathrm{N_A}}{n_\sigma \cdot W} \sqrt{\frac{M \cdot t}{b \cdot \Delta E}}. \tag{29}$$

We can summarize the above calculations to a simple expression. When there is no event observed in the $Q_{\beta\beta}$ region, the sensitivity

$$T^{0\nu}_{1/2} \propto M \cdot t, \tag{30}$$

while a number of background events are remaining in the $Q_{\beta\beta}$ region and have a flat distribution, the sensitivity will decline as

$$T^{0\nu}_{1/2} \propto \sqrt{\frac{M \cdot t}{b \cdot \Delta E}}. \tag{31}$$

The experimental sensitivity to effective Majorana neutrino mass is expressed as

$$< m_{\beta\beta} > \propto (\frac{1}{M \cdot t})^{1/2} \tag{32}$$

in the case of zero-background measurement environment, and

$$< m_{\beta\beta} > \propto (\frac{b \cdot \Delta E}{M \cdot t})^{1/4} \tag{33}$$

for a number of background events remaining in ROI. Consequently, a zero-background measurement is an efficient way for a successful $0\nu\beta\beta$ experiment.

3 Detection technologies for neutrinoless double beta decay search

Until now, several detection technologies are developed for the $0\nu\beta\beta$ decay search, listed as below.

- Large liquid scintillator detector.
- Germanium detector.
- Tracking detector.
- Scintillating bolometer.

The large liquid scintillator detector employs the scintillation mechanism to detect scintillation light induced by radiation, such as KamLAND-Zen, SNO+ [35]; Germanium Detector is a semi-conductor detector that measures the charge generated by radiation under applied voltage [36]; Tracking detector records the track of beta ray in a magnetic field [37]; Scintillating bolometer applied low temperature technologies to detect phonon and scintillation light generated by radiation simultaneously [38, 39]. Detection technologies are introduced in detail in the following subsections.

3.1 Large liquid scintillator detector

Liquid scintillator detector employs liquid scintillator as the target for radiation detection. When radiation deposits energy in liquid scintillator, a part of energy will transform to scintillation energy. The scintillation mechanism can be considered as a result of molecular transitions in Fig.6. The ground state of the molecule is at the point A_0, which is the minimum of the potential energy. The deposit energy of radiation raises the molecule to an excited state, such as $A_0 \rightarrow A_1$. The position A_1 is not the minimum energy point in the excited state, so the molecule will release energy through lattice vibrations (heat or phonons) and move to point B_1. In

general, the decay time of excited state is a few ns, so the molecule will undergo the transition $B_1 \rightarrow B_0$ immediately with an emission photon of energy equal to $E_{B1} - E_{B0}$.

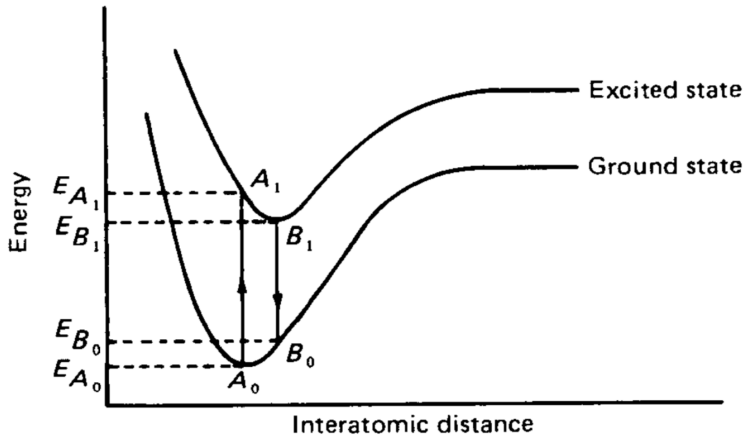

Figure 6: A typical energy diagram of a molecule [40].

If we dissolve $0\nu\beta\beta$ isotopes into liquid scintillator, it can be used as a calorimeter detector for $0\nu\beta\beta$ experiments. The KamLAND-Zen experiment employs ^{136}Xe gas as the $0\nu\beta\beta$ target and dissolves Xe gas into liquid scintillator. The SNO+ experiment employs ^{130}Te as the $0\nu\beta\beta$ target and dissolve organics with Te component into liquid scintillator as a $0\nu\beta\beta$ detector.

Merit of liquid scintillator detectors for $0\nu\beta\beta$ search is the detector structure's simplicity. A simple detector structure is easy to scale up and finally results in a large target mass. For example, the KamLAND-Zen experiment contains 800 kg ^{136}Xe in the liquid scintillator. However, liquid scintillator detectors also have demerit of relatively worse energy resolution. In general, liquid scintillator's light yield is not higher than 10,000 photons/MeV. In addition to the quantum efficiency of PMT and light collection efficiency, the resolution of detector will be limited to 5-10% (FWHM). For example, the KamLAND-Zen experiment has a light output of a few 100 p.e./MeV and an energy resolution of 10% (FWHM) at the $Q_{\beta\beta}$.

The low energy resolution induces a serious background in the $Q_{0\nu}$ from the high

energy tail of $2\nu\beta\beta$ events. The $2\nu\beta\beta$ background will strongly limit experimental sensitivity. To reduce the $2\nu\beta\beta$ background, the only way is to improve the detector's resolution.

3.2 Germanium experiments

In current running $0\nu\beta\beta$ experiments, the best resolution was achieved by germanium detectors in the GERDA and Majorana experiments. The resolution of the GERDA experiment is 2.9 keV (FWHM), which is equal to 0.14% at the $Q_{\beta\beta}$ and the one of the Majorana experiment is 2.4 keV (FWHM), which is equal to 0.12% at the $Q_{\beta\beta}$.

The operation of germanium detector is based on the properties of p-n junction with reverse bias, shown in Fig.7. When incident radiation deposits energy higher than the band gap in the germanium, pairs of electron and hole are created. The electrons and holes will propagate to the cathode and anode by the electric field, respectively. With proper electronics, the charge collected produces a pulse that can be recorded. The resolution of germanium detector depends on the band gap energy and the number of electron and hole carriers. For example, a 4 MeV alpha particle deposits all energy in a germanium detector. The band gap energy of germanium is 3.0 eV. Therefore, 1×10^6 electron-hole carriers will be generated. The statistical deviation is 0.1%, equal to 4 keV.

The high resolution of germanium detectors can narrow the $0\nu\beta\beta$ window and result in a low background measurement. Presently GERDA is the only experiment that is able to achieve the zero-background measurement environment. In addition, germanium detectors allow to discriminate between single-site (electron-like) and multi-site (γ-like) energy releases. They can achieve a background rate as low as $0.001\,\mathrm{counts}/(\mathrm{keV}\cdot\mathrm{kg}\cdot\mathrm{y})$, even though $Q_{\beta\beta}$ is 2039 keV which is lower than ^{208}Tl's 2.6 MeV gamma rays.

However, germanium detectors also have a demerit for the $0\nu\beta\beta$ search. They

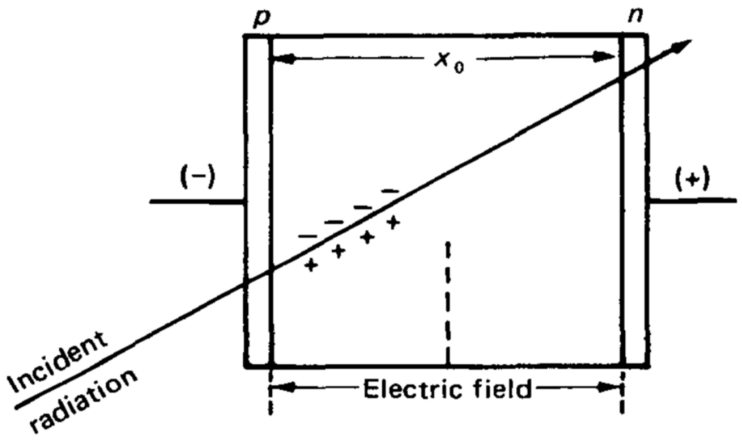

Figure 7: A p-n junction with reverse bias operating as a detector [41].

can use germanium detector to search for $0\nu\beta\beta$ of ^{76}Ge, but cannot be used for other $0\nu\beta\beta$ candidates. The discovery of $0\nu\beta\beta$ decay should be confirmed by different nucleus. In 2003, a germanium detector experiment, the Heidelberg-Moscow experiment, claimed the discovery of $0\nu\beta\beta$ decay [42]. However, the claim was denied by other $0\nu\beta\beta$ experiments. This historical incident tells us it's very important to confirm the observation of $0\nu\beta\beta$ decay using several different nuclide candidates. Therefore, a detector that can change the target sorts is preferred.

3.3 Tracker-Calorimeter: NEMO experiments

The one of most famous $0\nu\beta\beta$ experiment that studied many different $0\nu\beta\beta$ nuclide candidates is the NEMO-3 experiment. The NEMO-3 detector employed a tracking detector. Tracking detectors are different from other 0νDBD techniques because the source isotopes are not embedded inside the detector. The detection principle of the NEMO-3 tracker-calorimeter is shown in Fig.8. The $0\nu\beta\beta$ isotopes are deposited on foils, and the track and energy of the emitted electrons are measured by conventional gas detectors and calorimeters. This approach allows to investigate any isotope that can undergo double-beta decay, such as ^{48}Ca, ^{82}Se, ^{96}Zr, ^{100}Mo, ^{116}Cd, ^{130}Te and ^{150}Nd.

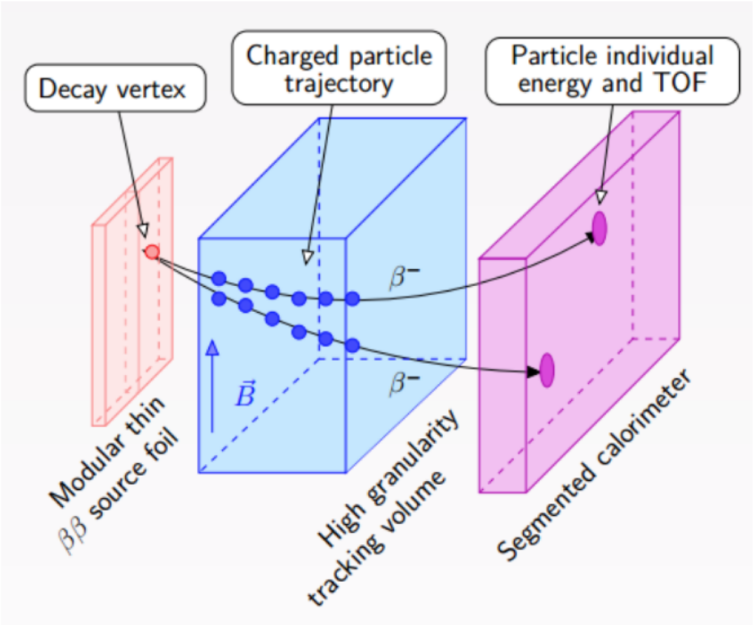

Figure 8: Detection principle of the NEMO-3 detector [37].

The reconstruction of the electron tracks provides excellent background suppression and allows to study the angular distribution of the decay. This feature would be very important to study decay mechanism alternative to the exchange of a light Majorana neutrino. However, the demerit of tracker-calorimeter is relatively poor detection efficiency, because part of the electrons energy is given in the source foils and can not be measured. For example, in the NEMO-3 experiment, beta rays above 2 MeV have only 10% detection efficiency.

In the $0\nu\beta\beta$ search, it is required to prepare at least 1 ton target source to search for the inverted hierarchy and 100 ton target source for the normal hierarchy. The 10% detection efficiency means they have to prepare more than 10 tons target source to explore the inverted hierarchy region. That is very difficult for current status of $0\nu\beta\beta$ experiments in the world.

3.4 Bolometer experiments

An excellent detector for the $0\nu\beta\beta$ search should achieve large target mass, high energy resolution, high detection efficiency and multi-target acceptability. The scintillating bolometer is considered as a promising detector for that request.

At first, let me introduce the detection principle of bolometer in Fig.9. Bolometer is an absorber thermally connected to a heat bath. When a radiation deposits energy E inside the absorber, the temperature of absorber will increase by E/C, where C is the absorber's heat capacity. At room temperature, the temperature increase by a 4 MeV energy deposit is just 5.0×10^{-16} K for a 300 g CaF_2 crystal. It's impossible to detect that temperature change. However, the dielectric crystal's heat capacity is written as

$$C = \frac{12}{5}\pi^4 N_A k_B (\frac{T}{\theta_D})^3, \tag{34}$$

where N_A is the Avogadro constant, k_B is the Boltzmann constant and θ_D is the Debye temperature of absorber. At low temperature of mK, the heat capacity of CaF_2 will decrease by 15 orders of magnitude from root temperature. For example, the temperature increase of a 300 g CaF_2 at 10 mK for a 4 MeV radiation is 14 mK, which is high enough to be measured.

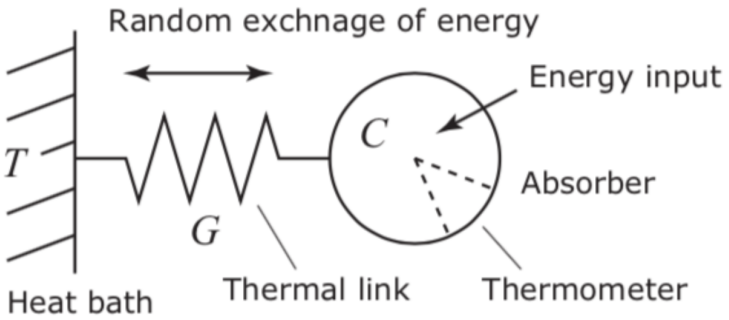

Figure 9: Detection principle of bolometer.

When we attach a thermometer on the absorber and cool them down to mK,

we can measure the temperature change $\Delta T = E/C_t$ as a signal in Fig.10. Here, C_t is the sum of the absorber's heat capacity C and the thermometer sensor's heat capacity C_s. Since the absorber is thermally connected to heat bath by a thermal link, the absorber's temperature will return asymptotically to the temperature of heat bath in a decay time τ. The scale of $\tau = C_t/G$, depending on the heat capacity and the thermal link's thermal conductance G.

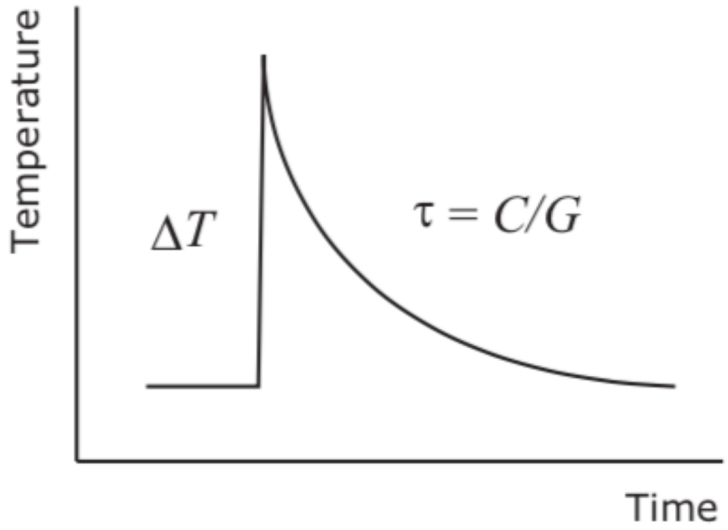

Figure 10: Scheme of signal output in low temperature measurement.

For an ideal case, the resolution of bolometer is limited by the thermodynamic fluctuation noise. The total thermal energy of the detector system can be written as $E = C_t T$. The energy of phonon is $\epsilon = k_B T$. Hence, the number of thermal quanta is $N = E/\epsilon = C_t/k_B$. The fluctuation of the thermal energy is

$$\Delta E_{rms} = \sqrt{N}\epsilon = \sqrt{C_t k_B T^2}. \tag{35}$$

The ΔE_{rms} is an intrinsic energy resolution limit of low temperature detector by thermodynamic fluctuation noise. In the case of 300 g CaF_2 crystal, the thermodynamic fluctuation noise is a few 10 eV at 20 mK. However, in the realistic condition, the resolution of low temperature detector is poorer than that value, because di-

lution refrigerator's vibration noise, electric noise of readout circuits will limit the final resolution. The CUORE $0\nu\beta\beta$ experiment achieved 6 keV (FWHM) at 2.6 MeV, equal to 0.2% (FWHM) resolution [43]. The AMoRE $0\nu\beta\beta$ experiment also achieved 10 keV (FWHM) at the ^{100}Mo's $Q_{\beta\beta} = 3.03MeV$, which is equal to 0.33% (FWHM) [44]. Therefore, this high resolution property of bolometer is satisfied with the requirements of $0\nu\beta\beta$ decay search experiments.

To achieve a low background measurement condition for $0\nu\beta\beta$ decay search, the technology of bolometer can be upgraded to scintillating bolometer. The scintillating bolometer consists of two bolometer systems in Fig.11, one is to detect phonons from the scintillation crystal; the other is to detect scintillation photons from the scintillation crystal. When we apply a scintillation crystal as the absorber of bolometer, a small part of energy from radiation will be emitted as scintillation photons. Scintillation photons have a well-known quenching property that alpha ray's light output is lower than that of beta/gamma ray. If we can detect phonons and scintillation photons at the same time, we can discriminate the alpha background from interested beta/gamma events as in Fig.12. This method is very useful for $0\nu\beta\beta$ decay search. The LUCIFER experiment, which used a ZnSe scintillating bolometer, has achieved 1 count/(ton·year) low background condition [45].

Through the above introduction, we have known the scintillating bolometer technology can achieve a good energy resolution and a low background measurement condition for $0\nu\beta\beta$ decay search. Besides those, this technology can also satisfy the requests of large mass, high detection efficiency and multi-target acceptability. The largest scintillating bolometer is developed by the CUORE experiment. It can contain 1000×5 cm cubic crystals, whose total mass is about 709 kg [46]. The detection efficiency is dependent of attenuation length of beta ray. For a 2.0 MeV beta ray in a general scintillation crystal, its range is about 1 mm. Hence, the detection efficiency is as high as about 70∼90%. Finally, one of the most important ability is

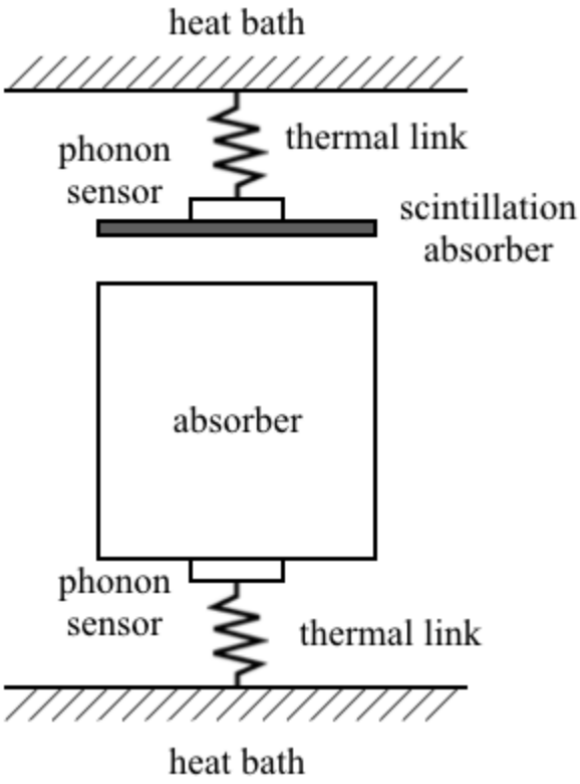

Figure 11: Scheme diagram of scintillating bolometer.

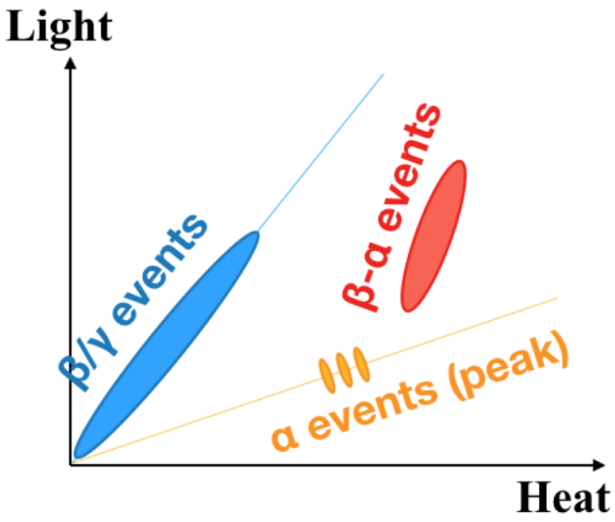

Figure 12: Background discrimination by simultaneous detection of heat and scintillation light.

multi-target acceptability. Since we can use any scintillation crystal as the absorber of scintillating bolometer, we can study different nuclei candidates of $0\nu\beta\beta$ decay. For example, the CUORE experiment is using TeO_2 crystal to study ^{130}Te's $0\nu\beta\beta$ decay [43], the LUCIFER experiment is using ZnSe crystal to study ^{82}Se [45] and the AMoRE experiment is using $CaMoO_4$ crystal to study ^{100}Mo [44].

Since scintillating bolometer technology is very promising for $0\nu\beta\beta$ decay search, our experiment group also plans to develop a scintillating bolometer to search for $0\nu\beta\beta$ decay of ^{48}Ca. In this thesis, I will describe my development process of a scintillating bolometer using a CaF_2(Eu) scintillation crystal.

4 Conceptualization of scintillating bolometer with a large CaF_2(Eu) scintillation crystal

4.1 Absorber selection for $0\nu\beta\beta$ decay of ^{48}Ca

This thesis focuses on an application of a scintillating bolometer to search neurinoless double beta decay of ^{48}Ca. An advantage in working with ^{48}Ca is because it has the largest $Q_{\beta\beta} = 4.27$ MeV (Fig.13). Neutrinoless double beta decay events are expected to fall in a region of the energy spectrum where the background is expected to be very low. The hardest γ rays emitted from the natural primordial radioactive nuclei belong to ^{208}Tl of 2.615 MeV energy, and β emissions from the same sources do not exceed the energy of 3.272 MeV (^{214}Bi).

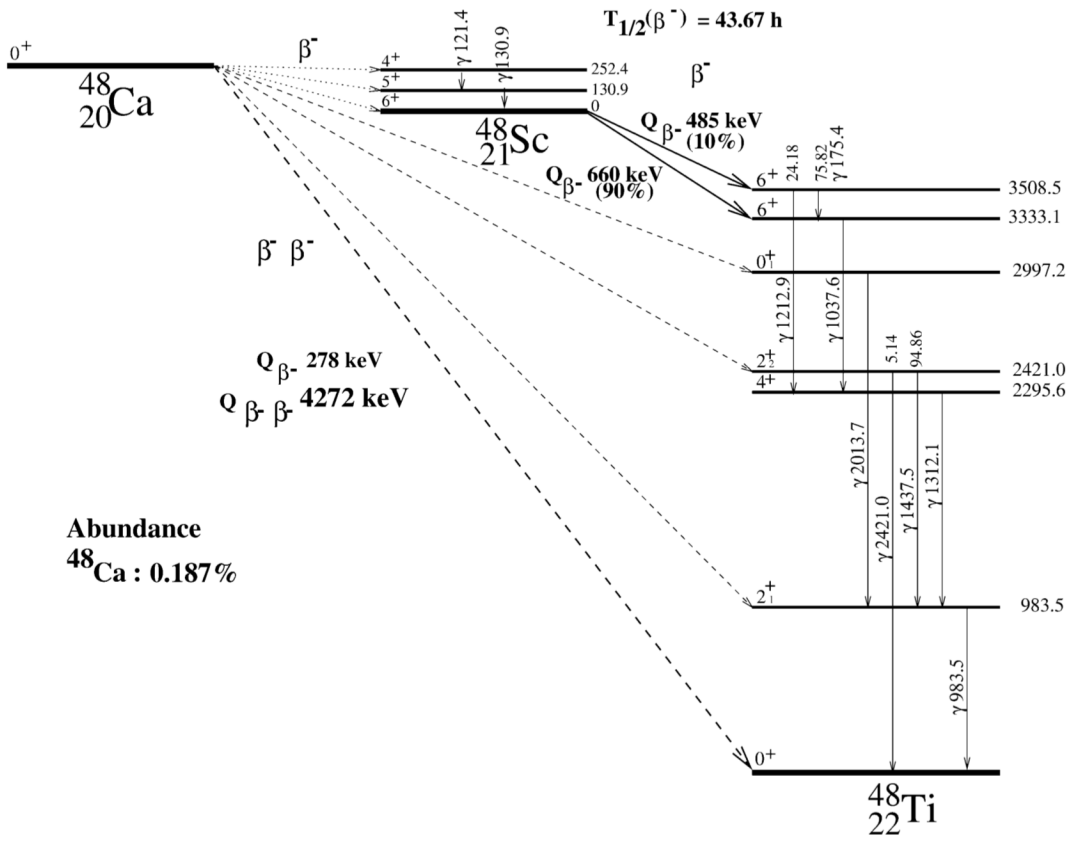

Figure 13: Decay scheme of ^{48}Ca [47].

To detect this decay event, we need to select a scintillation crystal with Ca component as the absorber of scintillating bolometer. There are four satisfying candidates, CaF_2(Eu), CaF_2, $CaWO_4$ and $CaMoO_4$ in table.3. In scintillating bolometer experiments, the dilution refrigerator's volume is limited, so we have to select a crystal that can contain Ca element as much as possible. CaF_2(Eu) and CaF_2 have about 4 mol Ca nuclei in a 5 cm cylinder crystal, while $CaWO_4$ and $CaMoO_4$ can only contain half of that. CaF_2(Eu) and CaF_2 can be purchased from company, but $CaWO_4$ and $CaMoO_4$ cannot at the moment. If we employ $CaWO_4$ or $CaMoO_4$, we have to grow those crystals by ourselves. Another thing that we should consider is the Debye temperature θ_D. The temperature increase of crystal absorber is proportional to θ_D^3, so we can observe a larger signal if we employ CaF_2(Eu) or CaF_2 as the absorber of our scintillating bolometer. From above reason, we plan to develop a scintillating bolometer using a CaF_2(Eu) or CaF_2. Another Ph.D student studied a CaF_2 scintillating bolometer, and I studied a CaF_2(Eu) scintillating bolometer. In this thesis, I will discuss about CaF_2(Eu) scintillating bolometer development.

Table 3: Comparison of different Ca scintillation crystals

target	CaF_2(Eu)/CaF_2	$CaWO_4$	$CaMoO_4$
content ratio (mol/cm^3)	4.07	2.03	2.03
available from market	Yes	No	No
Debye T (K)	513	250 [48]	395 [49]

4.2 Preliminary low temperature experiments using CaF_2(Eu) scintillator for rare event physics

Actually, the CaF_2(Eu) scintillating bolometer has a long history, but its low temperature properties are not understood in detail. This section will introduce the studies of CaF_2(Eu) scintillator at low temperature, which were carried out by several preliminary experiments from 1992.

4.2.1 First bolometer of CaF_2(Eu) in 1992

The first low temperature experiment using CaF_2(Eu) scintillator was carried out by Russian and Italian group to search neutrinoless double beta decay [50]. They used a 2.50 g CaF_2(Eu) crystals in the shape of cylinder with 10 mm diameter and 10 mm height. The CaF_2(Eu) crystals had different Eu doping densities from 0.01% to 0.07%, and were cooled down from 300 K to 20 mK to study thermal and scintillation performances, respectively. Thermal signal was measured with 0.01% Eu doping CaF_2(Eu) crystal and NTD-Ge thermistor. The energy resolution of thermal signal was 3.7% (FWHM), calculated with 1,500 keV double escape peak of ^{208}Tl's 2,615 keV gamma rays. Scintillation signal was detected by PIN silicon photodiode using 0.03% Eu doping CaF_2(Eu) crystal. The energy resolution was 10%, evaluated from ^{241}Am's 5.485 MeV alpha peak. In this experiment, two important informations were mentioned. Firstly, even though the thermal signal and the scintillation signal were detected by two different experiments, it showed that the simultaneous measurement of thermal and scintillation signal is possible for CaF_2(Eu) scintillator. Secondly, since Europium is paramagnetic, the doping level could increase the heat capacity of the CaF_2 absorber to deteriorate the energy resolution [51]. However, the authors asserted such doping levels of 0.01% don't affect the heat capacity of CaF_2(Eu) as a thermal detector.

4.2.2 Scintillation study at low temperature in 1995

After the possibility of simultaneous detection of heat and light was confirmed, people wanted to know how much is the light yield of CaF_2(Eu) scintillator at low temperature. The light yield of CaF_2(Eu) scintillator determines the discrimination power of critical alpha background events, especially, ^{238}U's 4270 keV alpha events. The light response of a CaF_2(Eu) scintillator as a function of the temperature down to 1 K is presented in [52] to evaluate the feasibility of applications of scintillating bolometer using CaF_2(Eu) scintillator to search for $0\nu\beta\beta$ decay. In the experiment, the CaF_2(Eu) crystal is 54 g, much larger than the one used in [50]. A windowless photodiode was used to detect the scintillation light and the scintillation yield almost didn't change from 300 K to 1 K (Fig.14). That means CaF_2(Eu) could also have a high light output at the temperature below 1 K. One can expect a high discrimination power to reduce the alpha background.

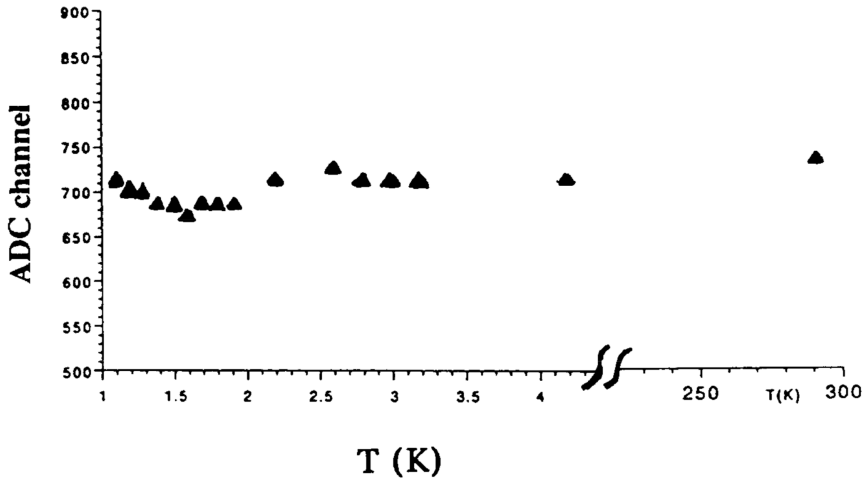

Figure 14: Temperature dependence of light yield of CaF_2(Eu) scintillator [52].

In Ref.[52], another thing should be emphasized here. The crystal used was produced by a Russian company with 0.01% Eu concentration, however, in which the ^{238}U and ^{232}Th contamination was less than 4 ppb. This means CaF_2(Eu) crystals with a low intrinsic radioactive contamination can be grown and the intrinsic ra-

dioactive contamination doesn't become a threat to the application of a CaF_2(Eu) scintillating bolometer to search for $0\nu\beta\beta$ decay.

4.2.3 First simultaneous detection of phonon and scintillation in 1997

The best result on energy resolution and discrimination power of alpha and beta/gamma was given by French group [53]. Since the purpose is to directly detect WIMPs (weakly interacting massive particles), an extremely small CaF_2(Eu) crystal of 300 mg was utilized to achieve low energy threshold. They used a NTD-Ge sensor to detect phonons from the CaF_2(Eu) crystal. The scintillation light detection is carried out by an infrared bolometer consisting of sapphire disk and NTD-Ge sensor (Fig.15).

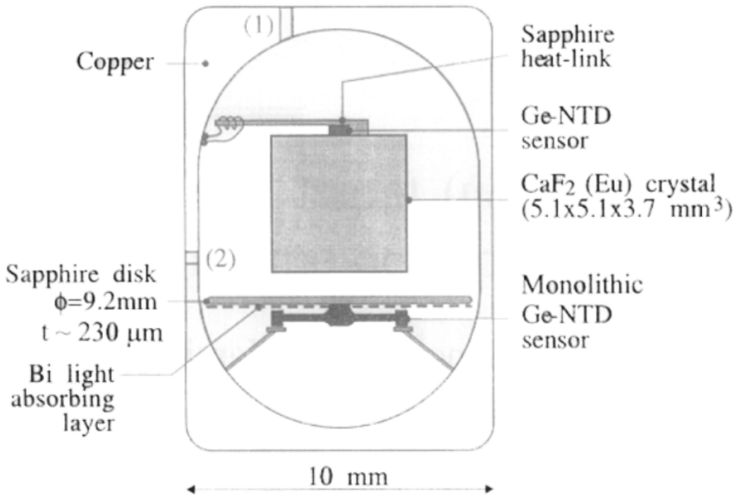

Figure 15: Experimental setup of a 0.3 g CaF_2(Eu) scintillating bolometer for WIMPs detection [53].

From two-dimensional plot of thermal and scintillation signals (Fig.16), gamma and alpha events were clearly grouped along two straight lines with a slope ratio of about 7.3, which implies a good discrimination power of beta/gamma and alpha background. However, the alpha events are from an external alpha source, not bulk events uniformly distributed in the crystal. The discrimination power was not evaluated at that time.

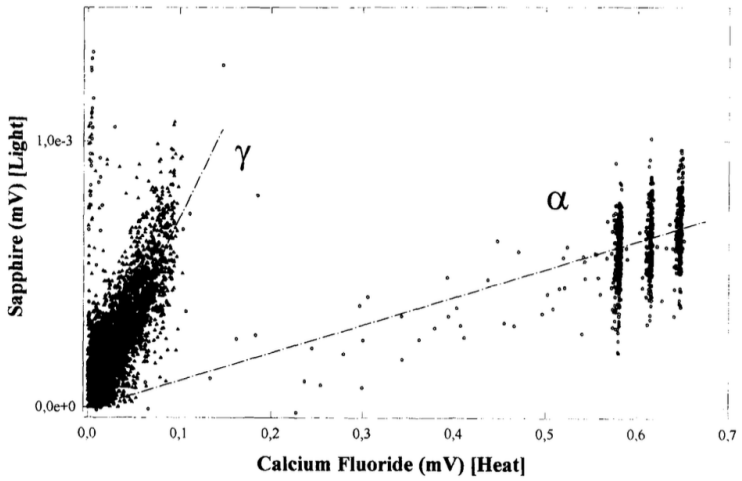

Figure 16: Simultaneous detection of heat and light signals by a 0.3 g CaF_2(Eu) scintillating bolometer [53].

The mass concentration of Europium in the CaF_2 crystal is 0.3%, quite higher than the preliminary experiments [42,44]. This level of doping might be too high to maintain good thermal properties of CaF_2(Eu) target, while the energy resolution of thermal signal is 22.5 keV (FWHM) on the ^{241}Am's 5485 keV line, equal to 0.41%, shown in Fig.17.

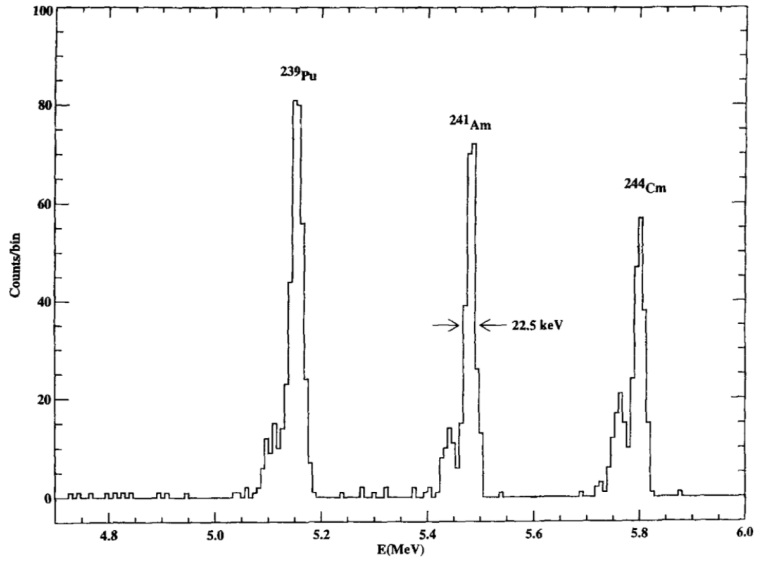

Figure 17: The spectrum of external alpha events [53].

In this experiment, the temperature could only be cooled down to 130 mK, because the heat capacity of Bismuth coating on the sapphire disk increases below 100 mK. If we can cool the crystal down to a few 10 mK, it may achieve a similar energy resolution with much more massive CaF_2(Eu) crystal. However, in this 20 years, there is no experiment to study a large volume CaF_2(Eu) scintillating bolometer. We still don't know how much energy resolution can be achieved, and if a large volume CaF_2(Eu) crystal is suitable as an absorber of scintillating bolometer for the $0\nu\beta\beta$ decay search.

4.3 Purpose of my study

From the above previous experiments, we have known the CaF_2(Eu) crystal also emits scintillation photons at low temperatures, so simultaneous detection of phonon and scintillation is possible. The light yield is unchanged from root temperature to 1 K, so a strong discrimination power can be expected. Using an external alpha source, a 0.3 g CaF_2(Eu) crystal achieved 0.42% (FWHM) energy resolution.

Now what we are interested in are as follows,

- how much is the energy resolution for a large volume CaF_2(Eu) scintillating bolometer?
- To reduce alpha background, how large is the discrimination power?
- Does europium doping really affect detection performance of CaF_2(Eu) scintillating bolometer?

The answers of these questions are significant to the development of measurement technology for $0\nu\beta\beta$ decay, because energy resolution is the only way to reduce $2\nu\beta\beta$ background. In Fig.18, we can see the importance of energy resolution. In the case of $< m_{\beta\beta} >= 5$ meV, the $2\nu\beta\beta$ background will submerge the $0\nu\beta\beta$ decay events in the case of 4.0% (FWHM) energy resolution. If we can achieve 0.5% (FWHM) resolution, the $2\nu\beta\beta$ background can be reduced to negligible level.

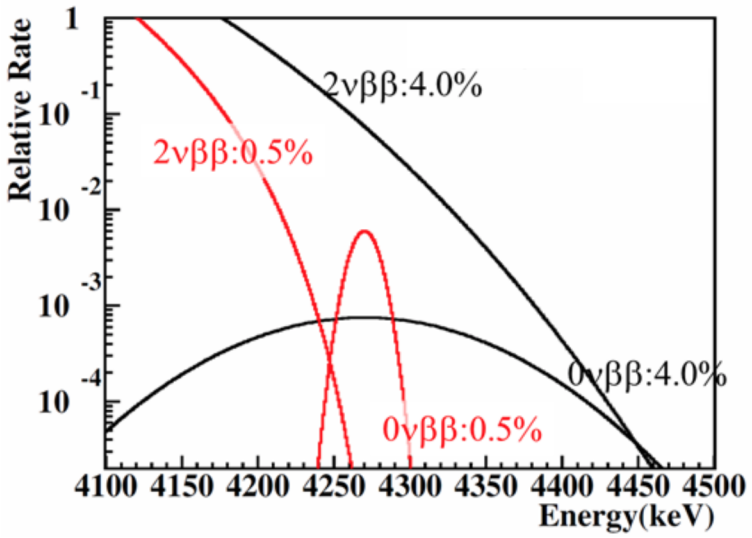

Figure 18: Importance of energy resolution for neutrinoless double beta search.

In the view point of development of low temperature technology, it's very interesting to understand if high doping density crystal can be used as an absorber for scintillating bolometer. Until now, the scintillating bolometer experiments only succeeded in several pure crystals for scintillating bolometer. If doping crystals, like CaF_2(Eu), are also suitable absorbers for scintillating bolometer, we can have many more crystal choices to study $0\nu\beta\beta$ decay. On the other hand, the scintillating bolometer technology can also be applied to other physics topics, like WIMPs detection and rare alpha decay search.

5 Development of scintillating bolometer with a large CaF_2(Eu) crystal

In this section, I will describe my development of scintillating bolometer using a large CaF_2(Eu) crystal. In this development, we cooperated with low temperature technology groups in Korea Research Institute of Standards and Science (KRISS) and Institute for Basic Science (IBS) of Republic of Korea and applied metallic magnetic calorimeter technology to the CaF_2 scintillating bolometer. The detector configuration will be described at first and then each developed element will be shown later on. In addition of description of the detector setup, I will show a mechanism diagram to discuss the physics phenomena caused in the detector system.

5.1 Detector configuration

At first, this R&D detector configuration is shown in Fig.19. A 312 g CaF_2(Eu) crystal in weight percent of 0.17% Eu is employed as a target. Heat signals from the crystal are read by a metallic magnetic calorimeter (MMC) that is thermally connected to a multi-layer phonon collector film evaporated on the surface of the crystal. A light detector composed of a 2 inch Ge wafer and an MMC sensor is placed just above the crystal. A silicon heater is attached to the crystal to generate periodic reference signals in the heat channel.

A Ag-Au phonon collector film was deposited on a 50 mm in diameter and 50 mm in height (50 mm Φ $\times$ 50 mm H) CaF_2(Eu) crystal. The Ag layer can reflect 99.7% of 425 nm scintillation light of the crystal and the gold layer prevents the silver's oxidation. An expanded PTFE reflector surrounded the crystal to increase the light collection efficiency. The detector was installed in a dilution refrigerator to cool down to 10-40 mK. The measurement was carried out in an above-ground laboratory.

The following subsections will introduce basic properties of our CaF_2(Eu) scintil-

lation crystal, structure and design of phonon collector, process of phonon detection by MMC and light detection of the light detector. Finally, we will show some pictures of the real detector setup.

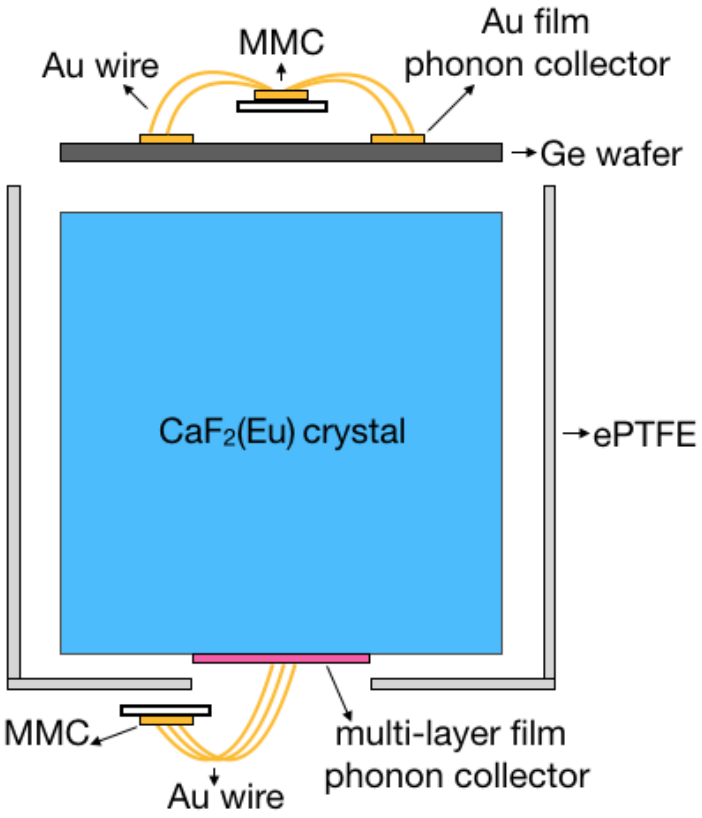

Figure 19: The schematics of phonon-scintillation detection using a CaF_2(Eu) crystal and MMC readouts.

5.2 Basic properties of CaF_2(Eu) crystal used in this experiment

The CaF_2(Eu) crystal used in this experiment is in the shape of cylinder with 50 mm height and 50 mm diameter, whose total mass is 312.18 g (Fig.20). Since the molar mass is 78.07 g/mol, there are 4 mol of calcium atoms in this crystal. Among them, there are 4.51×10^{21} ^{48}Ca isotope nuclei, calculated with natural isotopic abundance of ^{48}Ca, 0.187%. The mass density of europium doping is 0.17%. Since the molar

mass of europium is 152 g/mol and the one of CaF_2 is 78 g/mol, the mole density of europium is about 0.09% and there are 2.0×10^{20} europium nuclei in the CaF_2(Eu) crystal.

Europium has two states of Eu^{2+} and Eu^{3+}. In Eu-doped CaF_2, paramagnetic Eu ions are in the form of Eu^{2+} and localize instead of Ca^{2+} in the CaF_2 crystal. When growing CaF_2(Eu) crystals, one use a reduction treatment, which is known as a thermal-carbon reducing atmosphere treatment [54] , to transform all Eu^{3+} to Eu^{2+}. The abundance ratio of Eu^{3+} and Eu^{2+} can be confirmed in the emission spectrum of CaF_2(Eu), because the emission peak of Eu^{2+} is 435 nm while the one of Eu^{3+} is 613 nm. After providing weak reducing atmosphere for forming Eu^{2+} in the treatment, no emission peak corresponding to Eu^{3+} can be found [55].

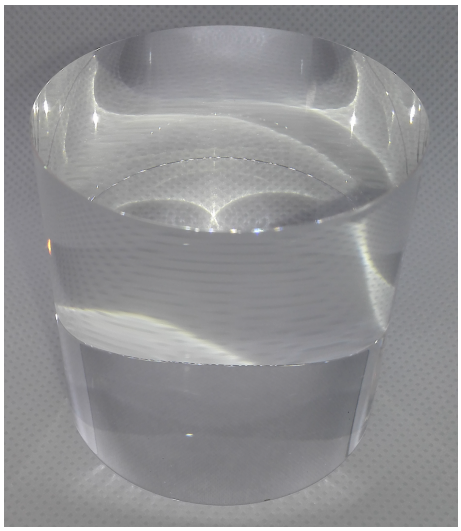

Figure 20: CaF_2(Eu) crystal used in this experiment.

The basic properties of CaF_2(Eu) scintillator can be found in the website of Saint-Gobain company. The CaF_2(Eu) crystal is not hygroscopic, so it doesn't need a special isolation treatment like NaI crystals. The crystal is also hard enough to be fixed firmly in the detector module. If the crystal is not hard enough or cleavable, cracks could occur when assembling the detector module. Cracks in crystal can seriously prevent phonon propagation and degrade energy resolution, which was

reported in Ref.[56].

Table 4: Basic properties of CaF_2(Eu) crystal at 300K

Properties	Value
Density [g/cm^3]	3.18
Melting point [K]	1691
Cleavage plane	<111>
Hardness (Mho)	4
Hygroscopic	no
Wavelength of emission max [nm]	435
Lower wavelength cutoff [nm]	395
Refractive index at emission max of 435 nm	1.44
Primary decay time [ns]	940
Light yield [photons/MeV$_\gamma$]	23500
Photoelectron yield [% of NaI(Tl)] (for γ-rays)	50

The scintillation light of CaF_2(Eu) has emission peak at 435 nm with a narrow width from 395 nm to 520 nm, shown in Fig.21. The light yield is 23500 photons/MeV, which is about half of NaI scintillator. There is no temperature dependence in the light yield for CaF_2(Eu) from 300 K to 1 K, so we can also expect the same light yield at mK region. This high light yield can provide a good particle discrimination power to reduce alpha background. The primary decay time of CaF_2(Eu) is as short as 1 us and also doesn't have strong temperature dependence from 300 K to 8 K [57].

The refractive index of CaF_2(Eu) crystal is 1.44 at 435 nm, so total reflection angle is very small, 45 degree. Scintillation light emitted at close to the surface is easier to be reflected on the surface, while that emitted near the center has a high probability to escape from the crystal. When the scintillation photons propagate through the crystal, some of them are absorbed by the crystal itself due to atten-

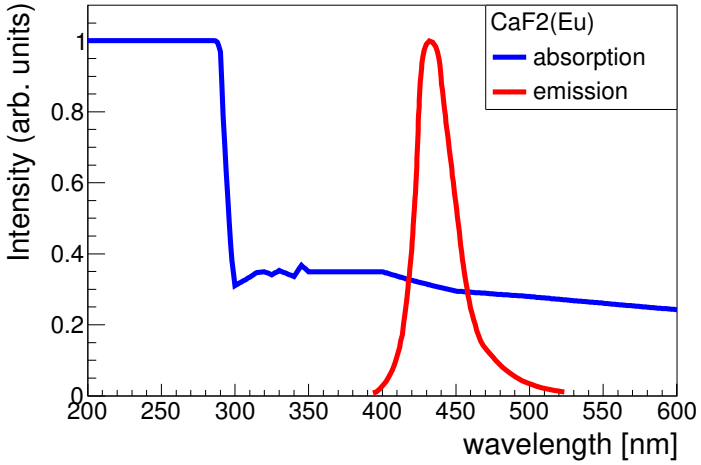

Figure 21: Emission and absorption spectra of CaF_2(Eu) scintillator.

uation. The attenuation length of CaF_2(Eu) is 6.5 cm for 435 nm emission peak and has wavelength dependence. The data of attenuation length is obtained from a collaborator. In the communication with the collaborator, we knew the attenuation length depends on the Eu doping density [58]. In general case, the commercial crystal has 3.6 cm attenuation length. However, our crystal's Eu density seems a little lower than the commercial one, so a longer attenuation length was considered. To be consistent with our data result, we found 6.5 cm is the most possible. Using that value, I calculated the absorption for the different wavelength as

$$I_{abs} = 1 - \frac{I}{I_0} = 1 - e^{-\frac{l}{\lambda}}, \tag{36}$$

where I_{abs} is light absorption probability, I is the transmission of scintillation light in a length of l, I_0 is total amount of scintillation light and λ is the attenuation length from the measured data. Here, the length l is used as 2.5 cm, a half of the length of diameter and height of crystal used in this study. The absorption at each wavelength is shown as the blue line in Fig.21. From this result, we can see there are about 30% of photons will be absorbed by crystal itself after propagating 2.5 cm.

The mechanism after radiation deposits energy in the crystal is shown in Fig.22. When radiation deposits energy in the crystal, most of energy generates high energy phonons (athermal phonons). The high energy phonons thermalize the whole crystal and down-convert to equilibrium phonons (thermal phonons). The energy of phonons in equilibrium condition has a Bose-Einstein distribution and the mean energy is product of Boltzmann constant k_B and temperature T, k_BT. In the Debye model, the minimum energy of phonon could be infinitely close to 0, however, the maximum energy cannot exceed k_BT_Θ, where T_Θ is the Debye temperature of the crystal. At 10 mK, the mean energy of phonons is 1 μeV with a maximum of 50 meV.

At the same time, scintillation photons are also emitted. The total energy of scintillation photons can be calculated as the product of photon average energy of 2.8 eV with light yield of 23500 photons/MeV. A beta ray with energy of 4.27 MeV generates photons equivalent to 281 keV, which is in a percentage of 6.5%. For alpha events, the energy of photons should be less because of quenching factor. In the case of beta rays, in addition to scintillation light, Cherenkov radiation is also emitted in the crystal. Compared with scintillation light, photons from Cherenkov radiation are much fewer, but we have to confirm if they cause problems in our detector system.

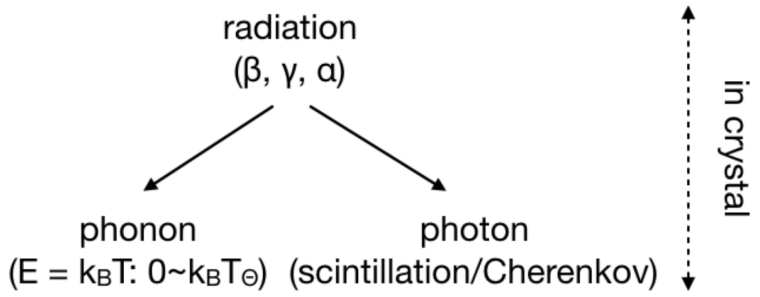

Figure 22: Mechanism of events happening in the crystal.

5.3 Phonon collector

The CaF_2(Eu) was fixed with several teflon supports in the detector module (Fig.23). The teflon worked as a weak thermal link connected to the heat bath. In the low temperature detector with MMC, we need to transport phonons to the MMC as much as possible. We employed a metal film phonon collector with a much higher thermal conductivity than the teflon. For example, the thermal conductivity of teflon is $3.0 \times 10^{-5}\,\mathrm{Wm^{-1}K^{-1}}$, while silver is $50\,\mathrm{Wm^{-1}K^{-1}}$. From this 6 orders of magnitude difference of thermal conductivity, we can think most of phonons are collected into the metal film phonon collector.

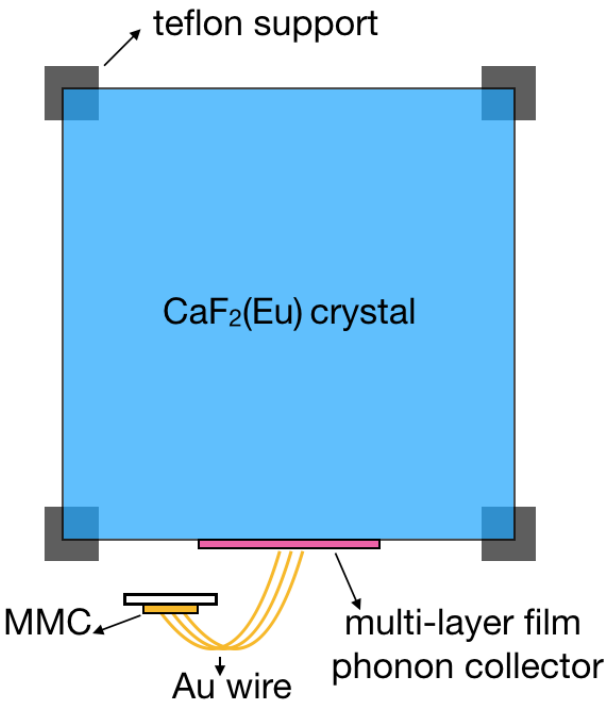

Figure 23: A multi-layer film phonon collector is used to collect phonons generated in the crystal.

The phonon collector is designed as a multi-layer metal film evaporated on the bottom of the crystal. After phonons thermalized the whole crystal, they are absorbed by the low temperature metal film. 24 gold wires are bonded on the center of metal film and are bonded to the MMC. The heat flows from the metal film to

the MMC through the gold wirings.

The physical mechanism happened in the crystal and at the boundary of crystal and metal film is shown in Fig.24. Thermal transport in dielectric crystal is usually considered to be governed by the three-phonon scattering process. When high energy phonons are generated by radiation, the phonons decay into two lower energy phonons. In this collision process, the energy and quasi-momentum are conserved as

$$h\omega_1 = h\omega_2 + h\omega_3 \tag{37}$$

and

$$h\boldsymbol{q}_1 = h\boldsymbol{q}_2 + h\boldsymbol{q}_3, \tag{38}$$

where ω_i is i_{th} phonon's frequency and $\boldsymbol{q}_i$ is i_{th} phonon's wave vector. By repeating this process, the generated phonons thermalize the whole crystal and are finally absorbed by the metal film.

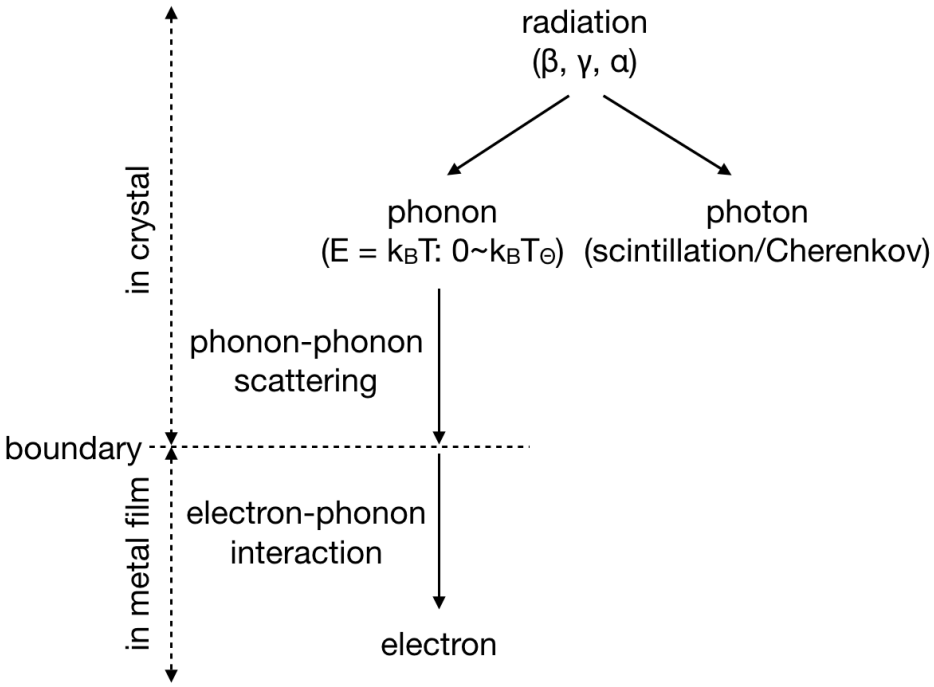

Figure 24: Mechanism of phonon propagation in the crystal and at the boundary of crystal and metal film.

At the boundary of metal film, heat from the crystal is transferred to the metal film through phonon-electron interaction (Fig.24). In metal, electrons are main heat carriers, not phonons. The phonon-electron interaction can be considered as a free-electron gas scattered by a phonon wave. The free-electrons are in the Fermi sphere with a electronic wave vector $\boldsymbol{k}$. When phonon with a wave vector $\boldsymbol{q}$ scatters the free electron, the electronic wave vector changes to $\boldsymbol{k'} = \boldsymbol{k} + \boldsymbol{q}$. Repeating this process, the thermal flow goes into the metal film and is carried by electrons. The electrons transport heat at the speed of sound. The speed of sound in metal is in an order of 10^3 m/s, for example, the silver has 2680 m/s at room temperature. At lower temperature, the speed becomes slower, but still remains in the order of 10^3 m/s.

5.4 Phonon collector design

For this experiment, I did lots of ingenuity to design the metal film phonon collector. As shown in Fig.25, the metal film was evaporated on the CaF_2(Eu) crystal and consists of 5 nm titanium layer, 150 nm silver layer, 50 nm gold layer and 200 nm gold pattern. The selection of silver as the main part of phonon collector was because silver layer can reflect the scintillation light of CaF_2(Eu) well. The detail of the effect of scintillation absorption will be explained in the section of 5.7.2. During the experimental preparation, silver film could be oxidized in the air. To avoid the oxidation, we evaporated 50 nm gold film onto the silver film.

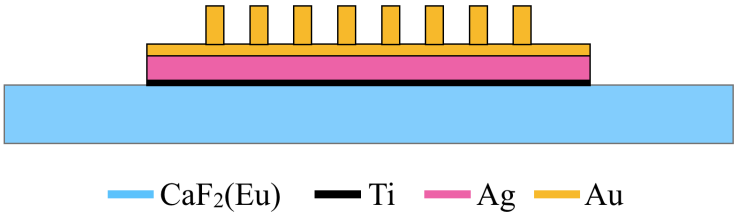

Figure 25: The structure of multi-layer metal film phonon collector.

The titanium layer works as an adhesive to improve adhesion between CaF_2(Eu) and silver layer. Since silver doesn't directly adhere to glass, it doesn't adhere to CaF_2(Eu) crystal either. We carried out an evaporation test using a CaF_2 test piece and verified this fact. To check the adhesion power, we pasted a Kapton tape with an adhesion power of 4 N/10 mm onto the evaporated silver film and peeled the tape off vertically from the crystal. The result showed most of silver film was peeled off as we predicted. However, from this test we found that silver can attach to the crystal strongly if the crystal's surface is unpolished and rough. However, the rough surface can affect the electrical conductance of metal film absorber, because the roughness is comparable to the thickness of metal film. Therefore, an intermediate layer is necessary for silver evaporation on CaF_2(Eu) crystal.

The intermediate layer candidates for silver evaporation are SiO_2, Al_2O_3, Ti and

Cr. SiO_2 or Al_2O_3 of 50 nm thickness is commonly used for silver evaporation on glass for some optical applications. Ti and Cr are well known as a good intermediate layer for crystals. Ti is also used as an adhesive for a $CaMoO_4$ crystal in the previous experiment, so we think it also can adhere well to CaF_2(Eu) crystal. In a journal on nano-particle physics, we found Ti was used to adhere silver to glass [59]. Therefore, Ti is possible to adhere both CaF_2(Eu) crystal and silver. In this experiment, we employed Ti as the adhesive for our CaF_2(Eu) crystal. The Ti layer with a thickness of few nm can be treated as a transparent material [60].

The gold pattern shown in Fig.26 has 12 main branches spreading from the center of metal film with each main branch having two pairs of small branches at an angle of 20° and 30° to it. The width of the branches is 0.6 mm, which is the minimum width where we can control the evaporation thickness precisely. In the case of narrower width, outgassing from surrounding materials could disturb the gold particle's straightness leading to a thinner gold pattern than our target thickness.

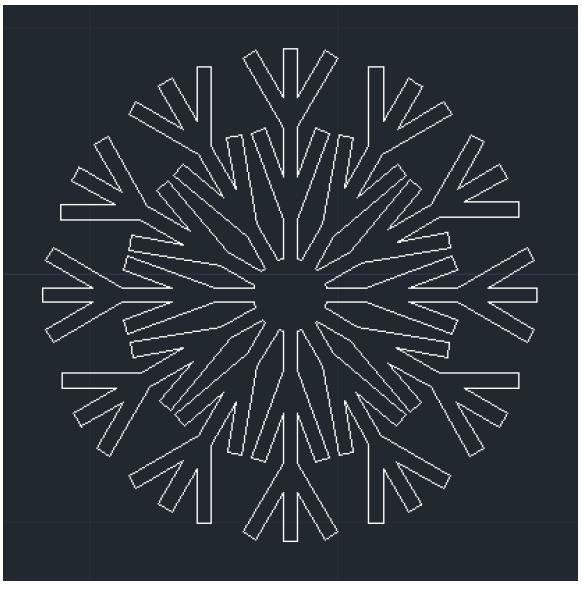

Figure 26: Design of gold pattern.

The gold pattern can increase the concentrating efficiency of phonons to the center, which results in a decrease of rise-time and an increase of signal pulse height.

In the metal film, most of heat is carried by electrons. The electrons move in random directions in the metal film, like the left picture in Fig.27. The gold wires between the MMC and the metal film are only bonded in the center of metal film, because bonding length of the wire bonding machine is limited. Therefore, we need a radial pattern to concentrate the thermal flux of electrons to the center as faster as possible. The radial pattern can be considered as a groove that has one side is closed and the other side is opened at the center, so the thermal flow has to concentrate on the center. This pattern can increase the efficiency of phonon collection, which results in a signal pulse with a shorter rise time. The shorter rise time also means a higher amplitude signal in our low temperature measurement, so a higher amplitude signal is less susceptible to noise and provides a better resolution.

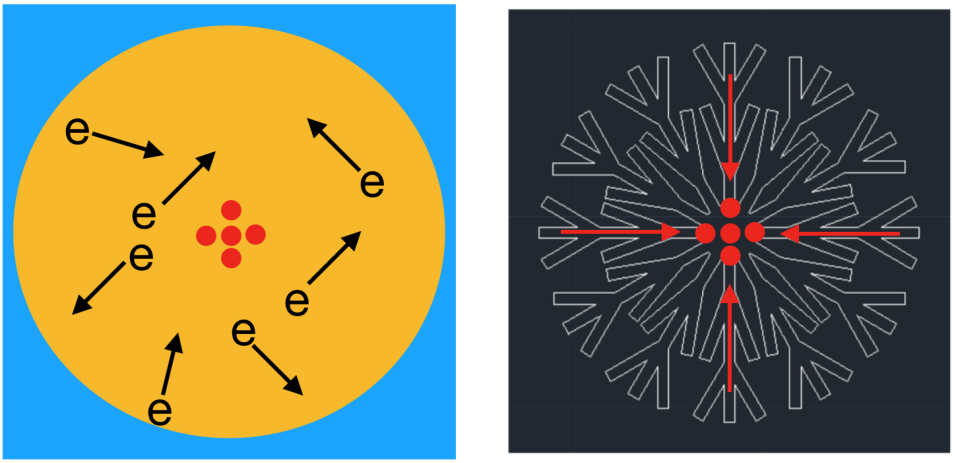

Figure 27: Effect of gold pattern. The red points represent the gold wires' bonding positions.

5.5 Multi-layer metal film production

The production of multi-layer metal film consists of three processes. The first is surface cleaning of CaF_2(Eu) crystal, which is a preparation work for the following evaporation process. The second is evaporation process of multi-layer metal film in the factory of our technical cooperation company, Etsumi Ltd. The third is an adhesion test to check if the metal film can work well as a phonon absorber.

5.5.1 Surface cleaning method

Crystal surface cleaning is a significant part in the evaporation process. Even if only slight organic layer remains on the surface, it could deteriorate adhesion of metal film and cause a failure of costly evaporation test. In this experiment, we cleaned the CaF_2(Eu) crystal as below.

1. Acetone washing: To remove organic layer on the crystal's surface, we used acetone to clean it at first. Since the crystal is strong and shock-resistant, 10 min ultrasonic cleaning in 100 kHz frequency was carried out. This step is to clean the mineral oil and other greases.

2. Isopropyl alcohol (IPA) washing: After acetone washing, we inserted the crystal into IPA and followed the ultrasonic cleaning step as before. This step is to remove the remaining acetone on the crystal and was carried out twice.

3. Distilled water washing: Since CaF_2(Eu) is not hygroscopic, we finally cleaned the crystal with distilled water after IPA washing. While the purity of IPA is higher than 99%, there is still a little mineral oil remaining in the IPA production process. To remove it completely, we carried distilled water washing three times.

After the cleaning process, I blew away the remaining water on the crystal surface with a N_2 gas gun and packaged the crystal into a plastic bag, which is then sent to the company for metal film evaporation.

5.5.2 Evaporation process

To create the multi-layer metal film shown in Fig.25, we have to find an evaporation machine that can satisfy several requirements. The first requirement is a machine that can hold a large target. Most of companies can evaporate metal layers onto a thin silicon wafer, not a target with 5 cm thickness. The second requirement is a machine with more than 3 source target spots. Since silver is very easy to be oxidized in the air, we have to evaporate Ti layer, silver layer and gold layer in a single process. Evaporation machine with less than 3 source target spots has to be opened once for the supplement. During the supplement, silver has a risk to be oxidized and make the evaporation process fail. The final requirement is a low temperature evaporation process. The melting point of silver and gold is about 1000 degree, the high temperature heat radiation could heat the crystal and cause cracks in the crystal. The cracks in the crystal will obstruct the propagation of phonon and make resolution worse. To avoid this situation, we need to evaporate metal film onto the crystal at a lower temperature. There are two ways to achieve a lower temperature condition, one is to cool down the crystal while evaporating; the other one is to increase the distance between source target and the crystal. The heat radiation decreases in proportion to solid angle. When the crystal is fixed far from the source target, the solid angle becomes small and the heat transfer from radiation to the crystal becomes less.

Our evaporation process was carried out in the Etsumi company, which is the biggest sun glass company in Japan. The evaporation machine in the Etsumi company can satisfy all of our requirements. It has a 2 m height with 1.5 m diameter volume as shown in Fig.28. The distance from source target spots to the crystal hold is about 1 m, keeping the crystal's temperature at 60 degree while evaporating gold layer.

There are more than 10 evaporation target spots on the bottom (Fig.29). In the evaporation process, we used one spot for titanium, one spot for silver and two

Figure 28: Evaporation machine of Etsumi company. Release of this photo has been permitted by the employee in charge of the deposition work.

spots for gold. Electron beam was emitted from the hole on the right side of source target spots and was bended by magnetic field until it collides the source target in the spot. During the collision, the metal particles obtained kinetic energy from electrons and moved up to the crystal side.

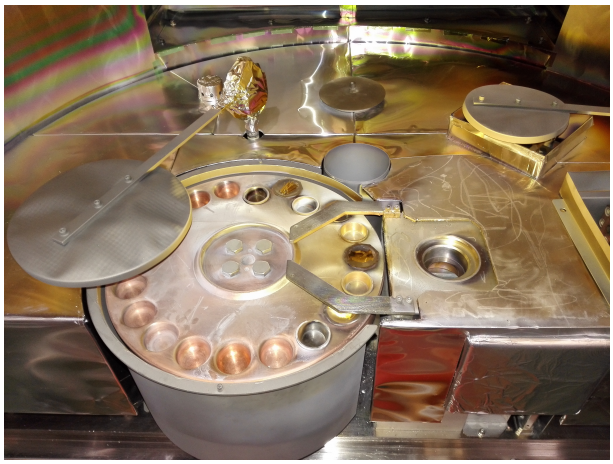

Figure 29: Evaporation target spots. Release of this photo has been permitted by the employee in charge of the deposition work.

The crystal was placed in a teflon cup shown in Fig.30 and was fixed on the top of evaporation machine. In the first step of evaporation process, titanium layer, silver layer and gold layer were evaporated in the shape of a circle, respectively. The thickness of each layer was controlled through evaporation time. In this first step, we evaporated 5 nm titanium layer, 150 nm silver layer and 50 nm gold layer. From the experience of company's employees, the error of thickness was about 0.5 nm for each layer. In the second step, we opened the machine and installed mask shown in Fig.31 into the teflon cup. After that, we evaporated 200 nm gold pattern onto the gold layer.

5.5.3 Evaporation results and adhesion test

Fig.32 and Fig.33 show the evaporation results of multi-layer metal film phonon collector. From the outside, we can see the gold face; from inside, we can see the silver face. The gold pattern is only 200 nm and is difficult to be identified, unless

Figure 30: Crystal holder for the evaporation process.

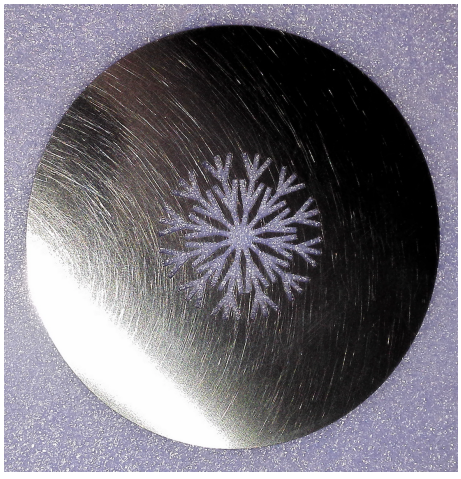

Figure 31: Mask for the second evaporation process.

view from a special direction of illumination. The silver face has high reflectivity for the visible light, we can see the image of my smartphone's camera.

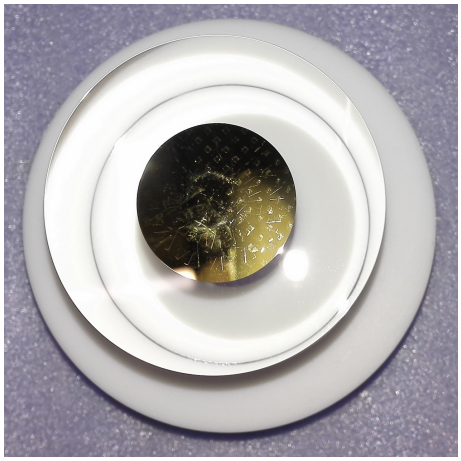

Figure 32: The gold face of multi-layer metal film.

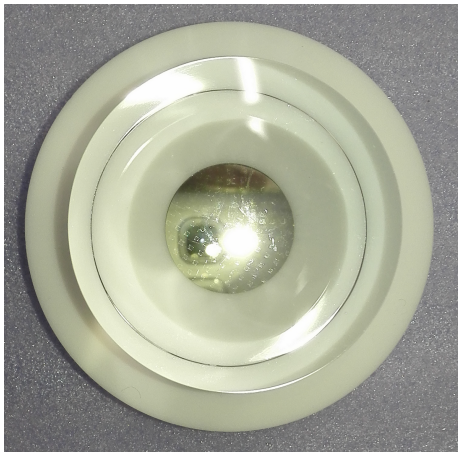

Figure 33: The silver face of multi-layer metal film

For the phonon-electron interaction at the boundary of crystal and silver layer, the metal film should be in close contact with the surface of crystal. We carried out an adhesion test to check if the contact is strong enough. An empirical method is used for the adhesion test. We pasted a Kapton tape with an adhesion power of 4 N/10 mm onto the evaporated metal film and peeled the tape off vertically from the crystal. As a result, no metal film was peeled off, therefore we judged that the multi-layer metal film phonon collector was completed.

5.6 Temperature increase measurement

After the metal film phonon collector absorbed phonons from the crystal, the phonons propagate towards the metallic magnetic calorimeter (MMC) through the gold wires (Fig.34). The temperature measurement of MMC can be explained as

$$\delta E \rightarrow \delta T \rightarrow \delta M \rightarrow \delta \Phi, \tag{39}$$

where δE is deposited energy from radiation, δT is MMC's temperature change induced by the δE, δM is MMC's magnetization change and $\delta \Phi$ is a magnetic flux change in a dc-SQUID circuit.

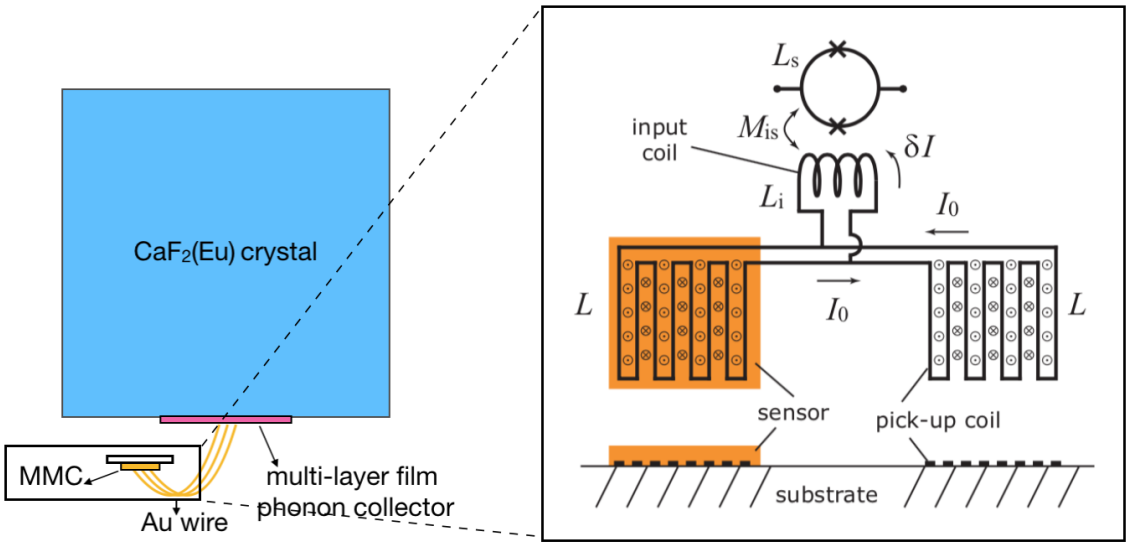

Figure 34: A schematic diagram of MMC.

The MMC is made of paramagnetic material Au:Er on a meander coil. The meander coil is evaporated on a silicon chip, which is attached to a copper plate by varnish. A constant electric current flows in the meander coil, so a magnetic field is generated in the space between the coil. There is a layer of paramagnetic material Au:Er on the meander coil. Under the magnetic field, spins in the paramagnetic material are in the same direction along the magnetic field. When the phonons from

the crystal transfer into the MMC, the temperature change induce a magnetization change of the paramagnetic material, then the electric current in the meander coil is also changed. Since the meander coil is connected to an input-coil of dc-SQUID, the current change in the meander coil causes magnetic flux fluctuation in the input-coil of dc-SQUID. Finally, the dc-SQUID changes the magnetic flux fluctuation to a voltage pulse, which is read out as signals.

5.7 Three types of photon propagations

The scintillation light emitted by $CaF_2(Eu)$ crystal has three physical processes, shown in Fig.35. The first one is self-absorption by crystal. The attenuation length for 435 nm scintillation light is 6.5 cm, so most of scintillation is absorbed by crystal as heat.

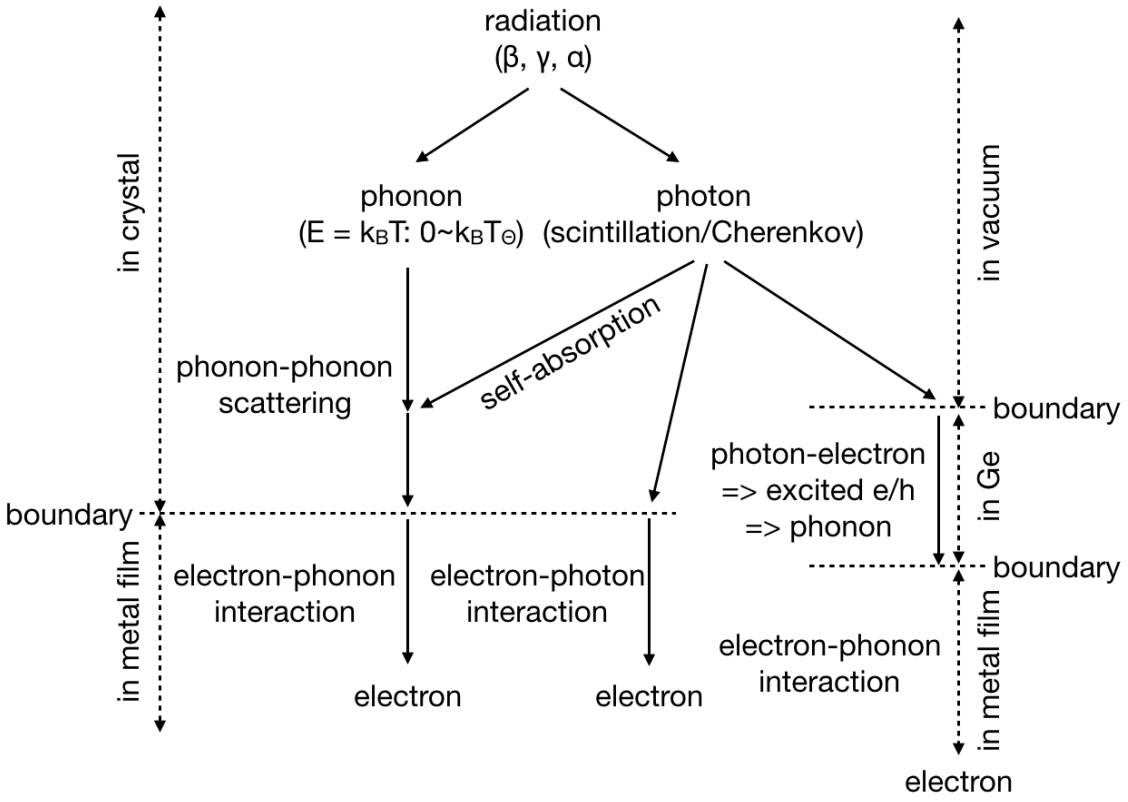

Figure 35: Three types of photon propagations.

A part of scintillation light could be absorbed by metal film, because metal easily absorbs UV light. However, the metal film is used as phonon collector, which means we want it to absorb phonon, not photon. Therefore, we have to choose a suitable metal that reflects scintillation light well. As the probability of scintillation absorption is not 0, we should consider this case and evaluate its effect by simulation.

There is a light detector placed on the top of the crystal. Some scintillation light is absorbed by the germanium wafer, which is the absorber of light detector, as light

signal readout. On the surface of Ge wafer, scintillation light creates an excited state of electron-hole pair through photon-electron interaction. The Ge semiconductor has two different band gaps, one is optical band gap, whose band gap energy is 0.7 eV; the other one is electrical band gap, whose band gap is about 3 eV. The optical band gap means only photons with energy higher than this band energy can be absorbed by the Ge semiconductor, while the electrical band gap means the energy needed to separate electron and hole electrically. In the case of CaF_2(Eu) scintillating bolometer, the scintillation photon has energy of 2.8 eV. The energy is higher than the optical band gap, so scintillation photons can be absorbed by the Ge wafer. The excited electron-hole pair drops down to ground state immediately and generates high energy phonons. By phonon-phonon scattering, the high energy phonons down-convert to equilibrium phonons and thermalizes the whole Ge wafer. The temperature rise of Ge wafer absorber is also measured by MMC with the same mechanism. There are 3 gold film evaporated on the Ge wafer to collect phonons. At the boundary of Ge wafer and gold films, phonon-electron interaction occurs and heat is transferred from phonons in the Ge wafer to the electrons in the gold films. Finally, the electrons carries heat to MMC through gold wires.

5.7.1 Self-absorption

Photon simulation can provide information of position dependence of self-absorption and also can check if the silver film reflect the scintillation light well to avoid metal film absorbing it.

The simulation model is set as same as the actual detector configuration, shown in the Fig.36. A Ge wafer of 2 inch diameter and 200 μm thickness is placed on the top of CaF_2(Eu) crystal. A Au or Ag film with 200 nm thickness and 10 mm diameter is attached on the bottom of the crystal. A reflector is set around cylindrical surface and on the bottom of crystal. The distance between the reflector and the crystal is same as the real detector. There is a gap between the Ge wafer and the reflector.

Scintillation light can escape from the gap.

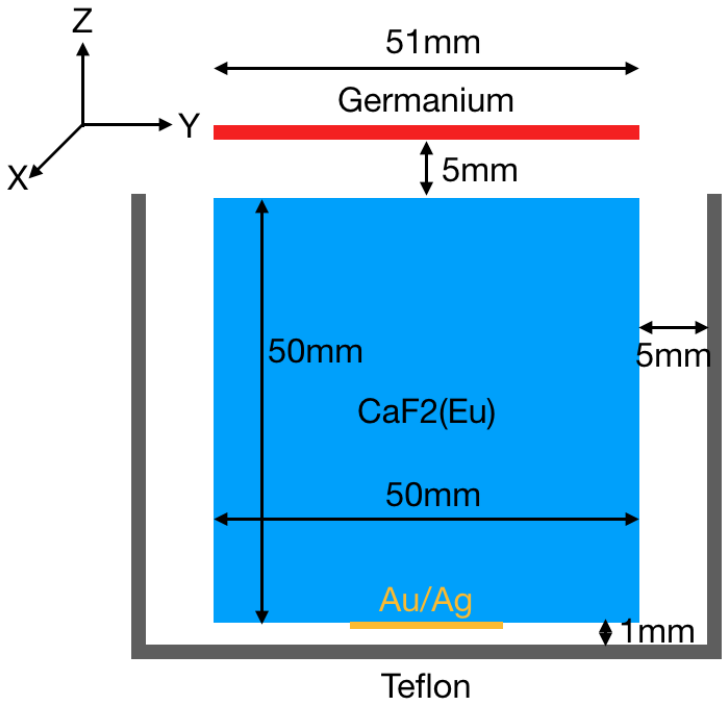

Figure 36: Scheme of simulation model.

Optical parameters used in the simulation include refractive index of CaF_2, real and imaginary refractive index of germanium, real and imaginary refractive index of gold or silver. The PTFE reflector is assumed to have 90% reflectivity with an angle dependence, which is included in the Geant4 package. The data of absorption length of CaF_2(Eu) crystal is 6.5 cm for 435 nm wavelength.

Initial photons generated in the simulation have several conditions. The first one is the photon energy. Depending $E = hc/\lambda$, the photon has a energy spectrum with a peak at 2.8 eV, which is equal to 435 nm emission peak of CaF_2(Eu) scintillator. The second one is photon's initial position. Since radiation deposits energy anywhere in the crystal, the photon's initial position is random and uniform in the crystal. The third one is photon's initial direction. When radiation deposits energy in the CaF_2(Eu) scintillator, many photons are generated and emitted in the random directions. As same as this fact, the scintillation photons are generated and

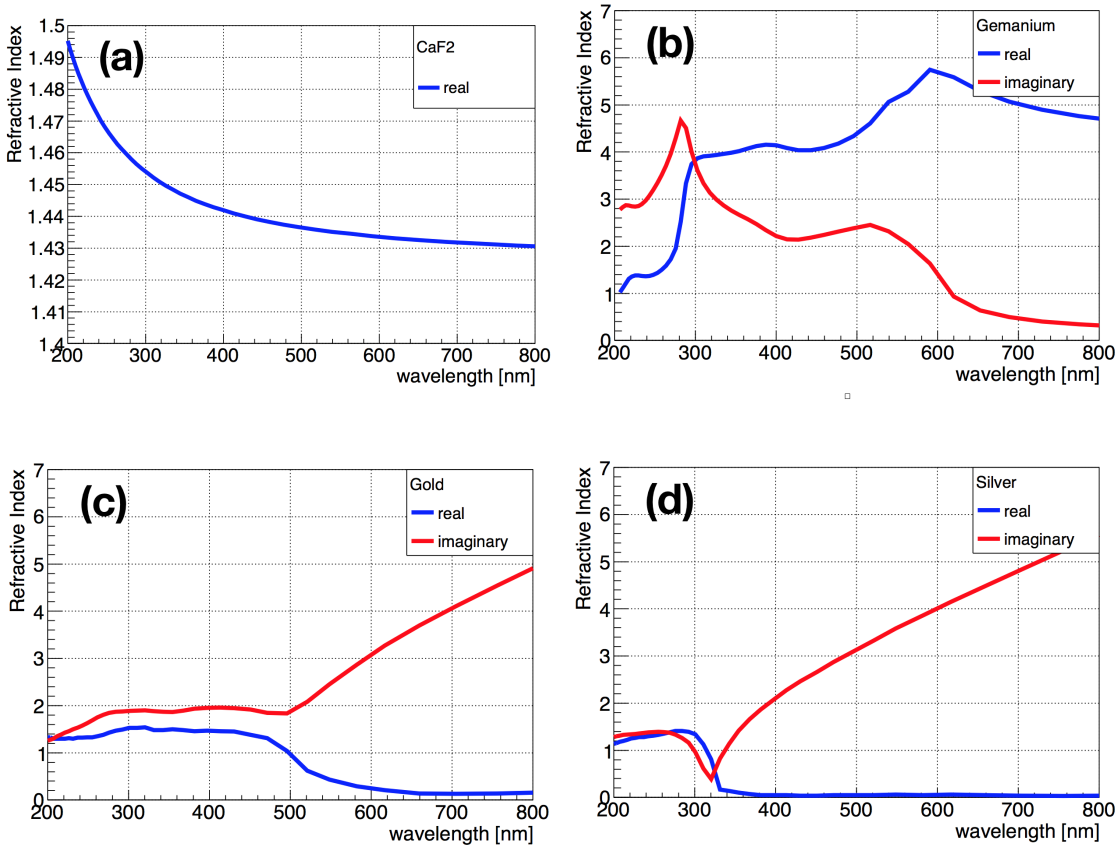

Figure 37: Optical parameters of the components in the simulation model. (a) real refractive index of CaF_2 crystal [61]; (b) real and imaginary refractive index of germanium [62]; (c) real and imaginary refractive index of gold [63]; (d) real and imaginary refractive index of silver [63].

emitted isotropically.

When photons propagate in the crystal, most of photons will be absorbed by the crystal itself because of the crystal's short absorption length. Fig.38 shows the initial photon positions that are finally absorbed by the crystal. Since the crystal is a cylinder shape with the volume element $\mathrm{dV} = \mathrm{r}\,\mathrm{dr}\,\mathrm{d}\theta\,\mathrm{dz}$, we use R^2 as horizontal axis and Z as vertial axis. From Fig.38, we can see approximate 81% photons are absorbed by the CaF_2(Eu) itself in this simulated condition and there is position dependence. In the top of the crystal, scintillation photons have a higher probability to be detected by the light detector. However, in the bottom of the crystal, photons that escaped from the crystal are reflected back by ePTFE reflector and came into

the crystal again. This process will increase the propagation length in the crystal, so the probability of self-absorption becomes higher. At the up-right corner, many photons can escape from the gap between the Ge wafer and the reflector, so the self-absorption probability is low.

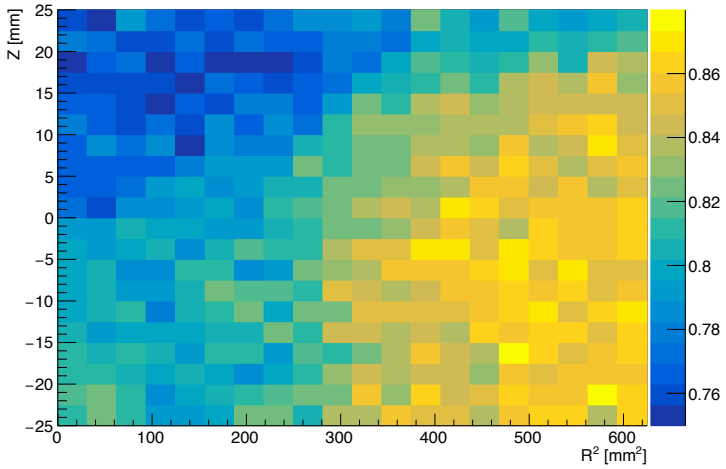

Figure 38: Position dependence of scintillation photon absorption by the crystal itself. The color in this figure shows the absorptance, which is represented by the ratio of absorbed photons by crystal to generated photons at that position.

The scintillation photons were absorbed and transformed to heat and were measured by the metal film phonon collector finally. The position dependence of self-absorption could induce to degrade the heat signal's resolution slightly. The total energy of scintillation photons are $23500\,\text{photons/MeV} \times 2.8\,\text{eV/photon} = 66\,\text{keV/MeV}$, which means 1 MeV beta ray should emit 66 keV photons totally. The deviation of position dependence in Fig.38 is 2%, so the contribution of self-absorption to heat signal's resolution should be $66\,\text{keV/MeV} \times 2\% = 1.3\,\text{keV/MeV}$. Therefore, the self-absorption of CaF_2(Eu) crystal only gives 0.13% deviation to the heat signal's resolution.

5.7.2 Photon absorption by metal film

In general, ultraviolet (UV) scintillation light is easy to be absorbed by metal. However, the metal film phonon collector is used to detect phonons, not photons. When metal film absorbs photons by photon-electron interaction, a fast component with a shorter rise-time and a shorter decay-time will be added to the phonon signal, like Fig.39. In low temperature measurement, the maximum of signal pulse is used as the parameter to evaluate event's energy, so the mixture of photon component will degrade energy resolution seriously. To avoid this case occurring, we have to develop a metal film phonon collector with both high thermal conductivity and high optical reflectivity for the CaF_2(Eu) scintillator.

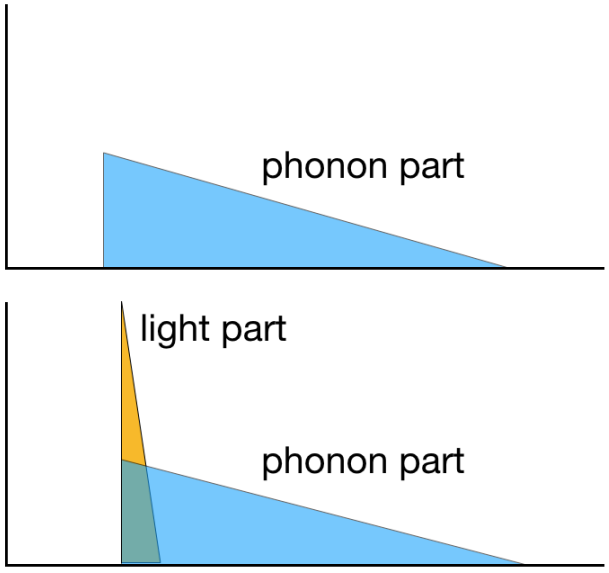

Figure 39: Effect of phonon absorption by metal film.

Metals with high thermal conductivity are gold, silver and copper. These metals can be refined to high purity level. Since metal film is contacted to the crystal, the high purity metal can contribute less background to our detector. At the same time, the high purity gold, silver or copper can be purchased from companies with reasonable prices. For example, 20 g silver only costs 500 dollars and 20 g gold costs 2000 dollars.

Compared to thermal conductivity, it is much difficult to select a metal with high reflectivity for UV light. At room temperature, aluminum is a good candidate with high reflectivity for UV scintillation. However, aluminum becomes superconducting material below 1.2 K and will absorb photons to break coopper pair of electrons. In Fig.40, we can see many elements will be superconducting at low temperature. The common non-surperconducting metals with high thermal conductivities include Cu, Ag, Au, Pd and Pt. The thermal conductivities of these metals are list in Table.5. The table shows silver, gold and copper are the candidates from the view points of thermal conductivity.

Table 5: Thermal conductivities of metals at 300K [65].

Metal	Thermal conductivity [$Wm^{-1}K^{-1}$]
Silver (Ag)	428
Copper (Cu)	403
Gold (Ag)	319
Platinum (Pt)	72
Palladium (Pd)	72

The reflectivity of each metal candidate should also be considered. The reflectivity of metal can be calculated by Fresnel equations with medium's refractive index information. Dielectric crystals have a real number refractive index n_0, while metals have a complex number refractive index $\overline{n}_1 = n_1 - ik_1$. The real component n_1 is the parameter in related to reflectivity and the imaginary component k_1 is the parameter in related to absorption. In the case of photons incident on a metal ($\overline{n}_1$) in a dielectric medium (n_0), with incident angle of 0 degree, the reflectivity R is written as

$$R = \frac{(n_1 - n_0)^2 + k_1^2}{(n_1 + n_0)^2 + k_1^2}. \tag{40}$$

Figure 40: Superconducting elements. This graph is taken from "Superconductivity in the metallic elements at high pressures" [64].

The absorption A is

$$A = 1 - R. \tag{41}$$

In the case of other incident angle θ_i, we have to consider about $s-$polarization and $p-$polarization. $s-$polarization has electric field parallel to the surface of the crystal and $p-$polarization has magnetic field parallel to the surface. The reflection coefficients for both cases are shown as below.

$$r_s = \frac{n_0 cos\theta_i - \sqrt{(n_1 - ik_1)^2 - n_0^2 sin^2\theta_i}}{n_0 cos\theta_i + \sqrt{(n_1 - ik_1)^2 - n_0^2 sin^2\theta_i}} \tag{42}$$

$$r_p = \frac{-(n_1 - ik_1)^2 cos\theta_i + \sqrt{(n_1 - ik_1)^2 - n_0^2 sin^2\theta_i}}{(n_1 - ik_1)^2 cos\theta_i + \sqrt{(n_1 - ik_1)^2 - n_0^2 sin^2\theta_i}} \tag{43}$$

The reflectivity R is calculated as $R = r_s r_s^*$ and $R = r_p r_p^*$, respectively. In the realistic case, the polarization is random, so the reflectance R should be the average of both values.

The absorptions of silver, gold and copper are calculated and shown in Fig.41, Fig.42 and Fig.43, respectively. The absorption of silver film is the lowest in this three metal candidates. Less than 10% of scintillation photons will be absorbed at emission peak 435 nm. Compared with silver, gold and copper absorb 70% and 50% of the scintillation photons, respectively.

From above two dimensional (2D) results, we have known only silver can satisfy our request of high thermal conductivity and high reflectivity for CaF_2(Eu)'s scintillation light. In our detector, we have to consider three dimensional (3D) volume, so we should also confirm this result from 3D simulation.

In the same simulation model in this section, we can also confirm the absorption of silver film. Fig.44 shows the initial position distribution of photons which are absorbed by the silver film. The average absorption is only 0.13%, which can be considered to be negligible. Since the photons generated near the silver film ($Z =$

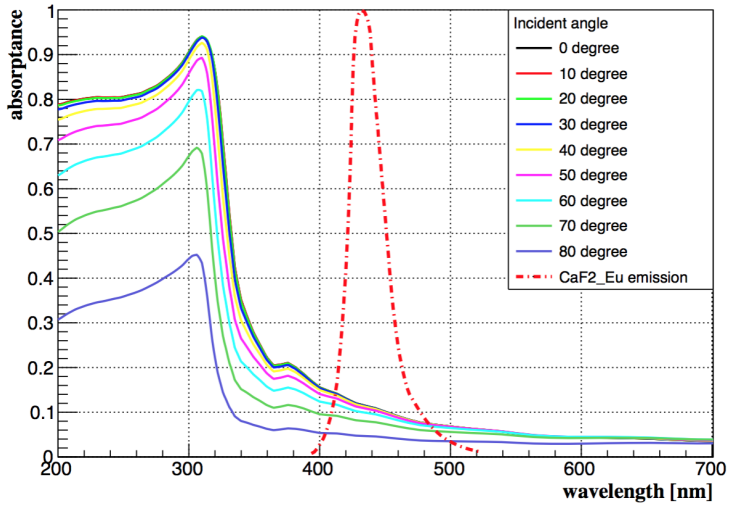

Figure 41: Angular wavelength dependence on absorption of silver film on the CaF_2(Eu) crystal surface. The red dotted line shows the emission spectrum of CaF_2(Eu) scintillator.

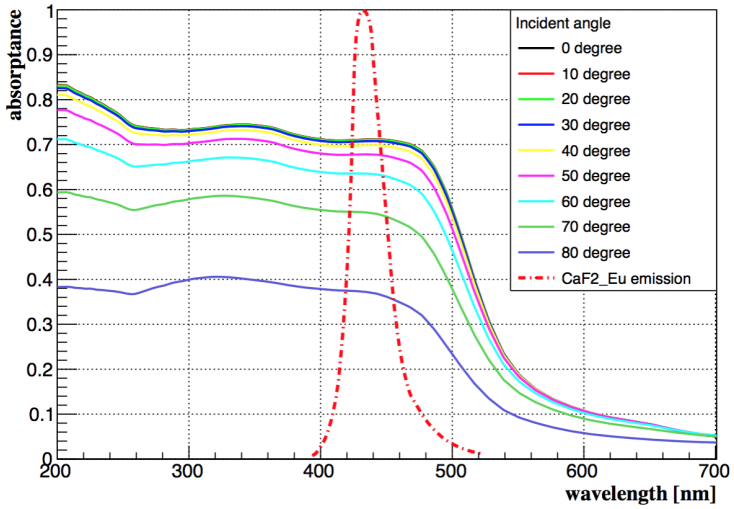

Figure 42: Angular wavelength dependence on absorption of gold film on the CaF_2(Eu) crystal surface. The red dotted line is as same as in Fig.41.

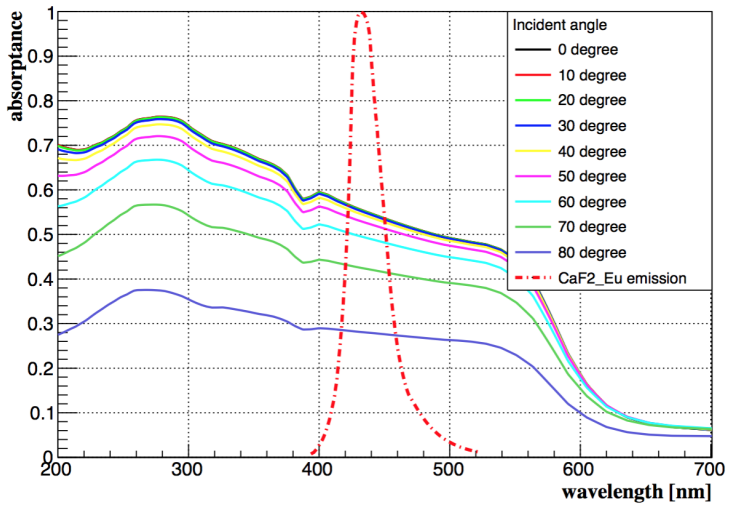

Figure 43: Angular wavelength dependence on absorption of copper film on the CaF_2(Eu) crystal surface. The red dotted line is as same as in Fig.41.

$-25\,\mathrm{mm}, 0\,\mathrm{mm}^2 < \mathrm{R}^2 < 100\,\mathrm{mm}^2$) are much easier to be absorbed than the ones further from the film, we can see a position dependence from the simulation result. Even though that is the case, the maximum of absorption is only 0.24%.

To compare the effect of silver film, I simulated the effect of gold film. Fig.45 shows the initial photons absorbed by gold film. Near the metal film, about 25% photons are absorbed, 100 times higher than silver film. In this case, when 1 MeV beta ray generated near the gold film gives 16 keV energy from photon to phonon, while the beta ray at the right-top corner doesn't give photon energy to phonon. If we employ gold film for our phonon collector, scintillation absorption will cause a maximum difference of 1.6% in the signal height.

5.7.3 Scintillation detection by light detector

Here I consider the third type of photon propagations, the scintillation photons detected by a light detector. In the design of our scintillating bolometer, there is only one light detector on the top of the crystal. This induces a position dependence for light detection. Fig.46 shows position distribution of generated photons that are

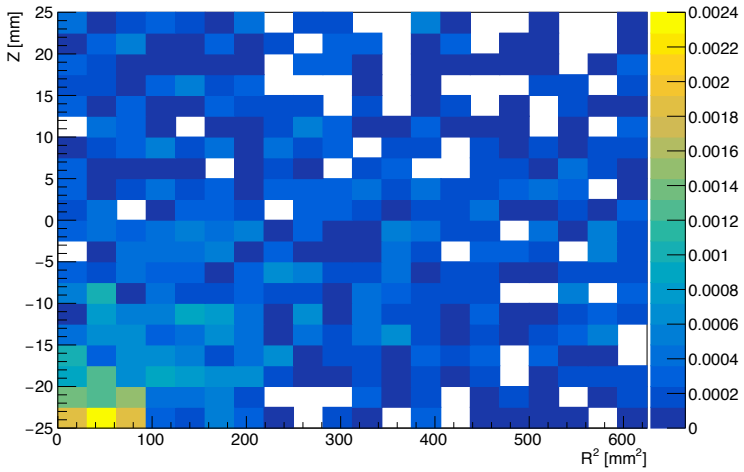

Figure 44: Position dependence of scintillation photon absorption by the silver film. The color in this figure shows the absorptance, which is represented by the ratio of absorbed photons by Ag film to generated photons at that position.

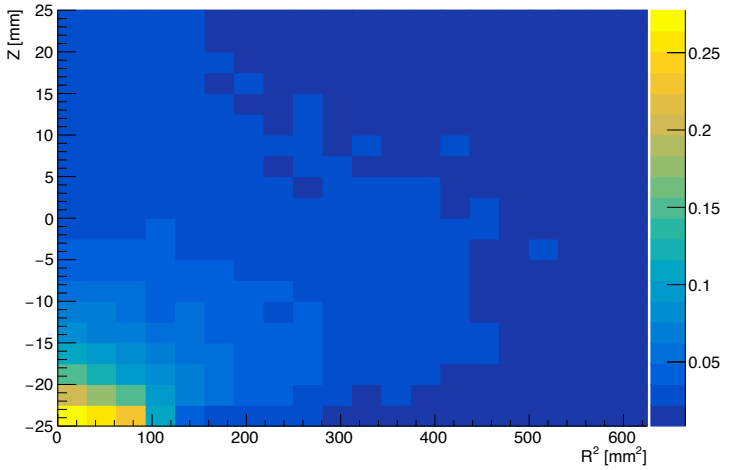

Figure 45: Absorption by Au film, as in Fig.44.

detected by Ge wafer. Photons generated near the Ge wafer have higher probability to be detected by the wafer, while the ones generated far from the Ge wafer and near the silver film have lower probability to be detected by it.

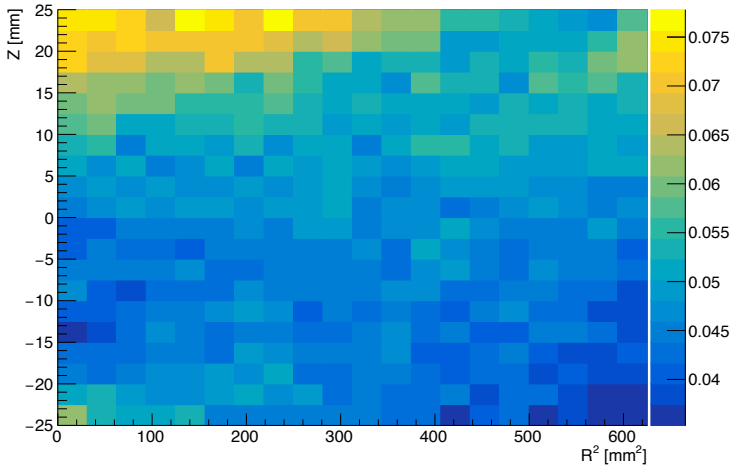

Figure 46: Position dependence of scintillation photon detection by the Ge wafer. The color in this figure shows the detection rate, which is represented by the ratio of detected photons by the Ge wafer to generated photons at that position. Here, the maximum detection rate is about 2 times of the minimum one in this simulation result. The reason of this large difference could be from the ideal crystal surface condition.

To understand the tendency of position dependence, I plotted one dimension histograms in Z axis and R^2 axis, respectively. Fig.47 shows the Z axis distribution. Larger Z region is near the Ge wafer, while smaller Z region is near the metal film. If events are generated near the Ge wafer, more scintillation light will be detected by light detector; if events are generated near the metal film, less scintillation light will be detected. This tendency seems to be opposite to the one of self-absorption in Fig.38. This effect comes from double readout system of heat and light, which will be explained in the section 6.3.1.

Different from Z axis distribution, there is much less difference in R^2 axis in Fig.48. There is only a slight dependence on the R^2 axis. The reason is self-absorption is more at the bottom-right corner as in Fig.46 and escape photons are

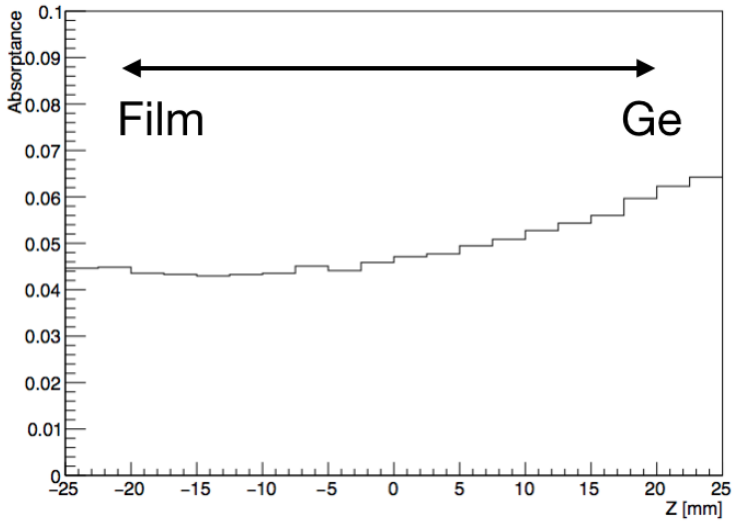

Figure 47: Position dependence of photons detected by the Ge wafer along the Z-direction of CaF_2(Eu) crystal.

more at the right-top corner.

The position distribution of photons escaped are shown in Fig.49. The photons generated at the top-right corner (near the gap) can easily escape from the detector module. The maximum probability to escape is found to be 11%. Near the bottom corner, photons are difficult to escape. The escape photons can be reduced by installing a suitable shape reflector to achieve 4π coverage.

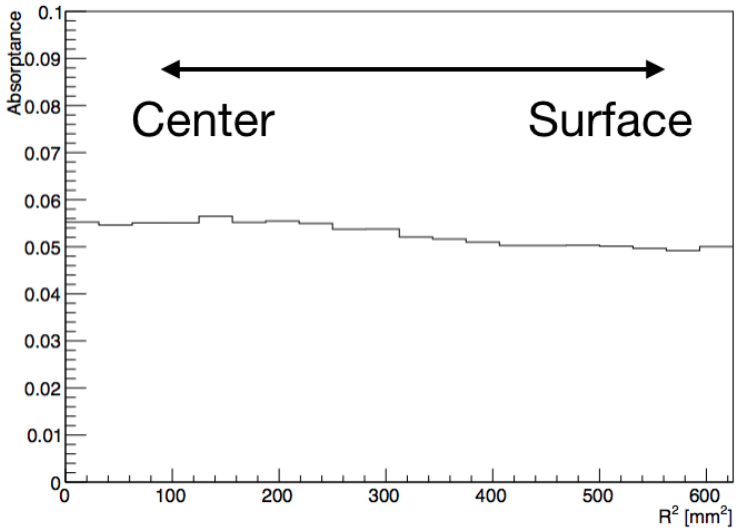

Figure 48: Position dependence of photons detected by the Ge wafer along the R^2-direction of CaF_2(Eu) crystal.

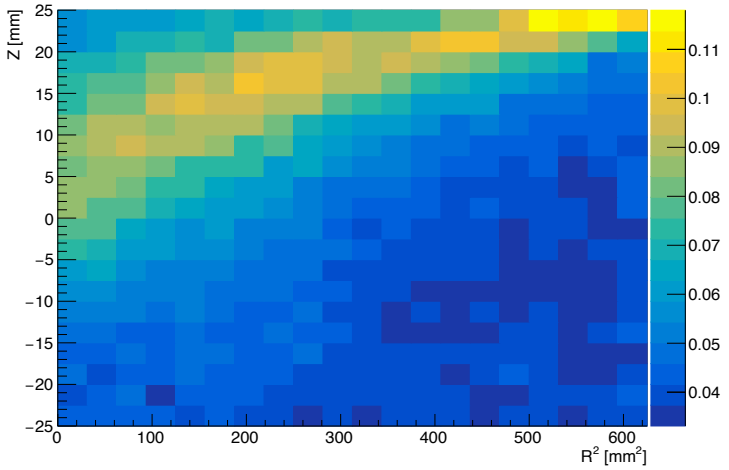

Figure 49: Position dependence of scintillation photons escaped from the detector module. The color in this figure shows the escape rate, which is represented by the ratio of escaped photons to generated photons at that position.

5.8 Cherenkov radiation of beta rays

When electrons from $0\nu\beta\beta$ decay pass through CaF_2(Eu) crystal at a speed greater than the phase velocity of light in the CaF_2(Eu) crystal, Cherenkov radiation will be emitted. Most of Cherenkov radiation distributes in the ultraviolet region. Therefore, only a small part of Cherenkov radiation could be absorbed by silver film to deteriorate energy resolution of heat signal. In this section, quantitative evaluation of Cherenkov radiation effect is performed.

The frequency spectrum of Cherenkov radiation by a particle is given by the Frank-Tamm formula [66]:

$$\frac{d^2E}{dx\,dw} = \frac{q^2}{4\pi}\mu(w)w\left(1 - \frac{1}{\beta^2 n^2(w)}\right) \tag{44}$$

The Frank-Tamm formula describes the amount of energy E emitted from Cherenkov radiation, per unit frequency w, per unit traveled length x. In the formula, $\mu(w)$ and $n(w)$ are the frequency-dependent permeability and index of refraction of the medium respectively, q is the electric charge of the particle, and $\beta = v/c$ where v is the speed of the particle, and c is the speed of light in vacuum.

In our experiment, two electrons with kinetic energy 2.1 MeV ($\beta \approx 1$) travel through CaF_2 medium while emitting Cherenkov radiations. The Cherenkov radiations, whose wavelength is shorter than 300 nm, will be absorbed by CaF_2(Eu) scintillator, because the cut-off wavelength of absorption spectrum of CaF_2(Eu) is 300 nm shown in Fig.50. From this, Cherenkov radiations shorter than 300 nm will not become a threat to deteriorate energy resolution. The most probability to make energy resolution worse is the component, shown in the pink region in Fig.50, between the cut-off wavelength of CaF_2(Eu)'s absorption spectrum (300 nm) and the one of silver's absorption spectrum (400 nm). The Cherenkov radiations in this region could transmit through CaF_2(Eu) crystal and be absorbed by silver film with a absorption coefficient more than 20%. Therefore, their total energy should be

calculated to check if they will become a serious problem.

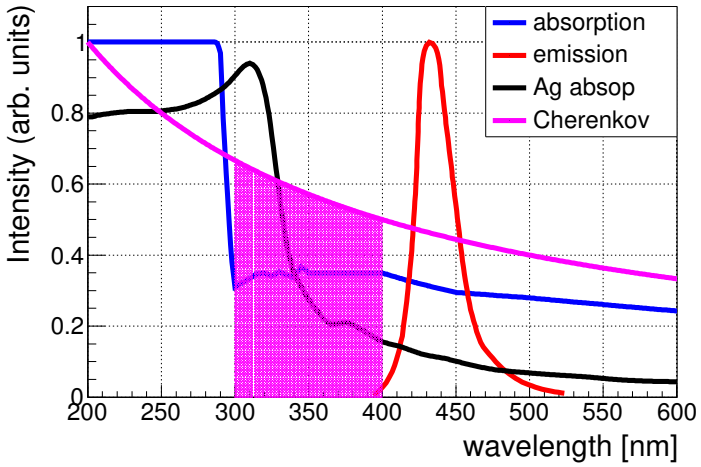

Figure 50: Effect of Cherenkov radiaiton.

Applying equation (44), we assume several conditions to evaluate the maximum effect of Cherenkov radiations. Firstly, the case could be supposed that high energy electron travels through CaF_2 scintillator with unchanged $\beta \approx 1$ in a distance $dx = 5\,\text{mm}$. Secondly, since CaF_2(Eu) is non-magnetic material and the variation of refraction index between 300 nm and 400 nm is just about 1%, $\mu(w) = 4\pi \times 10^{-7}\,\text{H/m}$ and $n(w) = 1.46$. Thirdly, we only care about the region between 300 nm and 400 nm, so $w = 1.07 \times 10^{15}\,\text{Hz}$ and $dw = 0.28 \times 10^{15}\,\text{Hz}$. As a result, the total energy of Cherenkov radiation $dE = 12.7\,\text{eV}$. Taking into account that the absorptance of silver film and light collection efficiency of detector module, the energy absorption of silver film from Cherenkov radiation is negligible.

5.9 Total understood mechanism of detector

Now we have considered about the physical processes, which are understood in normal scintillating bolometer system. We can conclude a total mechanism of the CaF_2(Eu) scintillating bolometer in Fig.51. When radiation deposits energy inside the CaF_2(Eu) crystal, about 94% of deposit energy generates high energy phonons. The high energy phonons thermalized the whole crystal and down-converted to equilibrium phonons through phonon-phonon scattering. The phonons were absorbed by the metal film phonon collector by phonon-electron interaction at the boundary of crystal and metal film. Finally, electrons in the metal film transfered heat to the MMC and the heat energy was detected.

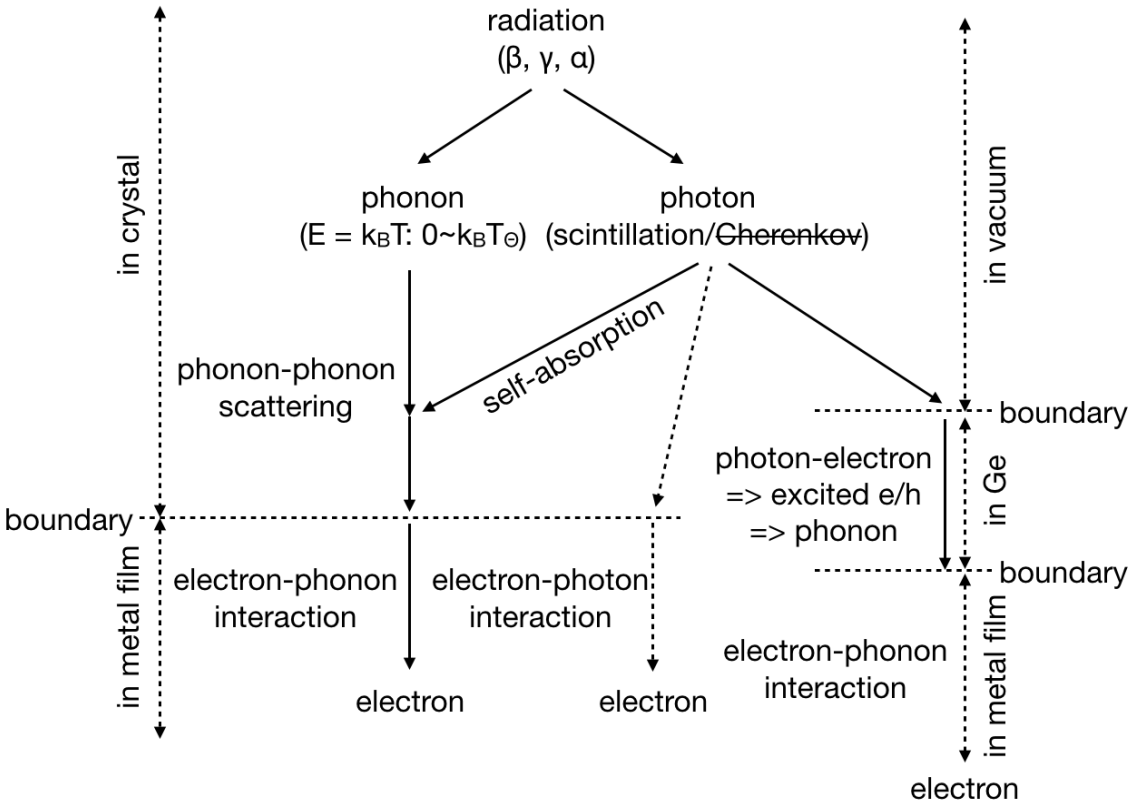

Figure 51: Total understood mechanism of the CaF_2(Eu) scintillating bolometer.

At the same time of phonon generation, 6% deposited energy transferred to

scintillation light. Since the attenuation length of CaF_2(Eu) is 6.5 cm, which is comparable with the length of crystal, 81% of scintillation light was absorbed by crystal itself. The metal film phonon collector made of silver film reflected well the scintillation light, so its absorption can be considered as negligible. Except 7% of scintillation photons escaping from the detector's gap, about 5% scintillation photons were detected by the light detector. The light detector was made by a Ge wafer. On the surface of Ge wafer, scintillation photons excited an electron-hole pair by phonon-electron interaction. When the excited electron-hole pair dropped to the ground state, the release energy generated phonons. The phonon-phonon scattering thermalized the Ge wafer and also interacted with electrons at the boundary of Ge wafer and gold films. As same as the phonon detection in the crystal, electrons in the gold films transfered heat to MMC and the scintillation energy was detected.

For beta rays, Cherenkov radiation is also emitted in the CaF_2(Eu) crystal. The short wavelength Cherenkov radiation vanishes immediately by self-absorption. The Cherenkov radiation between 300 nm and 400 nm is easy to be absorbed by the silver film, but the energy of radiation photons is 12 eV, which is negligible level and doesn't affect the detection performance.

5.10 Detector set-up

5.10.1 Scintillating bolometer assembling.

The complete scintillating bolometer of CaF_2(Eu) crystal is shown in Fig.52. In the top-left picture, the crystal was held by a hexagonal oxygen-free copper support. The weak thermal link between the crystal and the copper employed four PEEK plastics on the bottom and three PTFE-copper boards on the top. From inside, we can see the silver face with high reflectivity, where the image of smartphone camera is reflected. Next the silver film, a silicon heater was pasted onto the surface of crystal by Araldite.

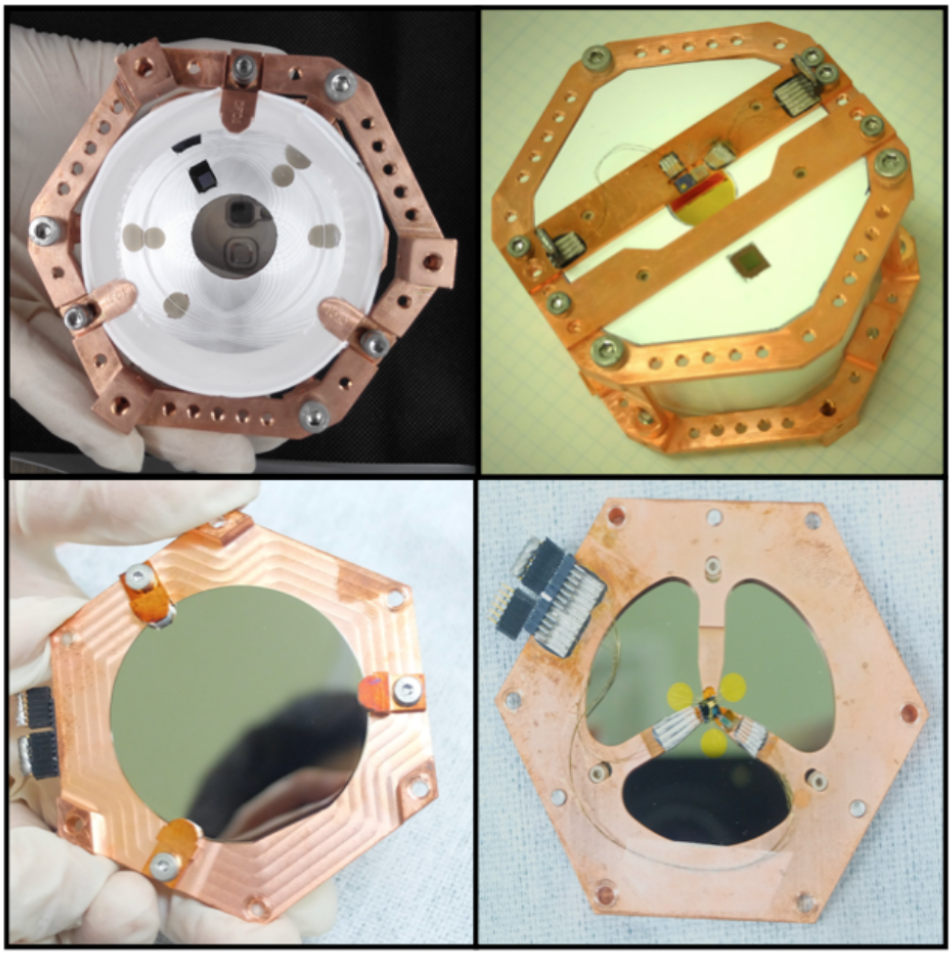

Figure 52: The pictures of detector set-up.

The top-right picture is in the view point of detector outside. On the opposite of silver film, gold film was thermally connected to the MMC, which was fixed on the copper plate by varnish. Next the MMC, there is the dc-SQUID circuit to convert the magnetization change to a voltage pulse. The wires used from the dc-SQUID to 1 K stage are superconducting wires.

The bottom-left picture is the face of light detector to the crystal. The 2 inch Ge wafer was fixed by three PTFE-copper supports, which works as a weak thermal link. The Ge wafer was 13 N high purity, purchased from Umicore company. The both sides of Ge wafer were etched.

The bottom-right picture shows the opposite face of Ge wafer. Three gold films were evaporated on the center. These three gold films were connected to the MMC, which was fixed on the copper plate, by gold wires. The MMC's magnetization change was also read out by a dc-SQUID next to the MMC.

5.10.2 Reflector selection

Scintillating bolometer needs a suitable reflector to collect the scintillation photons. A good reflector can collect more scintillation light and increase particle identification power using simultaneous measurement of heat and light. In the CUORE and AMoRE experiments, VM2002 light reflector (also known as ESR) from 3M company was selected, because VM2002 has an excellent reflectance more than 98% for visible light. In the case of ultraviolet light, especially which is shorter than 380 nm, VM2002 reflector is transparent and cannot work as a reflector. For CaF_2 scintillation crystals, scintillation emission peaks of CaF_2(pure) and CaF_2(Eu) are 280 nm and 435 nm respectively. Therefore, VM2002 reflector only matches CaF_2(Eu), but not CaF_2(pure).

In this measurement, I had to select a reflector with high UV reflectance for both CaF_2(Eu) and CaF_2(pure), because we also developed a scintillating bolometer with a CaF_2(pure) crystal. The reflector candidates at room temperature are Al (Alu-

minum) reflector and e-PTFE (expanded PolyTetraFluorEthylen). Al reflector is well known as a good mirror reflective material for UV light, for example MIRO-UV product of ALANOD company. However, Al will be superconducting below 1.2 K and absorb scintillation photons easily. Al reflector is not suitable for low temperature experiments. The e-PTFE is a commonly used reflector for both visible and UV light, for example, PTFE tape wrapping scintillation crystal for PMT application.

I carried out a measurement to confirm if the e-PTFE is a suitable selection for our scintillating bolometer with CaF_2 scintillators. I selected four different reflector materials, which are aluminum foil, PTFE tape, ePTFE sheet (0.5 mm) and ePTFE (1.0 mm), and mounted the crystal with them attaching to a PMT, respectively. Then I used ^{133}Ba source's 81 keV and 356 keV gamma rays and ^{22}Na source's 511 keV gamma rays to irradiate the crystal to observe the full energy peak in ADC channel. Fig.53 shows the relations of energy and ADC channel of four different reflectors. Since these measurements are carried out in the same condition, the slop of each reflector set-up can be considered as the reflectivity of the reflector. From the comparison of PTFE tape + Al foil and Al foil only, we can know the PTFE material works better than the Al foil. Since the PTFE tape is in the thickness of 80 μm, some photons could penetrate the tape which finally results in a loss of detection photons. To increase the photon collection efficiency, we should employ a PTFE material with enough thickness. I compared the results of PTFE tape + Al foil, PTFE sheet (0.5 mm) + Al foil and PTFE sheet (1.0 mm) + Al foil and confirmed the penetration of photons in the PTFE. Finally, I selected the thickest one, PTFE sheet (1.0 mm), as the reflector of our scintillating bolometers.

5.10.3 Dilution Refrigerator

In this measurement, we used a wet system dilution refrigerator in Fig.54, which is made by Leiden Cryogenics to carry out low temperature measurement. Leiden Cryogenics's dilution refrigerators have superior cooling power to the ones of

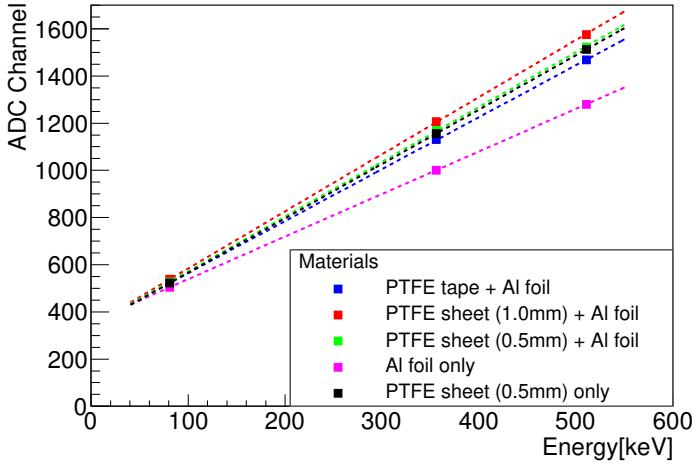

Figure 53: Light collections of different reflectors.

Oxford Instruments and BlueFors Cryogenics. At the moment, the most powerful dilution refrigerator (cryogen-free) in the world was made by Leiden Cryogenics and is employed by the CUORE experiment for neutrinoless double beta decay.

The dilution refrigerator used in this measurement is a MNK model MNK126-500 of Leiden Cryogenics, fabricated for low vibration setup. The achievable lowest temperature is 7 mK and cooling power at 120 mK is 500 μW. The main part below 1K pot stage is shown in Fig.54. Mixing chamber has a gold-plated copper bottom increasing thermal conductivity to provide a 10 mK plate. The CaF_2(Eu) scintillating bolometer is assembled to the plate by oxygen-free copper supporter.

10 cm thick lead shield was surrounding the cryostat to reduce radioactive radiations. However, this measurement is carried out in the above-ground laboratory, so the muon events can not be reduced.

5.10.4 Data acquisition system

The data acquisition (DAQ) system is shown in Fig.55. The magnetization change of MMC is read out by SQUID C6, the 6^{th} generation of the PTB sensor family. The SQUID is controlled by Magnicon XXF-1 electronics, which also works as a pre-

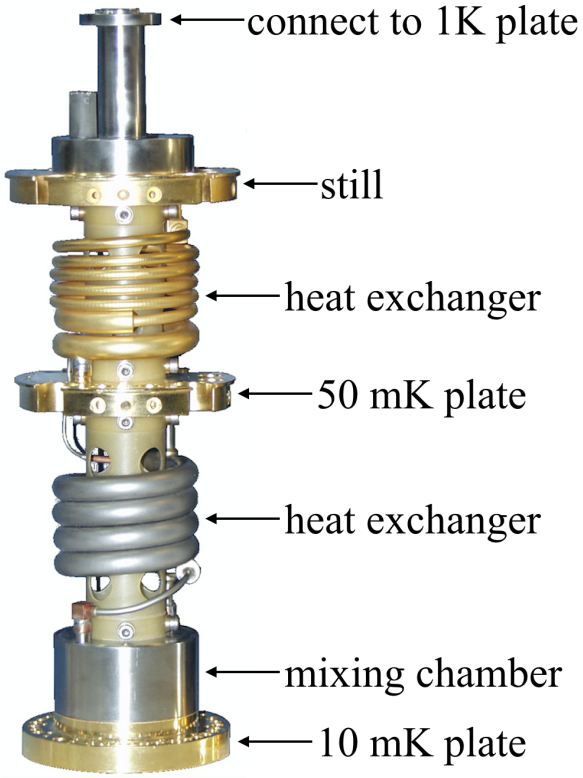

Figure 54: Dilution refrigerator (The picture is from www.leiden-cryogenics.com).

amplifier. The electronics has a voltage noise $0.33\,\mathrm{nV}/\sqrt{\mathrm{Hz}}$ and a 6 MHz bandwidth. A low-noise voltage preamplifier SR560 with a hardware low-pass filter from 100 kHz to 1 MHz to reduce high frequency noises is applied before digitizer module. The digitizer module together with PXI controller and PXI chassis are PXI system made by National Instruments. The digitizer module has 14-bits resolution and 100 MS/s speed. Both AC and DC coupling can be selected. In the measurement, we used 20 MS/s speed and saved after averaging each 10 samples for noise reduction.

Leading edge trigger with certain trigger level in the AC coupled signal is used. A high frequency rejection which is a function to ignore noise-induced triggers from high frequency noise exceeding 1 kHz. Since baseline level of DC signal is changed with temperature changes, dynamic range of DC signal is larger than the one of AC signal. This causes that AC signal has a lower digitizer noise, higher signal to noise ratio and lower pulse height. From this reason, we used AC signal as trigger

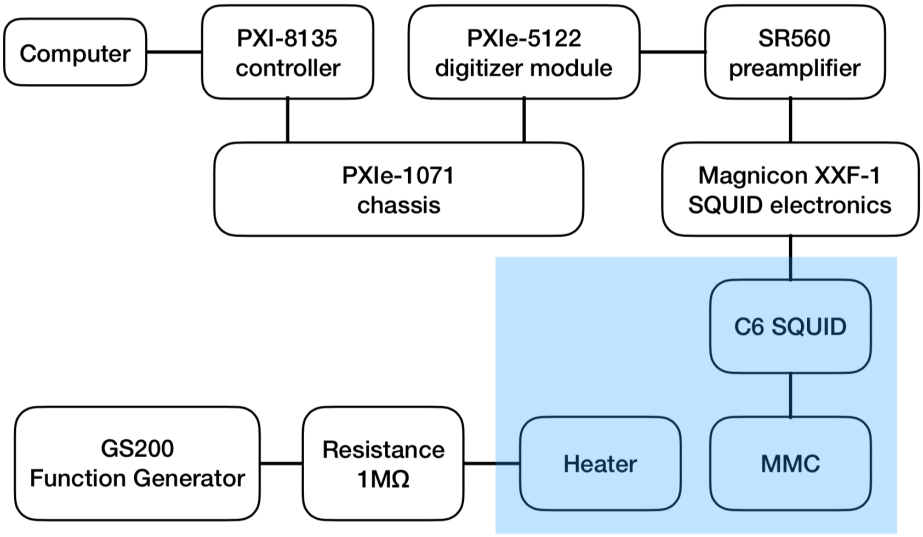

Figure 55: DAQ. The components in the blue region are at 20mK temperature.

information only, while DC signal was used for physics analysis.

A heater, which is a Au-Pd wire evaporated on a $3 \times 3\,\mathrm{mm}^2$ silicon chip, is attached on the crystal using ARALDITE epoxy adhesive. We injected a rectangular pulse with 3 V voltage height and 875 μs length to the heater through a 1 MΩ. The resistance of silicon heater path is 1 kΩ, which includes the Au-Pd wire's 0.7 kΩ resistance and the Manganin cable's 0.3 kΩ. The injection pulse creates $\sim$ 34 MeV heat on the silicon chip at the low temperature.

We cooled down the CaF_2(Eu) scintillating bolometer to a few 10 mK and detected phonons and photons at the same time. In the following section of data analysis, I will introduce the detection performance of our CaF_2(Eu) scintillating bolometer.

6 Data analysis

6.1 Result of simultaneous detection of phonon and scintillation

The result of this simultaneous detection for phonon and scintillation signals is shown in Fig.56. The X and Y axis is the pulse amplitudes of heat signal and light signal, respectively. The signal amplitudes showed several groups of events identified for beta/gamma band and internal alpha decays. The beta/gamma band has a maximum angle of inclination on the left of Fig.56. There are three clusters in the center of Fig.56. They are the alpha events with smaller light signals due to quenching factor. An extensive cluster on the top-right of three alpha events is from beta-alpha continuous decays. In the beta-alpha continuous decay events, the beta component has a high light/heat ratio and a continuous distribution, while the alpha component has a lower light/heat ratio and a cluster distribution. Therefore, the beta-alpha continuous decay events have a continuous distribution and a slop that is lower than the beta/gamma band, but higher than the alpha groups. Apart from the three main alpha clusters, there is a small cluster in the bottom-left alpha region. These events could be alpha decays from impurities of the CaF_2(Eu) crystal. We can identify these events substantially using information of data analysis and some reference.

The alpha decays are mainly from ^{226}Ra decay series, which consists of ^{226}Ra, ^{222}Rn and ^{218}Po. The ^{226}Ra is melted out of bedrocks or walls, and a well-known background source in the underground experiments. Since commercial crystals are not grown in the radiation-pure environment, they have a high level impurity of ^{226}Ra. The ^{226}Ra has a half-life as long as 1600 years, so many ^{226}Ra nuclei are still remaining in our CaF_2(Eu) crystal. The ^{226}Ra has a daughter nuclide ^{222}Rn with a half-life of 3.8 days and the ^{222}Rn also has a daughter nuclide ^{218}Po with a half-life of 3.1 minutes. In nature, when parent nuclide has a half-life much longer

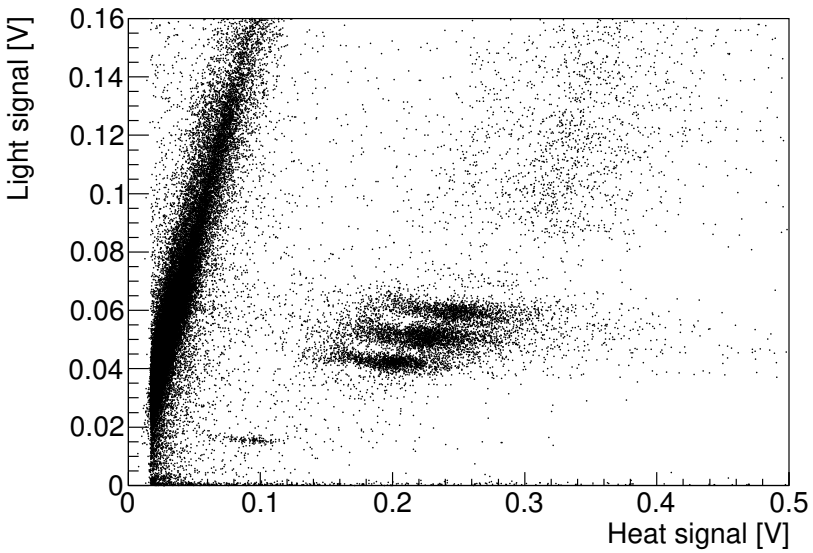

Figure 56: Pulse height distribution of heat and light signals.

than the daughter nuclide, they will maintain a radiation equilibrium and have the same decay rate. In Fig.56, the three alpha clusters with the similar event numbers are mainly from the ^{226}Ra, ^{222}Rn and ^{218}Po. These alpha backgrounds are also confirmed in another experiment using a commercial CaF_2(Eu) crystal [67].

The small alpha cluster in the bottom-left of Fig.56 was reported from ^{147}Sm [67]. When people dope europium (Eu) into the crystal grow process, a small amount of samarium (Sm) and gadolinium (Gd) could be mixed as impurities of europium source, because the atomic numbers of Sm (62) and Gd (64) are next to that of Eu (63). In the isotopes of Sm and Gd, only ^{147}Sm, ^{148}Sm and ^{152}Gd can decay alpha in about 2 MeV region. Their natural abundances (N.A.), decay energies and half-lives are listed in table.6. Since the impurity amount of Sm and Gd should not be so different and the half-lives of ^{148}Sm and ^{152}Gd are 3 order of magnitude higher, we can conclude the single alpha peak is from ^{147}Sm.

From Fig.56, we can see the discrimination power of alpha events and beta/gamma events is quite good. The light signal has a good resolution that separate the three

Table 6: Impurity of ^{147}Sm

Isotope	N.A.	Energy(MeV)	$T_{1/2}$(year)
^{147}Sm	15.0%	2.31	1.1×10^{11}
^{148}Sm	11.3%	1.99	7.0×10^{15}
^{152}Gd	0.2%	2.21	1.1×10^{14}

clusters of ^{226}Ra, ^{222}Rn and ^{218}Po. However, the heat signal is in a wide distribution by some reason. In the following sections, I will introduce each of them in order.

6.2 Discrimination of alpha and beta/gamma events

In most of scintillators, light yields of beta/gamma and alpha events are different due to quenching effect. The reason of quenching effect can be interpreted from the difference of deposit energy $\mathrm{d}E$ in unit distance $\mathrm{d}x$, $\mathrm{d}E/\mathrm{d}x$. The gamma ray is multi-site event that deposits energy in several positions, so the deposit energy at each position is small. The beta ray is not multi-site event, but the range is in the order of magnitude of a few mm. However, the range of alpha ray is point-like event with a range of few μm. In the short range of alpha ray, the electrons that can be excited to the excited state by the deposit energy are limited, so there is less scintillation photons emitted by alpha events than beta/gamma events.

In a scintillating bolometer, quenching effect provides a high discrimination power between electron and alpha events. We used the relative ratio of light to heat signal as a parameter of discrimination power. Since there is no quenching in the heat signals for different types of particles, we compared the ^{226}Ra events with the β/γ events in the same pulse height of heat signals (Fig.57). The peak at the light/heat ratio equal to 0.3 is alpha events, while the one at the light/heat ratio equal to 1.7 is beta/gamma events. A Gaussian function is used to fit the distribution of light/heat ratios of each α and β/γ events. Using the mean values (μ_α, $\mu_{\beta/\gamma}$) and the sigma values (σ_α, $\sigma_{\beta/\gamma}$), we obtain a discrimination power (DP) of 10 σ, which is calculated as

$$\mathrm{DP} = \frac{|\mu_{\beta/\gamma} - \mu_\alpha|}{\sqrt{\sigma^2_{\beta/\gamma} + \sigma^2_\alpha}}. \tag{45}$$

Compared with our CANDLES detector's discrimination power of 2.3 σ, we achieved a significant improvement to reduce background. In the $0\nu\beta\beta$ decay search, ^{208}Tl's 5.0 MeV beta decay is a serious background source. To reduce this background, we have to tag its parent nuclei ^{212}Bi's alpha events and veto a few minutes. In the case of 2.3 σ, some ^{212}Bi's alpha events cannot be tagged and their daughter ^{208}Tl's 5.0 MeV beta decay will become background. Now the CaF_2(Eu) scintillating bolometer

can clearly identify the ^{212}Bi's alpha events, the rejection of ^{208}Tl's 5.0 MeV beta decay background can be improved.

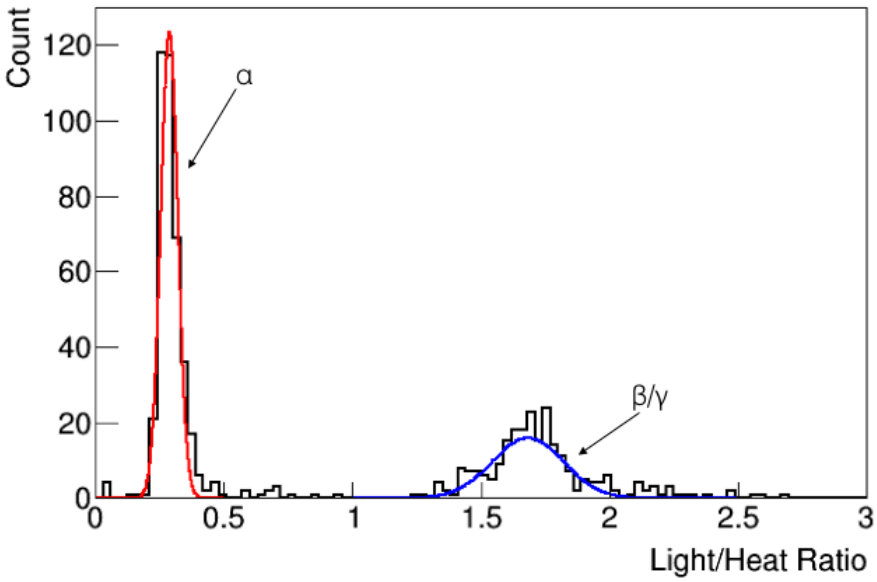

Figure 57: Discrimination power between β/γ and α events near 4.9 MeV region.

This strong discrimination power originates from the high light yield of the CaF_2(Eu) crystal and a large quenching in scintillation mechanism. A quenching factor $\mu_\alpha/\mu_{\beta/\gamma}$ of about 17% is found for the events in 4.9 MeV region. At the room temperature, the quenching factor of ^{226}Ra events was also reported as 17% [67]. This is an interesting point, because we have known the light yield of CaF_2(Eu) doesn't have temperature dependence. Now we found the quenching factor doesn't change at 20 mK either.

6.3 Light signal analysis

6.3.1 Resolution of light signal

In the simulation, we have explained there is anti-correlation between light and heat pulse amplitudes. This effect is a characteristic in double readout system, such as simultaneous detection of heat and light or simultaneous detection of ionization charge and light. In the case of scintillating bolometer, the double readout system shows an anti-correlation between light and heat signals as seen in a similar detection system [50]. When we evaluate the resolution of double readout system, we should correct the correlation to obtain the best resolution results.

The relation of anti-correlation and resolution is shown in Fig.58. In the graph of heat vs light, event cluster has an anti-correlation slop. The projections of event cluster in the heat axis and light axis are two gaussian distributions. In general, the resolution of heat signal is much better than that of light signal, but it's not the best solution of detector's resolution. We can correct the anti-correlation angle θ and determine a new axis as energy to obtain a better resolution.

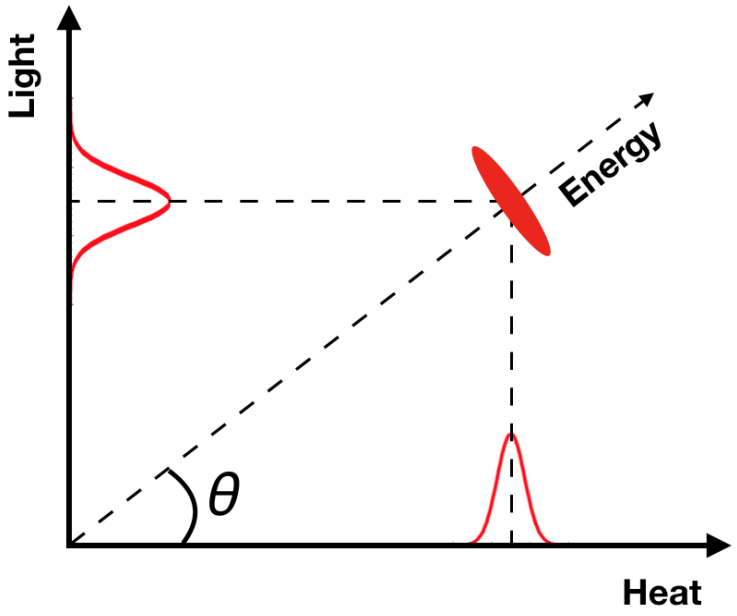

Figure 58: Scheme diagram of relation of anti-correlation and resolution.

In Fig.56, we also observed an anti-correlation in the alpha clusters. To evaluate the resolution of light signal, we have to correct the anti-correlation angle. At first, we plotted a light signal pulse height distribution of alpha events in Fig.59. The four peaks from the left side to the right side are ^{147}Sm, ^{226}Ra, ^{222}Rn + ^{210}Po, ^{218}Po, respectively. Here, we added ^{210}Po in the alpha clusters, because the third peak should have at least two components. In radiation equilibrium, ^{226}Ra, ^{222}Rn and ^{218}Po should have the same event rate, their peak heights should become lower when energy increases. However, the ^{222}Rn peak is the highest and its deviation is also larger than other two peaks. We estimated that at least one more component mixed into the ^{222}Rn peak. In the uranium series, the most energeticly possible candidate is ^{210}Po.

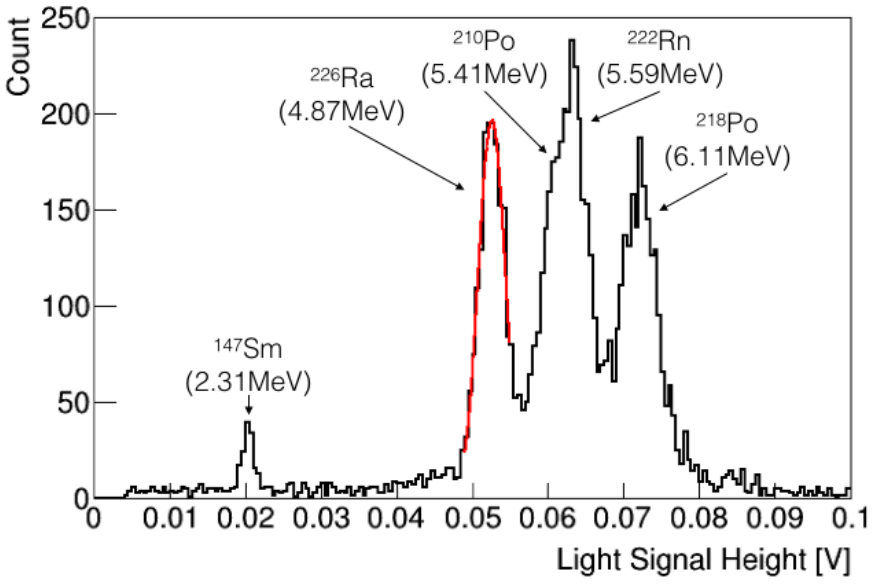

Figure 59: Resolution of ^{226}Ra events. The peak of ^{226}Ra is fitted by a single Gaussian function.

We employed ^{226}Ra event peak to evaluate the light signal's resolution, because its energy is the closest to the $Q_{\beta\beta}$ value 4.27 MeV. The ^{226}Ra peak was fitted with a single Gaussian function. The ratio of the sigma value to the mean value is the light signal's resolution at the angle θ. Then we changed the angle θ one degree by

one degree and calculated each resolution. The result of relation between correlation angle and resolution from 84° to 88° is shown in Fig.60. The best resolution is found at 87°, which means the true correlation angle. With the anti-correlation correction, three groups of α events can be notable in the α spectrum in Fig.59. The resolution of the 4.9 MeV ^{226}Ra events is $\Delta E_{\sigma} = 3.1\%$.

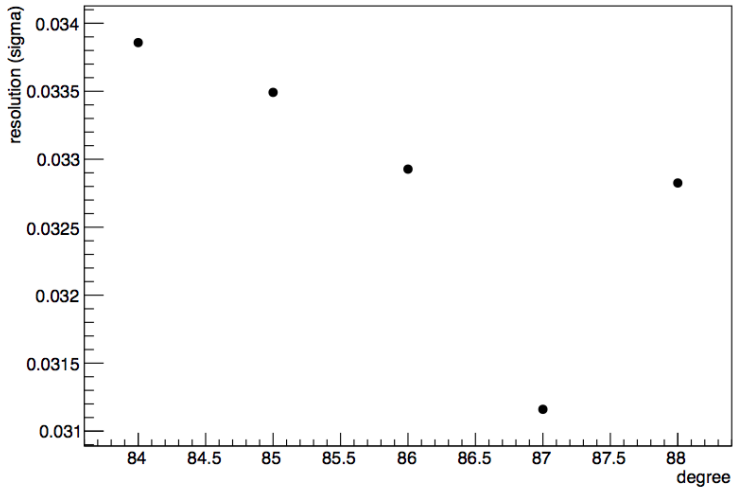

Figure 60: Resolution vs anti-correlation angle.

Now we have known the resolution of 4.9 MeV ^{226}Ra events is 3.1% (σ). Since the quenching factor at 4.9 MeV is 17%, the beta/gamma events in the same energy region should have 5.9 times more light yield. In an assumption that the light signal's resolution depends on the statistics of photons, we can estimate the beta/gamma events at 4.9 MeV have a resolution of $3.1\%/\sqrt{5.9} = 1.3\%$. The resolution of our current running CANDLES experiment is about 2.5%, so the light signal's resolution of our CaF_2(Eu) scintillating bolometer is 90% better than that of the CANDLES detector. Compared with the ELEGANT VI experiment that also used CaF_2(Eu) scintillator, the resolution is also improved by 46% from 1.9% to 1.3%.

6.3.2 Energy calibration in the light channel

In this measurement, we used a R&D detector to test the low temperature performance of $CaF_2(Eu)$ scintillating bolometer. The purpose is to evaluate its discrimination power and resolution. The energy calibration is not so important in this stage, but we still attempted to calibrate the energy of light signals with alpha events.

We used four peaks in Fig.61 to calibrate the energy scale, which are ^{147}Sm, ^{226}Ra, ^{218}Po and ^{216}Po. ^{147}Sm is from the impurities of europium, ^{226}Ra and ^{218}Po are from the Ra series' radiation equilibrium. However, we found the ^{218}Po 6.1 MeV peak is wider than our prediction and it has a tail at 0.08 V. At light signal height equal to 0.085 V, there is also a peak-like group. There is no candidates for them in ^{238}U series, so we supposed the existence of backgrounds from thorium series. 6.2 MeV ^{212}Bi and 6.4 MeV ^{220}Ra could mix into the ^{218}Po 6.1 MeV peak. The peak at 0.085 V could be 6.9 MeV ^{216}Po events. In this assumption, we fitted the peaks of ^{147}Sm, ^{226}Ra, ^{218}Po and ^{216}Po by single gaussian functions and calculated their mean values.

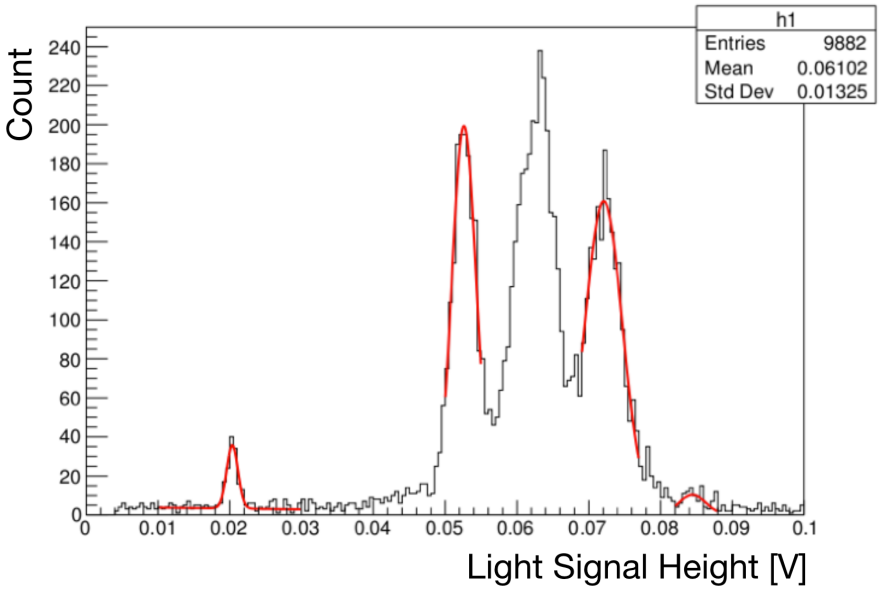

Figure 61: Fit of four peaks, ^{147}Sm, ^{226}Ra, ^{218}Po and ^{216}Po.

The mean values and their true energies are plot in Fig.62. The correlation is non-linear because of energy dependence of the quenching factor. At room temperature, CaF_2(Eu)'s quenching factor linearly increases with energy from 2 MeV to 9 MeV. At 2 MeV, the quenching factor is 13%, while at 9 MeV it increases to 24% [67]. In our low temperature data, we also observed that 2.3 MeV ^{147}Sm events have a lower light yield than the prediction from the 4.9 MeV ^{226}Ra events in Fig.56. Thus there should be also an energy dependence of quenching factor at low temperature, which results in the non-linearity of light signal height to the true energy. To calibrate this non-linear correlation, we found a power function is the best solution to fit the four correlation points in Fig.62.

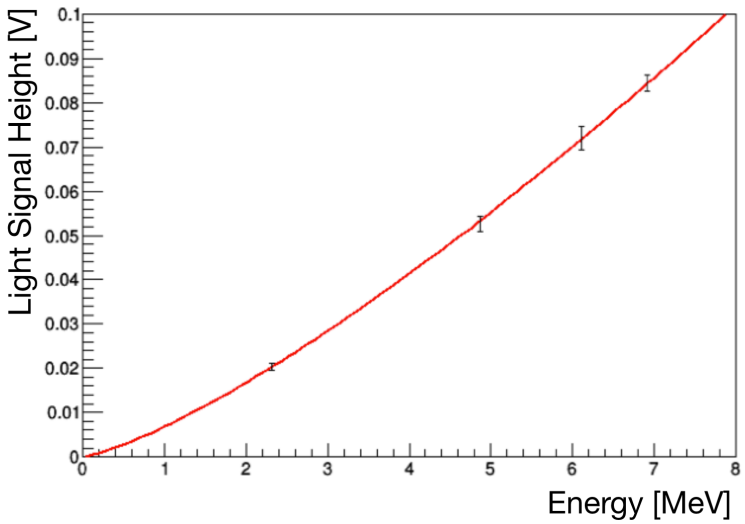

Figure 62: Power function fit of light signal height of α events. The error of each point uses the sigma value of the single peak fitting in Fig.61.

A good calibration should be consistent with all of candidate peaks in Fig.61. The candidates consist of uranium series, thorium series and Sm impurity. In table.7, we list all of background sources that could be contained in the CaF_2(Eu) crystal. Each background source should have a gaussian distribution. The mean value of each gaussian distribution should follow a power function of energy E; the sigma value of each distribution should obey a function of $\sqrt{E}$ due to the photon statistics.

Table 7: Assumed internal α backgrounds.

Uranium series [MeV]	Thorium series [MeV]	Other component [MeV]
^{238}U (4.27)	^{232}Th (4.08)	^{147}Sm (2.31)
^{234}U (4.86)	^{228}Th (5.52)	
^{230}Th (4.77)	^{224}Ra (5.79)	
^{226}Ra (4.87)	^{220}Rn (6.40)	
^{222}Rn (5.59)	^{216}Po (6.91)	
^{218}Po (6.11)	^{212}Bi (6.21)	
^{210}Po (5.41)		

The fitting result is shown in Fig.63. The red line is the fitting function of total alpha backgrounds, where each background of uranium series was redrawn as a green gaussian function, the one of thorium series is redrawn as a blue gaussian function and the samarium background is the pink gaussian function. The order of the candidate peaks is dependent of the energy that was listed in table.7. The power function determined by this fitting result is

$$V_L = 6.7 \times 10^{-3} \cdot E^{1.3}, \tag{46}$$

where V_L is pulse height of light signal in unit of voltage and E is the energy in unit of MeV. The errors of two factors in function.46 is less than 1%.

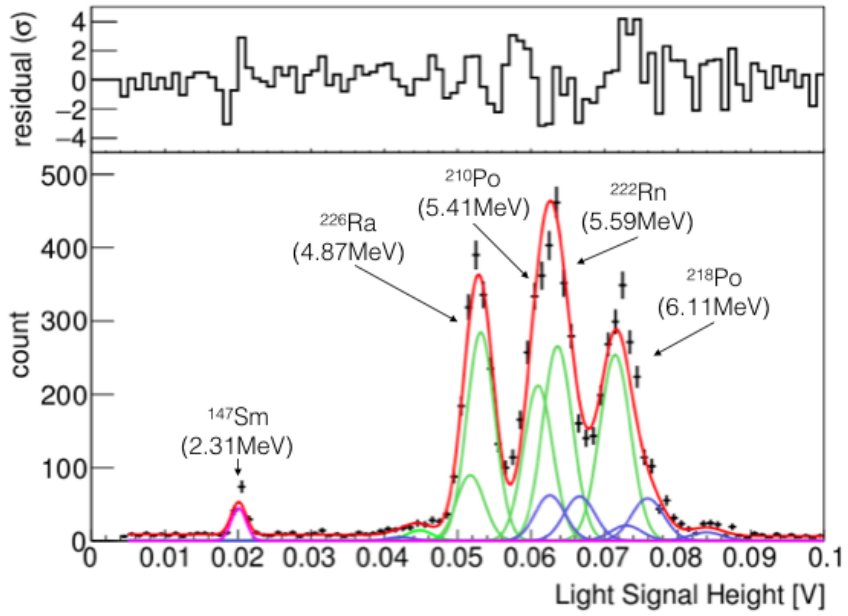

Figure 63: Background fitting of alpha spectrum. $\chi^2/\mathrm{ndf} = 2.4$.

6.4 Heat signal analysis

About heat signal's resolution, we analyzed the resolution of silicon heater pulse and physics events of alpha background. We found the silicon heater's resolution has achieved our goal of 0.5% (FWHM), while the one of physics events are much worse than our prediction. This section will introduce the details.

6.4.1 Resolution of heater's signal

It has been introduced in the part of detector development that a silicon heater was attached on the crystal to provide reference signals for heat channel. The reference signal of heater pulse can tell us if the crystal has been cooled to the preset temperature. It can be also used as a correlation parameter for temperature change by the dilution refrigerator's vibrations. For example, Fig.64 shows the heater signal's pulse height change over time. From 0 to 20 hours, we were cooling the crystal down to 20 mK, so the crystal's temperature was going down all the time. From 22 to 68 hours, the heater signal's pulse height kept almost constant, thus we can decide the crystal's temperature has reached 20 mK already. When the crystal was kept to 20 mK, the crystal's temperature rapidly fluctuated sometimes, such as the shift at 28 hours or 55 hours. The reason of these rapid fluctuation is dilution refrigerator's vibration. At the timing of 55 hours, a heavy liquid N_2 tank was moved near the refrigerator, which resulted in a serious vibration of the cooling system, then the pulse height of heater signal went down suddenly and took 2 hours to return to the original state.

The resolution of heater signal looks very good in Fig.64. We selected the events in a stable region between 28 and 32 hours to calculate the resolution. The distribution of their pulse height is shown in Fig.65. The distribution is gaussian-like, so we fitted it with a single gaussian function to obtain the sigma $\sigma_{\text{heater}} = 0.66$ mV and the mean $\mu_{\text{heater}} = 1.36$ V. The resolution is 0.11% (FWHM). In general, resolution decreases with square root of pulse height. At 0.2 V that is the average of signal heights

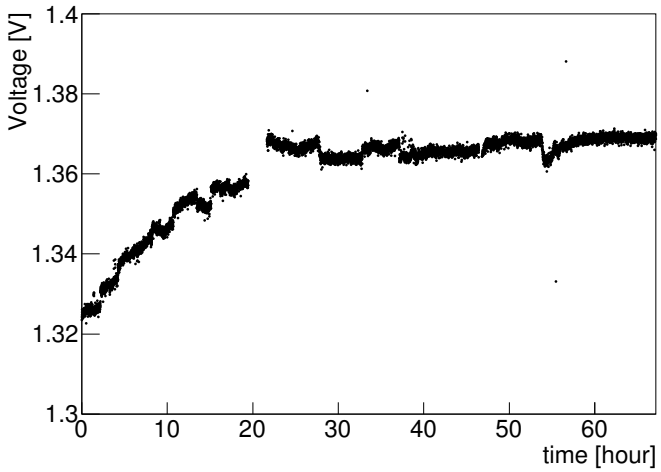

Figure 64: Temperature dependence of heater signal's pulse height.

of ^{226}Ra events, the heater signal has a resolution of $0.11\% \times \sqrt{1.36/0.2} = 0.29\%$. This result has already satisfied our goal of resolution, 0.5% (FWHM).

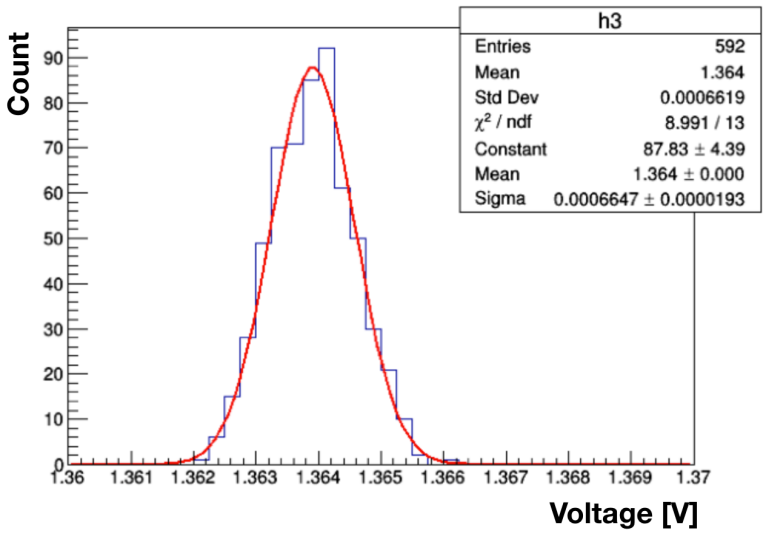

Figure 65: Resolution of heater signal's pulse height between 28 to 32 hours.

In scintillating bolometer experiments, the moving average of heater signal's pulse height can be used as a parameter for temperature correction. We used the average of its pulse heights in each 0.1 hour as the temperature reference parameter. The time dependence of temperature reference parameter is shown as the red line in Fig.66. We can correct the temperature fluctuation by dividing the heat signal's

pulse height with the reference parameter in that time region. In the case of temperature correction of heater signal, the result is shown in Fig.67. Almost all the heater events are normalized to 1.0.

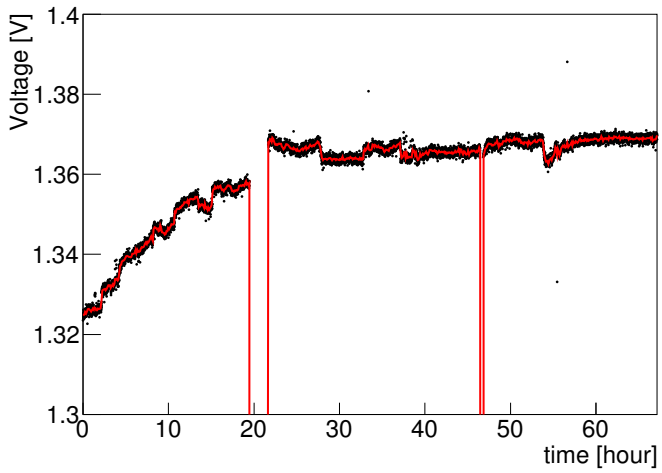

Figure 66: Moving average of heater pulse.

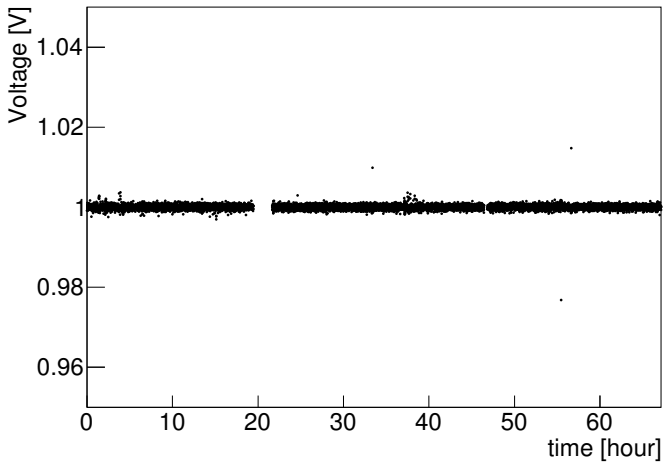

Figure 67: Normalized heater pulse after temperature correction.

Here, the average time used 0.1 hour in the temperature correction process. The reason of this selection is to keep the resolution of heater pulse after temperature correction consistent with the intrinsic resolution of heater pulse. If we use a much

shorter time, the corrected heater pulse's resolution will become divergence, which is meaningless for the temperature correction. If we use a much longer time, the temperature correction can not work well enough. The best solution is to find a time width that can keep the heater pulse's resolution same before and after the temperature correction. In the case of 0.1 hour, the resolution of heater pulse after temperature correction is also 0.11% (Fig.68), which is consistent with the one before the temperature correction.

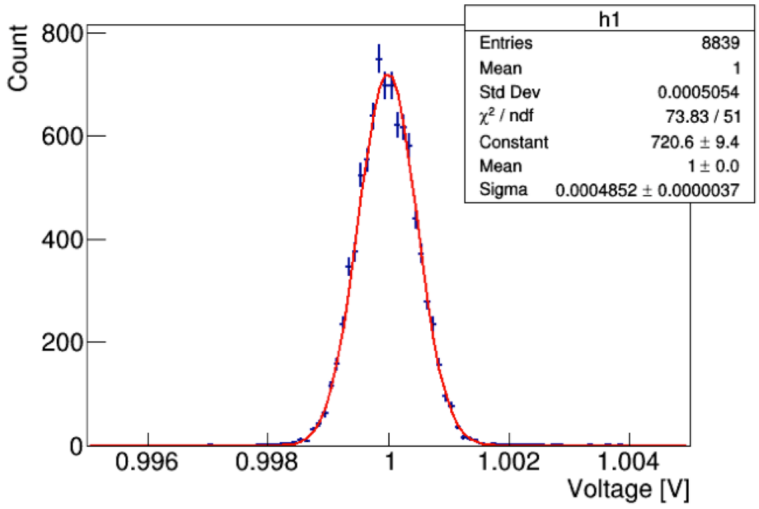

Figure 68: Energy resolution of heater pulse after temperature correction.

6.4.2 Resolution of alpha events

We have confirmed that our scintillating bolometer achieved an excellent resolution by evaluating heater signals. However, the resolution of alpha events looks very bad in Fig.56. Fig.69 shows the distribution of pulse height of ^{226}Ra in the heat channel. This distribution doesn't obey a gaussian distribution, so we use RMS to evaluate its resolution. Its resolution is equal to 29% (FWHM), which is 2 orders of magnitude worse than the silicon heater.

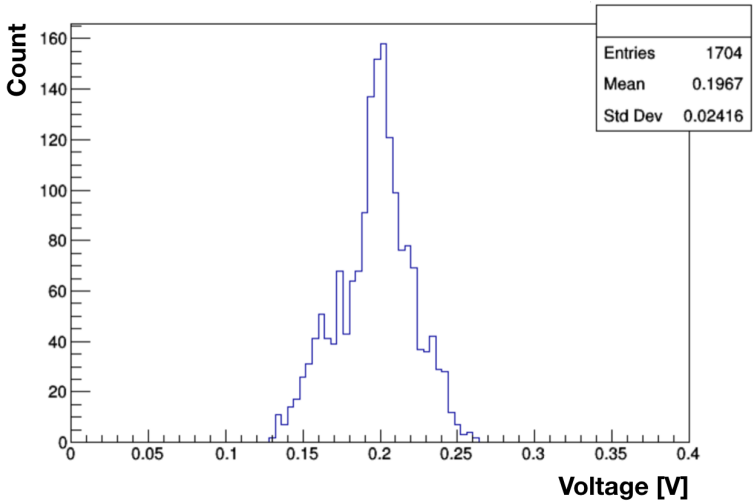

Figure 69: Distribution of pulse height of ^{226}Ra events in the heat channel.

The reason of this resolution deterioration can not be interpreted by temperature fluctuation and self-absorption of scintillation photons. The temperature fluctuation deteriorated the resolution from 0.11% to 0.38% in Fig.64, so it could induce 1.0% (FWHM) fluctuation in the region of ^{226}Ra events. The self-absorption of scintillation photons has a position dependence, but the deviation of energy contribution is only 0.13%. Both of this two cases cannot explain the resolution of 29%.

Here, we proposed a hypothesis that a position dependence exists in the heat channel. The silicon heater attached on just one position of the crystal surface, while the alpha events are distributed uniformly in the whole crystal. If the position dependence really exists, we can study the alpha-alpha continuous decay events to

confirm it. The following section will introduce that process.

6.5 Position dependence

The silicon heater's resolution is 0.29% (FWHM) corresponding to 4.9 MeV events, which satisfies our resolution goal of 0.5% (FWHM). However, the heat signals of internal alpha events have a wide distribution. This resolution difference could be induced by event's location, because the silicon heater is localized at one place of the crystal surface, while the internal alpha events are uniformly distributed in the whole crystal. A position dependence could exist and deteriorate the detector's resolution. To confirm this hypothesis, we employ alpha-alpha continuous decay of radon series. Since ^{218}Po's alpha decay has a half-life of 3 minutes, it's possible to detect the decay coincidence of ^{222}Rn$\rightarrow^{218}$Po$\rightarrow^{214}$Pb. The free path of alpha rays in CaF_2(Eu) is in the order of μm, so the parent alpha from ^{222}Rn and the daughter alpha from ^{218}Po can be considered to have the same position. If the position dependence exists, when the parent alpha has a large signal, its daughter alpha should also have a large signal; when the signal of parent alpha is small, the daughter alpha's signal should also be small. Thus a correlation line should appear in the two dimensional distribution of the signal heights of ^{222}Rn and ^{218}Po. The slop of correlation line should be equal to the decay energy ratio of ^{218}Po to ^{222}Rn.

We used every ^{222}Rn signal as trigger and tagged all ^{218}Po events within 3 minutes after the trigger. Fig.70 shows the signal amplitudes of ^{222}Rn events and their following ^{218}Po signals within 3 minutes. The events show a wide distribution of their amplitudes. However, the consecutive pairs also characterize a clear correlation line with the amplitudes proportional to each other likely originating from two α decays of ^{222}Rn$\rightarrow^{218}$Po$\rightarrow^{214}$Pb in the crystal. It indicates the position dependence exists in the heat channel.

To verify the correlation line indeed originates from ^{222}Rn$\rightarrow^{218}$Po$\rightarrow^{214}$Pb, we calculated the slop of correlation line and the decay time of decay coincidence events. We drew a line along the correlation line and obtained the slop value from ROOT application. The slop is consistent with the decay energy ratio of ^{222}Rn/^{218}Po.

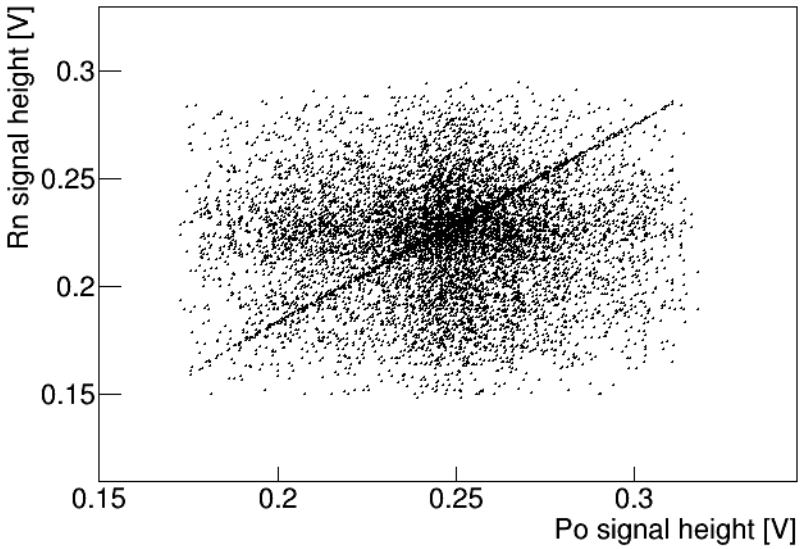

Figure 70: Evidence of position dependence.

To calculate the decay time, we changed the time window from 3 minutes to 6 minutes. We selected the decay coincidence events nearby the correlation line and drew a histogram of time difference between ^{222}Rn and ^{218}Po in Fig.71. A sum of an exponential function and a constant function is used to fit the distribution. The parameter of constant function is fixed by fitting the accidental background. The decay time of exponential function is $\tau_s = 213.8 \pm 17.9$ s with $\chi^2/\mathrm{ndf} = 0.5$, which is consistent with ^{218}Po's decay time 186.0 s.

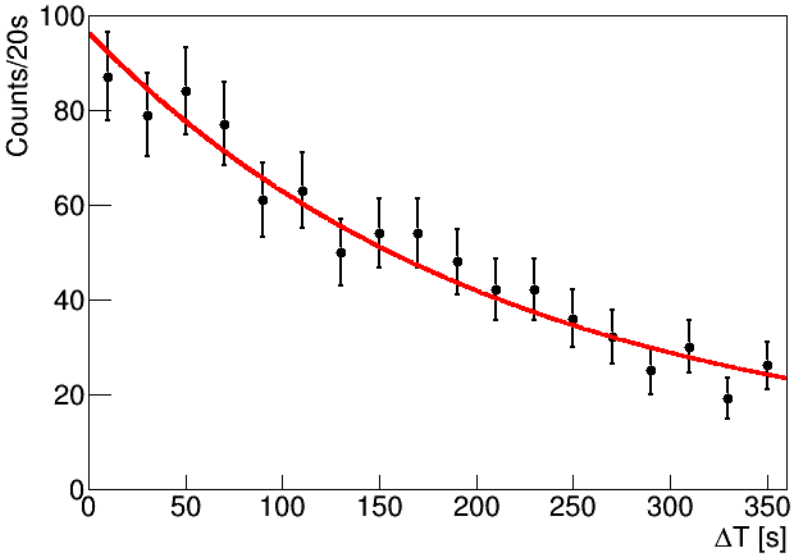

Figure 71: Decay time of sequential decay of ^{222}Rn$\rightarrow^{218}$Po$\rightarrow^{214}$Pb.

6.6 Intrinsic resolution of CaF_2(Eu) scintillating bolometer

From Fig.70, we realized the resolution without position dependence is quite good. Here, we define the resolution without position dependence as intrinsic resolution of the detector. We can calculate the intrinsic resolution using the ratio of signal height of polonium to signal height of radon. The blue histogram in Fig.72 shows the ratio values of the events in Fig.70. The peak at ratio 1.09 is contributed by the true parent-daughter alpha events from the sequential decay of ^{222}Ra-^{218}Po-^{214}Pb. The events widely distributed on both sides of the peak are accidental background. To calculate the accidental background accurately, we collected the polonium events happening within 60 mins, which is between 10 mins and 70 mins after the radon triggers.

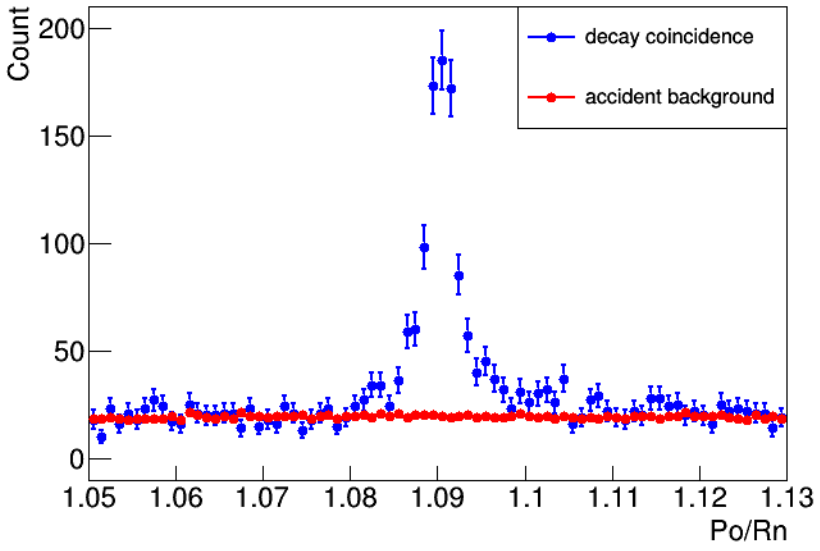

Figure 72: Decay coincidence of ^{222}Rn$\rightarrow^{218}$Po$\rightarrow^{214}$Pb (blue) and accidental background (red).

The distribution of the true parent-daughter alpha events from the sequential decay of ^{222}Ra-^{218}Po-^{214}Pb can be obtained from subtraction of the decay coincidence histogram and the accidental background histogram. The subtraction result is shown in Fig.73. To calculate the intrinsic resolution, we fitted the histogram using a single

Gaussian function. The mean value is 1.09 and the sigma value is 1.99×10^{-3} with $\chi^2/\mathrm{ndf} = 1.99$. The intrinsic resolution of Po/Rn ratio is 0.18% for σ and 0.42% for FWHM.

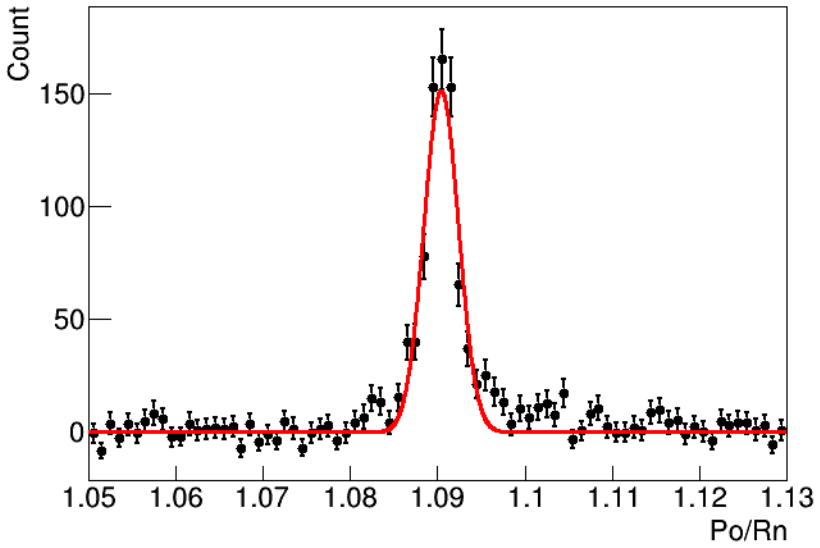

Figure 73: Intrinsic resolution without position dependence.

The intrinsic resolutions of polonium events or radon events should be better than the one of their ratio from consideration of error propagating. Here, we write the mean of Po/Rn ratio as $\mu_{\mathrm{Po/Rn}}$ and the sigma of Po/Rn ratio as $\sigma_{\mathrm{Po/Rn}}$. The error propagation function can be written as

$$(\frac{\sigma_{\mathrm{Po/Rn}}}{\mu_{\mathrm{Po/Rn}}})^2 = (\frac{\sigma_{\mathrm{Rn}}}{\mu_{\mathrm{Rn}}})^2 + (\frac{\sigma_{\mathrm{Po}}}{\mu_{\mathrm{Po}}})^2, \tag{47}$$

where σ_{Rn} and σ_{Po} are the intrinsic resolution of the radon events and the polonium events, respectively. μ_{Rn} is radon's alpha decay energy 5.59 MeV and μ_{Po} is polonium's alpha decay energy 6.11 MeV. The left side of equation (47) is the square of 0.18% obtained from the fitting result; In the right side σ_{Rn} and σ_{Po} are unknown. In general, the resolution of heat signal doesn't have significant energy dependence, we can assume $\sigma_{\mathrm{Rn}} \simeq \sigma_{\mathrm{Po}}$. In this assumption, $\sigma_{\mathrm{Rn}} \simeq \sigma_{\mathrm{Po}} = 7.43 \times 10^{-3}\,\mathrm{MeV}$ was

obtained from equation (47). Therefore, the intrinsic resolution of 5.59 MeV Rn events is 0.13% for σ and 0.31% for FWHM. This resolution is consistent with the resolution from silicon heater.

6.7 Comparison of waveforms of different signal heights

We have known the height of heat signal changes by event's location, but we haven't confirmed if the heat signal's waveform has the same position dependence. If position dependence also exists in the waveform of heat signal, we can use a waveform parameter to correct the signal height for a better resolution.

I selected ^{226}Ra events to compare the average waveforms of heat signals. The ^{226}Ra events are widely distributed from 0.15 V to 0.25 V in Fig.56. I separated these events in five different groups by the signal heights, such as 0.15-0.17 V, 0.17-0.19 V, ..., 0.23-0.25 V. The number of each group is different, but the smallest one has more than 30 events, so the waveform fluctuation of event by event is negligible. The average waveforms of this five groups are shown in Fig.74. The height of each average waveform is normalized to 1 and the timings of 10% of signal heights are aligned to 0.2 s. These five average waveforms are very similar with each other, the difference of average waveforms is less than 1%. This comparison is also applied to ^{222}Rn and ^{218}Po events, the results are same as ^{226}Ra case.

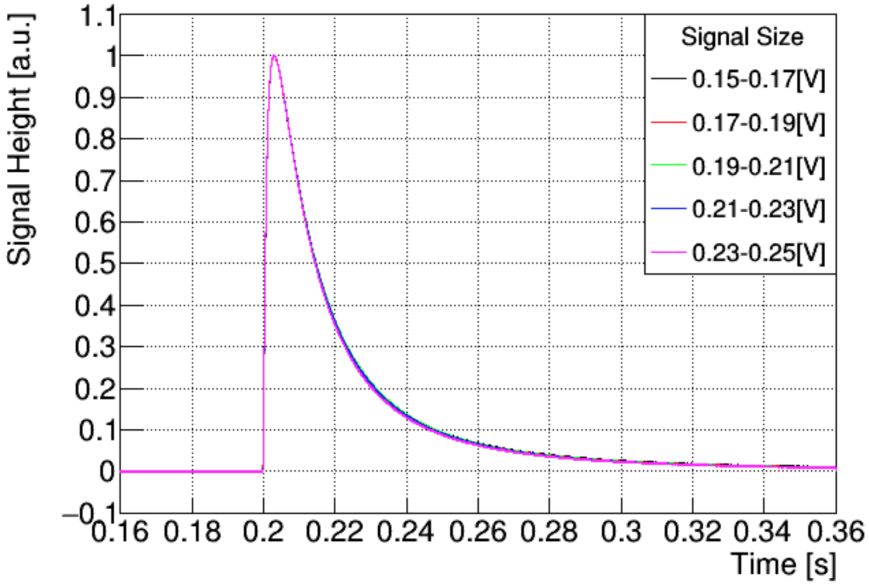

Figure 74: Average waveforms of different signal heights of ^{226}Ra events.

From the effect of position dependence, we predicted an unknown system in the crystal absorbed a part of energy from phonon. However, the energy would be released sometime. If the relaxation time $\tau \ll 0.2\,\mathrm{s}$, the system absorbs energy from phonon and release it immediately, there should be no difference in the signal height and no position dependence can be observed. In the case of $\tau \sim 0.2\,\mathrm{s}$, the release energy would induce a waveform difference, which is shown in Fig.75. Here, the phonon directly propagating to the metal film is defined as direct part; the phonon absorbed once by the unknown system and released later is defined as relaxation part. When an event occurs near the metal film, more phonons should be absorbed by the metal film, then its direct part is high; while the relaxation part is low, so its heat signal should have a shape like the upper waveform in Fig.75. When the event occurs far from the metal film, its waveform should have a lower direct part and a higher relaxation part. Therefore, a difference between waveforms of events at different positions should be observed.

However, from the comparison of waveforms of ^{226}Ra events at different positions, we found the waveforms are very similar with each other. This means the relaxation time of the assumed unknown system should have a much longer decay time than 0.2 s.

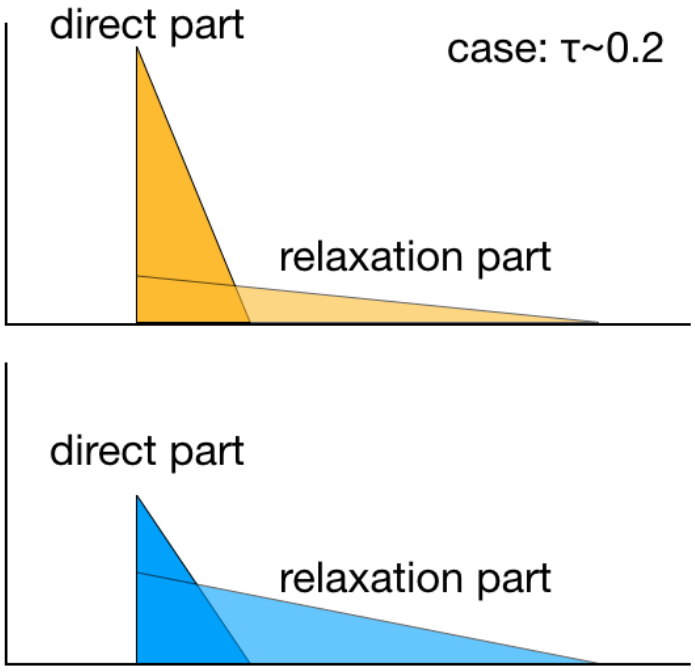

Figure 75: In the case of relaxation time $\tau \sim 0.2\,\mathrm{s}$, the waveform difference should be observed.

6.8 Possibility of an unknown mechanism in detector system

From the above data analysis results, we have known that there is a strong position dependence of heat energy in the CaF_2(Eu) scintillating bolometer. Since the silicon heater has a satisfying resolution, we can decide the problem happens in the crystal. From the correlation of light and heat signal's pulse height in Fig.56, we can know more energy of phonons were lost if events happened far from the metal film, while less energy was lost if events happened near the metal film. That fact also means some unknown system existing in the CaF_2(Eu) crystal absorbed the energy of phonons when they propagated to the metal film. The absorption of phonon energy is dependent of the 3D propagation path of phonon. The energy absorbed by the unknown system has to be released sometime. From the comparison of waveform, we can estimate the relaxation time must be much longer than 0.2 s.

To verify this hypothesis, we should consider the physical mechanism again to get some hints (Fig.76). In the crystal, phonon-phonon scattering obeys the conservation of total phonon energy and cannot act as the unknown system. The self-absorption of scintillation photons doesn't contribute so much effect to heat, so photons cannot play the role of unknown system. Moreover, photon-phonon interaction doesn't exist, because both of them are bose particles. Therefore, the unknown system must be related to electrons. In general, electrons are bound as pairs in dielectric crystals, there is no free electron inside. However, in the case of CaF_2(Eu) crystal, the possibility that Eu dope generates an unknown system relating to electrons cannot be rejected. We need to confirm that with some information of condensed matter physics.

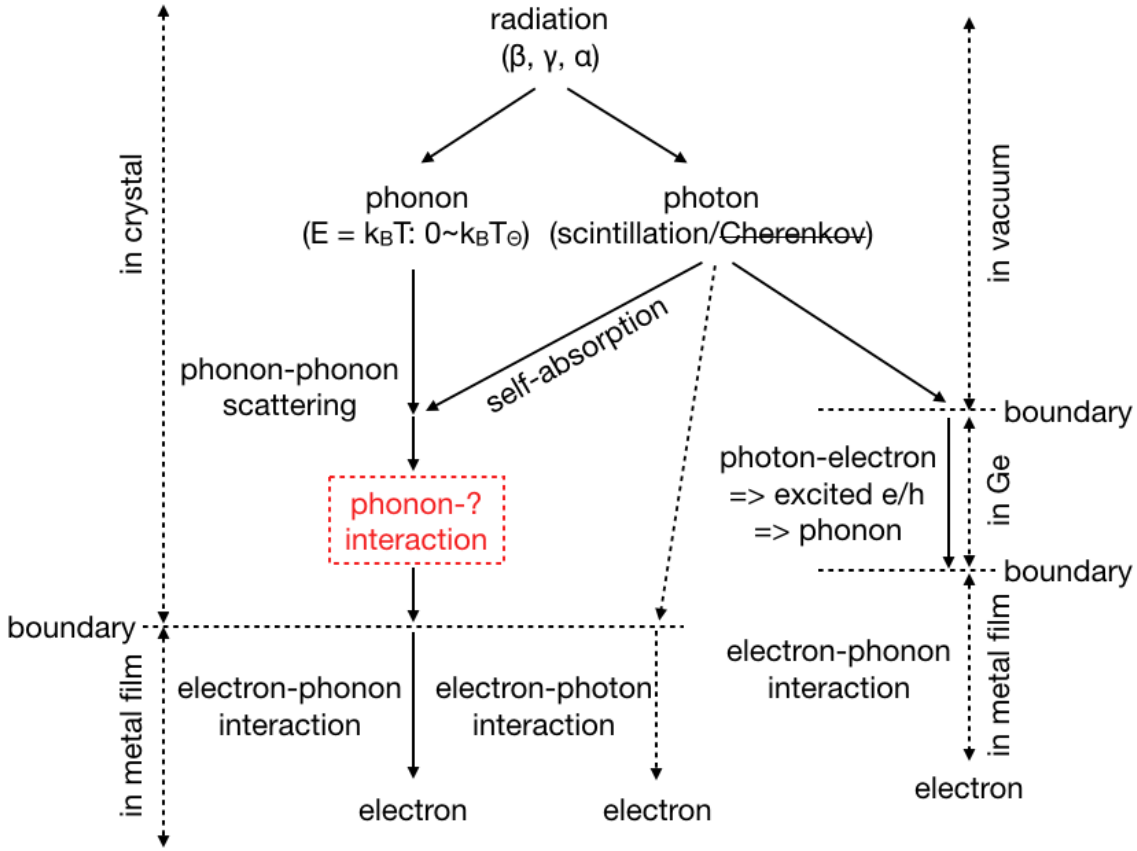

Figure 76: Existence of an unknown mechanism in the CaF_2(Eu) scintillating bolometer.

6.9 Interpretation of position dependence

6.9.1 Spin system in CaF_2(Eu)

From information of condensed matter physics, we found CaF_2(Eu) is a paramagnetic crystal and has a spin system inside [68]. Paramagnetic crystals are diamagnetic (ionic) crystal lattices and spin-systems, formed by ions of the transition elements with incomplete electronic shells. In our case, Eu is the transition element and CaF_2 is the diamagnetic crystal. When Eu ions are doped into a dielectric CaF_2 crystal, it generates an unpaired electron. The electron enters an orbit without forming a pair, so the paramagnetism that electrons originally possess remains. The paramagnetism of such systems is determined by the magnitude of the constant magnetic moment of the electronic shells. This is related, firstly, to the orbital motion of the electrons (orbital momenta), secondly, to their intrinsic motion, i.e., their spins. From this information, we have known that in addition to phonon system, there must be a spin system existing in the CaF_2(Eu) crystal. This spin system was also known from electron spin resonance of Eu^{2+} in CaF_2 [69].

6.9.2 Spin-lattice interaction to position dependence

From the double systems of phonons and spins, we have two conjectures to interpret the position dependence. The first conjecture is phonons lose energy by inelastic scatterings with the spin system [70]. In the paramagnetic material, the anisotropic energy for spins depends on the interatomic distance and the symmetry of the lattice, and thus changes with lattice vibration. This causes an spin-lattice interaction between spins and quantum of lattice vibration, phonon [71]. The spin system is strong coupled to the crystal lattice. This is continuous transfer of energy between the spins and the lattice, leading eventually to the establishment of thermodynamic equilibrium.

In cryogenic particle detection with a crystal absorber, athermal phonons are

initially generated near the vortex of an event in the crystal, and down-covert to lower energy phonons becoming a thermal phonon distribution. In this case of using a CaF_2(Eu) absorber, a significant portion of initial athermal phonons can interact with the spin system and lose a part of energy by inelastic scatterings with spins. Therefore, events near the phonon collector film experience less inelastic scatterings of athermal phonons to spins providing larger heat signals, while those further from the film result in smaller and slower signals in the heat channel.

The other conjecture is phonons lose energy by excitation of Eu^{2+}'s ground state. In the external magnetic field, the ground state of Eu^{2+} is separated into two different energy levels (Fig.77), which is well known as Zeeman effect. One energy level is spin parallel to the magnetic field and stable; the other level is spin antiparallel to the magnetic field and unstable. Basically, the Eu^{2+} is in the stable state where its spin direction is parallel to the magnetic field. However, when phonon interacts with the electron, the Eu^{2+} absorbs phonon's energy and will be excited to the excited state where the spin direction is antiparallel to the magnetic field [72]. This spin-lattice interaction was also found in other paramagnetic ions doped crystals [71]. These crystals are called paramagnetic crystals and are applied to electron spin resonance.

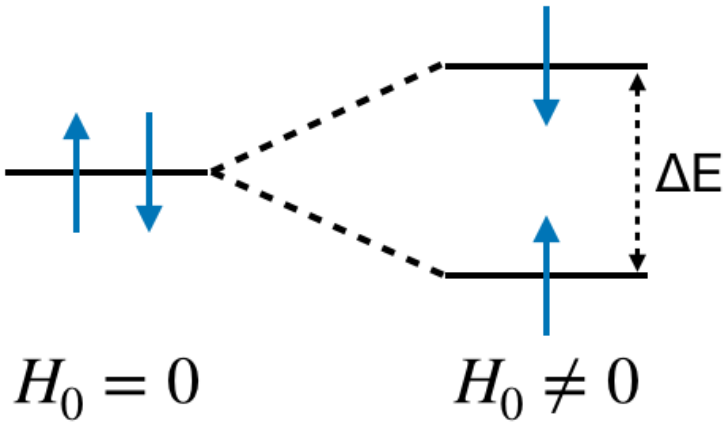

Figure 77: A scheme of the ground state separated by the external magnetic field in the case of $S = 1/2$.

Now we have known that the energy of phonons or lattice vibration can be

absorbed by Eu^{2+} to an excited state in a magnetic field. To confirm if phonons have enough energy to excite Eu^{2+}, we did a simple calculation. At 20 mK, phonons have an average energy of $k_BT = 2$ μeV ($0 \sim 50$ meV). In this measurement, the sources of magnetic field are geomagnetism and MMC's meander coil. The effect of magnetic field from the meander coil is less than geomagnetism for our crystal, so we can ignore it and only consider the geomagnetism (Here, we didn't consider effect of superconducting Ni shield. The superconducting shield can freeze the internal magnetic field to create a stable field environment, but it could generate a much stronger magnetic field [73]). The geomagnetism in Tokyo is 45000 nT. The split energy of Eu^{2+}'s ground state is proportional to the strength of geomagnetism (Fig.78), so the splitting energy ΔE is equal to 5 neV, which is calculated by

$$\Delta E = g\beta H_0, \tag{48}$$

where g is the electron's so-called g-factor, $g = 2.0$ for the free electron and $\beta = 6.0 \times 10^{-5}$ eV·T^{-1} is the Bohr magneton. In the case of Eu^{2+}, the ground state $S = 7/2$ has a splitting energy of 35 neV. Therefore, most phonons have enough energy to excite Eu^{2+} in our measurement condition.

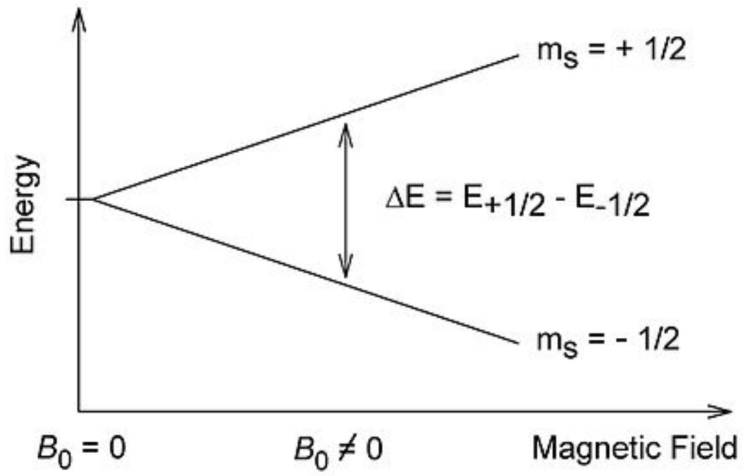

Figure 78: Relation of magnetic field strength and split energy of spin system.

Let's consider the physical phenomena that actually occurred in the CaF_2(Eu) crystal. When radiation deposits energy inside the crystal, phonon wave propagates to the metal film. In the propagation path, the phonon repeats to excite Eu^{2+} ions, which results in many inelastic scatterings. A phonon wave with energy $h\nu'$ excited Eu^{2+}, in this process, the phonon wave loses energy $\sim g\beta H_0$ and becomes a new phonon wave with a lower energy $h\nu$". Of course, the number of inelastic scatterings depends on the event's occurring positions. If the event happens far from the metal film, more inelastic scatterings can happen and result in a smaller heat signal; if the event happens near the metal film, less inelastic scattering can happen and result in a larger heat signal.

The interpretation using the excitation of Eu^{2+} by spin-lattice interaction is satisfied by the energy condition. However, we also need to confirm the relaxation time of excited state of Eu^{2+} in the CaF_2 crystal. The relaxation time of Eu^{2+} in CaF_2 has been reported in [74]. It has a strong temperature dependence shown in Fig.79. The relaxation time doesn't change by doping density. So our CaF_2(Eu) with 0.17% Eu dope should have the same relaxation time property.

The experimental temperature dependence of the spin-lattice relaxation was adequately described by

$$\tau^{-1} = 12T + 5.3 \times 10^{-4} T^5. \tag{49}$$

At the 20 mK, the relaxation time is as long as 4 s from this previous experiment's data. This value is 20 times longer than our signal window. Therefore, the energy absorbed by the Eu^{2+} ions will release the energy slowly in 4 s, which could result in that we cannot observe the waveform difference.

In the both conjectures, we can interpret that the strong position dependence is attributed to the spin-lattice interaction of paramagnetic Eu ions in CaF_2 crystal. In cryogenic particle detection with a crystal absorber, phonons are initially generated

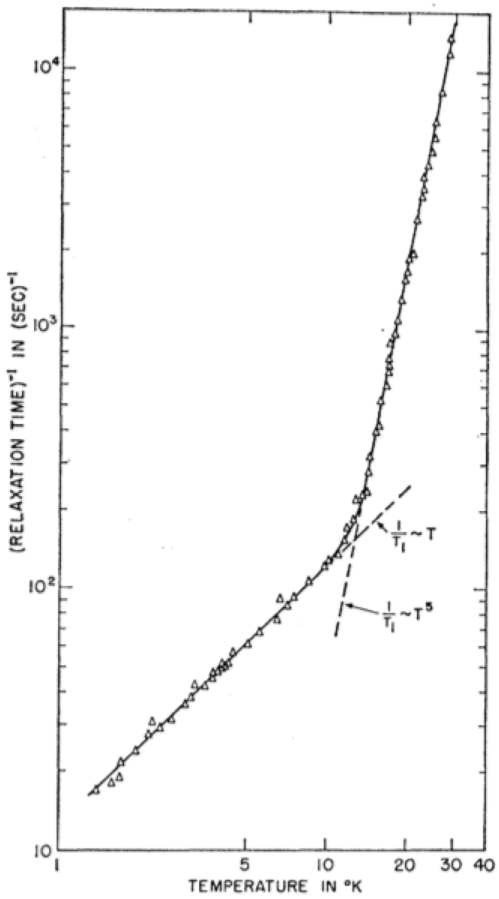

Figure 79: Relaxation data for 0.18% Eu^{2+} in CaF_2 [74].

near the vortex of an event in the crystal, and down-covert to lower energy phonons becoming a thermal phonon distribution. In this case of using a CaF_2(Eu) absorber, a significant portion of initial phonons can inelastically scatter with paramagnetic Eu ions or excite them. The excitation of paramagnetic ions from phonons takes place near the event location. However, the relaxation mechanism of the stored energy in the paramagnetic system to the crystal lattice has strong temperature dependent characteristics. The energy release from the spin system becomes very inefficient at the temperatures of the detector operation. Therefore, events near the phonon collector film experience less inelastic scattering of athermal phonons to the paramagnetic ions providing larger heat signals while those further from the film result in smaller and slower signals in the heat channel.

6.10 The complete mechanism of CaF_2(Eu) scintillating bolometer

In addition of phonon-spin inelastic scattering, the mechanism of CaF_2(Eu) scintillating bolometer is finally completed (Fig.80).

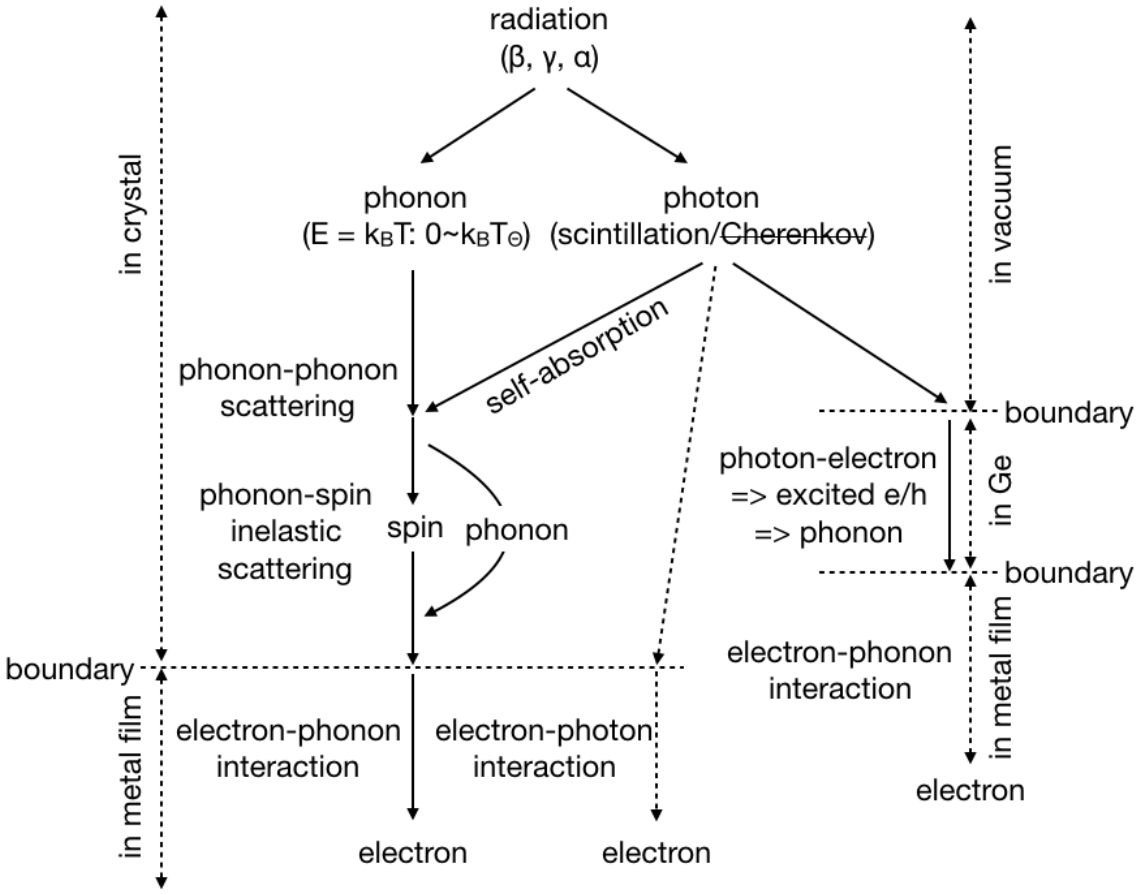

Figure 80: A scheme of the detection mechanism of CaF_2(Eu) scintillating bolometer.

When radiation deposits energy in the CaF_2(Eu) crystal, most of the energy generates high energy phonons and a few percents of the energy generates scintillation. The high energy phonons reduce their energy quickly by phonon-phonon scatterings and thermalize the whole CaF_2(Eu) crystal. Until reaching the metal film phonon collector, phonons have a probability of inelastic scatterings with spins induced by Eu^{2+} ions in the crystal. At the boundary of the crystal and the metal

film phonon collector, phonons in the crystal transfer heat to the electrons in the metal film by electron-phonon interaction. Finally, the electrons transfer the heat from the phonon collector to the MMC through the gold wires.

On the other hand, the scintillation light has three physical processes. The first one is self-absorption of the CaF_2(Eu) crystal. Since the absorption length of the CaF_2(Eu) crystal is quite short, 81% of scintillation is absorbed by the crystal. The second one is the absorption by the metal film phonon collector. However, the absorption probability is negligible owing to the silver layer of the phonon collector. The third one is the absorption by the germanium wafer, in other words, detection by the light detector. When the scintillation light irradiates the surface of the germanium wafer, the electrons in germanium are excited up to an excited state by phonon-electron interaction. Right after that, the excited electrons drop to the ground state with releasing the energy in the form of phonon. The phonons propagate in the germanium wafer and interact with electrons at the boundary of the germanium and the gold films. The rest of this process is same as the case of the metal film phonon collector on the CaF_2(Eu) crystal.

In the case of beta rays, Cherenkov radiation is emitted in the CaF_2(Eu) crystal. As same as the scintillation light, most of Cherenkov radiation is absorbed by the crystal itself. The absorption by the metal film phonon collector is also negligible from the calculation by the Frank-Tamm formula.

The above is the total detection mechanism of our CaF_2(Eu) scintillating bolometer.

7 Conclusion

Scintillating bolometer is a powerful tool to search the $0\nu\beta\beta$ decay, because it can achieve a high energy resolution and a good discrimination power to reduce background. Our experiment group plans to develop a scintillating bolometer to search for the $0\nu\beta\beta$ decay of ^{48}Ca.

In this dissertation, we selected CaF_2(Eu) scintillator as absorber of scintillating bolometer. We established a scintillating bolometer using a 312 g CaF_2(Eu) crystal with a readout technology of metallic magnetic calorimeters. Phonons and scintillation photons of the CaF_2(Eu) were detected by a metal film phonon collector and a germanium light detector, respectively. We developed a Ag-Au multi-layer metal film as the phonon collector to satisfy both a high thermal conductivity and a high optical reflectivity. From some basic optical calculations and Monte Carlo simulation, we understood most of scintillation photons were absorbed by crystal itself. The self-absorption had position dependence, but its deviation was just 0.1% and didn't affect much the detector's resolution. Application of the Ag-Au film reduced the scintillation absorption of metal film to a negligible level.

A set of successful measurements were carried out for simultaneous detection for heat and light signals at 20 mK in an above-ground laboratory. We found large light signals with clear difference in scintillation yields between electron- and alpha-induced events. The comparison of relative amplitudes of heat and light signals obtained about 10 σ discrimination power and a quenching factor of 17% at 4.9 MeV. The resolution of scintillation signals was 3.1% for 4.9 MeV alpha events, so we can estimate that the same energy beta/gamma events should have 1.3% energy resolution using the 17% quenching factor. This resolution has already exceeded the current running CANDLES experiment's 2.5% resolution.

The resolution of phonon signals was 0.3% (FWHM) for 5.6 MeV, which was evaluated by silicon heater's signals. However, the alpha event's resolution was

100 times worse. We hypothesized the phonon signals experiencing strong position dependence from the event locations and confirmed the position dependence by analyzing ^{222}Rn $\rightarrow$ ^{218}Po $\rightarrow$ ^{214}Pb continuous alpha decay events. The resolution calculated from the continuous alpha decay was 0.3% (FWHM), consistent with that of silicon heater. Therefore, we can say the intrinsic resolution of our scintillating bolometer has already satisfied our goal of resolution, 0.5% (FWHM).

From the two-dimensional distribution of heat vs light and the position dependence, we can know phonon signal's pulse height is dependent of the distance from its location to the phonon collector. Hence, we proposed a hypothesis that an unknown system absorbed phonon's energy when phonon propagated through the crystal. From the condensed matter physics, we found there is a spin system induced by Eu^{2+} ions in the CaF_2 crystal. We consider the position dependence could be induced by spin-lattice interaction of Eu^{2+} ions in the CaF_2.

8 Future prospect

In this study, we developed a next-generation detector to search for neutrinoless double beta decay of ^{48}Ca. Even the resolution was improved, it didn't realize our goal of resolution. We have several plans to remodel the scintillating bolometer. One plan is to apply a magnetic field to the crystal. We can increase the excited energy of Eu^{2+} and avoid phonons from exciting them. However, in this case, we have to maintain the performance of MMC from the effect of external magnetic field.

The second plan is to apply $CaWO_4$ crystal as the absorber (we need a crystal with calcium component, but we don't have to obsess with CaF_2). In fact, the development of multi-layer metal film phonon collector is also suitable for $CaWO_4$ (420 nm) [75]. $CaWO_4$ was produced by a company for the CRESST experiment [76] until 10 years ago. We can obtain the crystals in a little higher price. Therefore, a scintillating bolometer with a $CaWO_4$ crystal can be a good choice to search for $0\nu\beta\beta$ decay of ^{48}Ca.

9 Acknowledgments

I would like to thank my supervisor, Prof. Yoshida Sei, for giving me the chance to develop the next generation detector for the CANDLES experiment. I leant the importance of defense ability as a researcher from him. I also wold like to thank our collaborator, Prof. Kim Yong-Hamb. Without his support of low temperature technology, I cannot complete my doctoral study. I also would like to thank Prof. Lee Minkyu for taking care of our two month resident in KRISS. He also gave some importance comments for this study.

Several students cooperated and contributed a lot for carrying out this measurement. I would like to thank Kwon Do-hyung for the preparation for this experiment and the maintenance of dilution fridge. I also would like to thank Kim Inwook and Kim Hye-Lim for teaching me a lot about the low temperature techniques. Finally, I would like to thank Lee Hye-Jin to prepare for the MMC sensor and would like to thank Tetsuno Konosuke to help Helium transfer work.

List of Figures

1 Nuclear mass as a function of the atomic number Z in the case of an isobar candidate with even mass number A [14]. 13

2 Feynman diagram for $2\nu\beta\beta$ (left) and $0\nu\beta\beta$ (right) [24]. 14

3 Phase space factors $G_{0\nu}$ in units of 10^{-15} year^{-1}. The blue points are from [25] , and the black points are from [26] 15

4 Top panel: nuclear matrix elements ($M_{0\nu}$) for $0\nu\beta\beta$ decay candidates as a function of mass number A. Bottom panel: associated $0\nu\beta\beta$ decay half-lives, scaled by the square of the unknown parameter $m_{\beta\beta}$. The plotted results are introduced in [32]. 17

5 Illustration of the spectra of the sum of the electron kinetic energies K_e (Q is the endpoint) for the $\beta\beta(2\nu)$ normalized to 1 (dotted curve) and $\beta\beta(0\nu)$ decays (solid curve) [33]. The $\beta\beta(0\nu)$ spectrum is normalized to 10^{-2} (10^{-6} in the inset). Both spectra use an energy resolution of 5%. 18

6 A typical energy diagram of a molecule [40]. 25

7 A p-n junction with reverse bias operating as a detector [41]. 27

8 Detection principle of the NEMO-3 detector [37]. 28

9 Detection principle of bolometer. 29

10 Scheme of signal output in low temperature measurement. 30

11 Scheme diagram of scintillating bolometer. 32

12 Background discrimination by simultaneous detection of heat and scintillation light. 32

13 Decay scheme of ^{48}Ca [47]. 34

14 Temperature dependence of light yield of CaF_2(Eu) scintillator [52]. . 37

15 Experimental setup of a 0.3 g CaF_2(Eu) scintillating bolometer for WIMPs detection [53]. 38

16 Simultaneous detection of heat and light signals by a 0.3 g CaF_2(Eu) scintillating bolometer [53]. 39
17 The spectrum of external alpha events [53]. 39
18 Importance of energy resolution for neutrinoless double beta search. . 41
19 The schematics of phonon-scintillation detection using a CaF_2(Eu) crystal and MMC readouts. 43
20 CaF_2(Eu) crystal used in this experiment. 44
21 Emission and absorption spectra of CaF_2(Eu) scintillator. 46
22 Mechanism of events happening in the crystal. 47
23 A multi-layer film phonon collector is used to collect phonons generated in the crystal. 48
24 Mechanism of phonon propagation in the crystal and at the boundary of crystal and metal film. 49
25 The structure of multi-layer metal film phonon collector. 51
26 Design of gold pattern. 52
27 Effect of gold pattern. The red points represent the gold wires' bonding positions. 53
28 Evaporation machine of Etsumi company. Release of this photo has been permitted by the employee in charge of the deposition work. . . 56
29 Evaporation target spots. Release of this photo has been permitted by the employee in charge of the deposition work. 57
30 Crystal holder for the evaporation process. 58
31 Mask for the second evaporation process. 58
32 The gold face of multi-layer metal film. 59
33 The silver face of multi-layer metal film 59
34 A schematic diagram of MMC. 60
35 Three types of photon propagations. 62
36 Scheme of simulation model. 64

37 Optical parameters of the components in the simulation model. (a) real refractive index of CaF_2 crystal [61]; (b) real and imaginary refractive index of germanium [62]; (c) real and imaginary refractive index of gold [63]; (d) real and imaginary refractive index of silver [63]. 65

38 Position dependence of scintillation photon absorption by the crystal itself. The color in this figure shows the absorptance, which is represented by the ratio of absorbed photons by crystal to generated photons at that position. 66

39 Effect of phonon absorption by metal film. 67

40 Superconducting elements. This graph is taken from "Superconductivity in the metallic elements at high pressures" [64]. 69

41 Angular wavelength dependence on absorption of silver film on the CaF_2(Eu) crystal surface. The red dotted line shows the emission spectrum of CaF_2(Eu) scintillator. 71

42 Angular wavelength dependence on absorption of gold film on the CaF_2(Eu) crystal surface. The red dotted line is as same as in Fig.41. 71

43 Angular wavelength dependence on absorption of copper film on the CaF_2(Eu) crystal surface. The red dotted line is as same as in Fig.41. 72

44 Position dependence of scintillation photon absorption by the silver film. The color in this figure shows the absorptance, which is represented by the ratio of absorbed photons by Ag film to generated photons at that position. 73

45 Absorption by Au film, as in Fig.44. 73

46 Position dependence of scintillation photon detection by the Ge wafer. The color in this figure shows the detection rate, which is represented by the ratio of detected photons by the Ge wafer to generated photons at that position. Here, the maximum detection rate is about 2 times of the minimum one in this simulation result. The reason of this large difference could be from the ideal crystal surface condition. 74
47 Position dependence of photons detected by the Ge wafer along the Z-direction of CaF_2(Eu) crystal. 75
48 Position dependence of photons detected by the Ge wafer along the R^2-direction of CaF_2(Eu) crystal. 76
49 Position dependence of scintillation photons escaped from the detector module. The color in this figure shows the escape rate, which is represented by the ratio of escaped photons to generated photons at that position. 76
50 Effect of Cherenkov radiaiton. 78
51 Total understood mechanism of the CaF_2(Eu) scintillating bolometer. 79
52 The pictures of detector set-up. 81
53 Light collections of different reflectors. 84
54 Dilution refrigerator (The picture is from www.leiden-cryogenics.com). 85
55 DAQ. The components in the blue region are at 20mK temperature. . 86
56 Pulse height distribution of heat and light signals. 88
57 Discrimination power between β/γ and α events near 4.9 MeV region. 91
58 Scheme diagram of relation of anti-correlation and resolution. 92
59 Resolution of ^{226}Ra events. The peak of ^{226}Ra is fitted by a single Gaussian function. 93
60 Resolution vs anti-correlation angle. 94
61 Fit of four peaks, ^{147}Sm, ^{226}Ra, ^{218}Po and ^{216}Po. 95

62 Power function fit of light signal height of α events. The error of each point uses the sigma value of the single peak fitting in Fig.61. 96
63 Background fitting of alpha spectrum. $\chi^2/\mathrm{ndf} = 2.4$. 98
64 Temperature dependence of heater signal's pulse height. 100
65 Resolution of heater signal's pulse height between 28 to 32 hours. . . 100
66 Moving average of heater pulse. 101
67 Normalized heater pulse after temperature correction. 101
68 Energy resolution of heater pulse after temperature correction. 102
69 Distribution of pulse height of ^{226}Ra events in the heat channel. . . 103
70 Evidence of position dependence. 106
71 Decay time of sequential decay of $^{222}\mathrm{Rn}\rightarrow{}^{218}\mathrm{Po}\rightarrow{}^{214}\mathrm{Pb}$. 107
72 Decay coincidence of $^{222}\mathrm{Rn}\rightarrow{}^{218}\mathrm{Po}\rightarrow{}^{214}\mathrm{Pb}$ (blue) and accidental background (red). 108
73 Intrinsic resolution without position dependence. 109
74 Average waveforms of different signal heights of ^{226}Ra events. 111
75 In the case of relaxation time $\tau \sim 0.2\,\mathrm{s}$, the waveform difference should be observed. 113
76 Existence of an unknown mechanism in the CaF_2(Eu) scintillating bolometer. 115
77 A scheme of the ground state separated by the external magnetic field in the case of $S = 1/2$. 117
78 Relation of magnetic field strength and split energy of spin system. . 118
79 Relaxation data for 0.18% Eu^{2+} in CaF_2 [74]. 120
80 A scheme of the detection mechanism of CaF_2(Eu) scintillating bolometer. 121

List of Tables

1 Observed $2\nu\beta\beta$ nuclei. 13

2 $Q_{\beta\beta}$ value and natural abundance of each $0\nu\beta\beta$ isotope. 20

3 Comparison of different Ca scintillation crystals 35

4 Basic properties of CaF_2(Eu) crystal at 300K 45

5 Thermal conductivities of metals at 300K [65]. 68

6 Impurity of ^{147}Sm 89

7 Assumed internal α backgrounds. 97

References

[1] G. Danby et al. Observation of high-energy neutrino reactions and the existence of two kinds of neutrinos. *Physical Review Letters*, 9:36, 1995.

[2] M. L. Perl et al. Evidence for anomalous lepton production in e^+-e^- annihilation. *Physical Reveiw Letters*, 35:1489, 1975.

[3] DONUT Collaboration et al. Observation of tau neutrino interactions. *Physics Letters B*, 504:218–224, 2001.

[4] D. S. Harmer R. Davis, Jr. and K. C. Hoffman. Search for neutrinos from the sun. *Physical Review Letters*, 20:1205, 1968.

[5] Q. R. Ahmad et al. Measurement of the rate of $\nu_e + d \rightarrow p + p + e^-$ interactions produced by ^{8}B solar neutrinos at the sudbury neutrino observatory. *Physical Review Letters*, 87:071301, 2001.

[6] Y. Fukuda et al. Evidence for oscillation of atmospheric neutrinos. *Physical Review Letters*, 81:1562, 1998.

[7] Y. Abe et al. Indication of reactor $\bar{\nu}_e$ disappearance in the double Chooz experiment. *Physical Review Letters*, 108:131801, 2012.

[8] F. P. An et al. Observation of electron-antineutrino disappearance at Daya Bay. *Physical Review Letters*, 108:171803, 2012.

[9] J. K. Ahn et al. Observation of reactor electron antineutrinos disappearance in the RENO experiment. *Physical Review Letters*, 108:191802, 2012.

[10] K. Abe et al. Evidence of electron neutrino appearance in a muon neutrino beam. *Physical Review D*, 88:032002, 2013.

[11] M. Tanabashi et al. Review of particle physics. *Physical Review D*, 98:030001, 2018.

[12] A. Gando et al. Search for majorana neutrinos near the inverted mass hierarchy region with KamLAND-Zen. *Physical Review Letters*, 117:082503, 2016.

[13] M. Goeppert-Mayer. Double beta-disintegration. *Physical Review*, 48:512, 1935.

[14] S. DellOro et al. Neutrinoless double beta decay: 2015 review. *Advances in High Energy Physics*, 2016:2162659, 2016.

[15] R. Arnold et al. Measurement of the double-beta decay half-life and search for the neutrinoless double-beta decay of ^{48}Ca with the NEMO-3 detector. *Physical Review D*, 93:112008, 2016.

[16] The GERDA Collaboration et al. Measurement of the half-life of the two-neutrino double beta decay of ^{76}Ge with the GERDA experiment. *Journal of Physics G: Nuclear and Particle Physics*, 40:035110, 2013.

[17] R. Arnold et al. Final results on ^{82}Se double beta decay to the ground state of ^{82}Kr from the NEMO-3 experiment. *The European Physical Journal C*, 78:821, 2018.

[18] NEMO-3 Collaboration et al. Measurement of the two neutrino double beta decay half-life of Zr-96 with the NEMO-3 detector. *Nuclear Physics A*, 847:168–179, 2010.

[19] R. Arnold et al. Detailed studies of ^{100}Mo two-neutrino double beta decay in NEMO-3. *The European Physical Journal C*, 79:440, 2019.

[20] H. Ejiri et al. Double beta decays of ^{116}Cd. *Journal of the Physical Society of Japan*, 64:339–343, 1995.

[21] C. Alduino et al. Measurement of the two-neutrino double-beta decay half-life of ^{130}Te with the CUORE-0 experiment. *The European Physical Journal C*, 77:13, 2017.

[22] J. B. Albert et al. Improved measurement of the $2\nu\beta\beta$ half-life of ^{136}Xe with the EXO-200 detector. *Physical Review C*, 89:015502, 2014.

[23] J. Argyriades et al. Measurement of the double-β decay half-life of ^{150}Nd and search for neutrinoless decay modes with the NEMO-3 detector. *Physical Review C*, 80:032501(R), 2009.

[24] S. R. Elliott F. T. Avignone, III and J. Engel. Double beta decay, majorana neutrinos, and neutrino mass. *Reviews of Modern Physics*, 80:481, 2008.

[25] F. Boehm and P. Vogel. *Physics of Massive Neutrinos*. Cambridge University Press, 1992.

[26] J. Kotila and F. Iachello. Phase-space factors for double-β decay. *Physical Review C*, 85:034316, 2012.

[27] V. A. Rodin et al. Uncertainty in the $0\nu\beta\beta$ decay nuclear matrix elements. *Physical Review C*, 68:044302, 2003.

[28] J. Menendez et al. Disassembling the nuclear matrix elements of the neutrinoless $\beta\beta$ decay. *Nuclear Physics A*, 818:139–151, 2009.

[29] P. K. Rath et al. Uncertainties in nuclear transition matrix elements for neutrinoless $\beta\beta$ decay within the projected-Hartree-Fock-Bogoliubov model. *Physical Review C*, 82:064310, 2010.

[30] J. Barea and F. Iachello. Neutrinoless double-β decay in the microscopic interacting boson model. *Physical Review C*, 79:044301, 2009.

[31] T. R. Rodriguez and G. Martinez-Pinedo. Energy density functional study of nuclear matrix elements for neutrinoless $\beta\beta$ decay. *Physical Review Letters*, 105:252503, 2010.

[32] J. Engel and J. Menendez. Status and future of nuclear matrix elements for neutrinoless double-beta decay: a review. *Reports on Progress in Physics*, 80:046301, 2017.

[33] S. R. Elliott and P. Vogel. Double beta decay. *Annual Review of Nuclear and Particle Science*, 52:115–151, 2002.

[34] G. J. Feldman and R. D. Cousins. Unified approach to the classical statistical analysis of small signals. *Physical Review D*, 57:3873, 1998.

[35] I. Shimizu and M. Chen. Double beta decay experiments with loaded liquid scintillator. *Frontiers in Physics*, 7:33, 2019.

[36] F. T. Avignore III and S. R. Elliott. The search for double beta decay with germanium detectors: Past, present, and future. *Frontiers in Physics*, 7:6, 2019.

[37] A. S. Barabash et al. Calorimeter development for the SuperNEMO double beta decay experiment. *Nuclear Instruments and Methods in Physics Research Section A: Accelerators, Spectrometers, Detectors and Associated Equipment*, 868:98–108, 2017.

[38] O. Cremonesi C. Brofferio and S. DellOro. Neutrinoless double beta decay experiments with TeO_2 low-temperature detectors. *Frontiers in Physics*, 7:86, 2019.

[39] G. B. Kim et al. Novel measurement method of heat and light detection for neutrinoless double beta decay. *Astroparticle Physics*, 91:105–112, 2017.

[40] T. Nicholas. *Measurement and Detection of Radiation (second edition).* Taylor & Francis Press, 1995. p219.

[41] T. Nicholas. *Measurement and Detection of Radiation (second edition).* Taylor & Francis Press, 1995. p250.

[42] H. V. Klapdor-Kleingrothaus. First evidence for neutrinoless double beta decay. *Foundations of Physics*, 33:813–829, 2003.

[43] D. R. Artusa et al. Initial performance of the CUORE-0 experiment. *The European Physical Journal C*, 74:2956, 2014.

[44] I. Kim et al. Application of metallic magnetic calorimeter in rare event search. *Superconductor Science and Technology*, 30:094005, 2017.

[45] J. W. Beeman et al. Current status and future perspectives of the LUCIFER experiment. *Advances in High Energy Physics*, 2013:237973, 2013.

[46] C. Arnaboldi et al. CUORE: a cryogenic underground observatory for rare events. *Nuclear Instruments and Methods in Physics Research Section A: Accelerators, Spectrometers, Detectors and Associated Equipment*, 518:775–798, 2004.

[47] A. Bakalyarov et al. Search for β^- and $\beta^-\beta^-$ decays of ^{48}Ca. *Nuclear Physics A*, 700:17–24, 2002.

[48] R. F. Lang and W. Seidel. Search for dark matter with CRESST. *New Journal of Physics*, 11:105017, 2009.

[49] A. Senyshyn et al. Thermal properties of $CaMoO_4$: Lattice dynamics and synchrotron powder diffraction studies. *Physical Review B*, 73:014104, 2006.

[50] A. Alessandrello et al. Development of a thermal scintillating detector for double beta decay of ^{48}Ca. *Nuclear Physics B (Proc. Suppl.)*, 28A:233–235, 1992.

[51] E. Fiorini and T. O. Niinikoski. Low-temperature calorimetry for rare decays. *Nuclear Instruments and Methods in Physics Research*, 224:83–88, 1984.

[52] P. Belli et al. Response of a "large" CaF_2(Eu) scintillator at low temperature. *Nuclear Instruments and Methods in Physics Research A*, 357:329–332, 1995.

[53] C. Bobin et al. Alpha/gamma discrimination with a CaF_2(Eu) target bolometer optically coupled to a composite infrared bolometer. *Nuclear Instruments and Methods in Physics Research A*, 386:453–457, 1997.

[54] T. Alain. *Functionalized Inorganic Fluorides: Synthesis, Characterization & Properties of Nanostructured Solids.* A John Wiley and Sons, Ltd, Publication, 2010.

[55] Z. Cao et al. *Advanced Materials, CEAM 2011.* Trans Tech Publication Ltd, Switzerland, 2011.

[56] G. Buse et al. First scintillating bolometer tests of a CLYMENE R&D on Li_2MoO_4 scintillators towards a large-scale double-beta decay experiment. *Nuclear Instruments and Methods in Physics Research Section A: Accelerators, Spectrometers, Detectors and Associated Equipment*, 891:87–91, 2018.

[57] C. K. Duan et al. The unusual temperature dependence of the Eu^{2+} fluorescence lifetime in CaF_2 crystals. *Journal of Alloys and Compounds*, 408-412:784–787, 2005.

[58] Private communications with S. Yoshida and S. Umehara who are the staff of the CANDLES experiment.

[59] N. Chitvoranund et al. Effects of surface treatments on adhesion of silver film on glass substrate fabricated by electroless plating. *Journal of the Australian Ceramic Society*, 49(1):62–69, 2013.

[60] A. Axelevitch et al. Investigation of optical transmission in thin metal films. *Physics Procedia*, 32:1–13, 2012.

[61] I. H. Malitson. A redetermination of some optical properties of calcium fluoride. *Applied Optics*, 2:1103–1107, 1963.

[62] D. E. Aspnes and A. A. Studna. Dielectric functions and optical parameters of Si, Ge, GaP, GaAs, GaSb, InP, InAs, and InSb from 1.5 to 6.0 eV. *Physical Review B*, 27:985, 1983.

[63] P. B. Johnson and R. W. Christy. Optical constants of the noble metals. *Physical Review B*, 6:4370, 1972.

[64] J. J. Hamlin. Superconductivity in the metallic elements at high pressures. *Physica C: Superconductivity and its Applications*, 514:59–76, 2015.

[65] https://periodictable.com/Properties/A/ThermalConductivity.html.

[66] J. D. Jackson. *Classical electrodynamics*. John Wiley & Sons, Inc., 1999. p637-p640.

[67] P. Belli et al. Search for α decay of natural Europium. *Nuclear Physics A*, 789:15–29, 2007.

[68] L. A. Sorin and M. V. Vlasova. *Electron Spin Resonance of Paramagnetic Crystals*. Plenum Press and Israel Program for Scientific Translations, Ltd., 1973. p1.

[69] O. Matumura et al. Electron spin resonance of Eu^{++} in natural CaF_2. *Journal of the Physical Society of Japan*, 13:768–769, 1958.

[70] R. D. Mattuck and M. W. P. Strandberg. Spin-phonon interaction in paramagnetic crystals. *Physics Review*, 119:1204, 1960.

[71] L. A. Sorin and M. V. Vlasova. *Electron Spin Resonance of Paramagnetic Crystals*. Plenum Press and Israel Program for Scientific Translations, Ltd., 1973. p125-p129.

[72] K. N. Shrivastava. Splitting of states of Eu^{2+} by phonons in CaF_2: A novel correction to the spin-hamiltonian. *Physics Letters A*, 31:454–455, 1970.

[73] Private communications with Y. H. Kim who is the staff of the IBS and the KRISS laboratory.

[74] C. Y. Huang. Paramagnetic relaxation of some rare-earth ions in diamagnetic crystals. *Physical Review*, 139:A241, 1965.

[75] V. B. Mikhailik and H. Kraus. Performance of scintillation materials at cryogenic temperatures. *physica status solidi (b)*, 247:1583–1599, 2010.

[76] G. Angloher et al. Commissioning run of the CRESST-II dark matter search. *Astroparticle Physics*, 31:270–276, 2009.